

Proteomic and functional mapping of cardiac Nav1.5 channel phosphorylation

1
2
3
4
5
6
7
8
9
10
11
12
13
14
15
16
17
18
19
20
21
22
23
24
25
26
27
28
29
30
31
32
33
34
35
36
37
38
39
40
41
42
43
44
45
46
47
48
49
50
51

**Proteomic and functional mapping of cardiac Nav1.5 channel phosphorylation
reveals multisite regulation of surface expression and gating**

Maxime Lorenzini^a, Sophie Burel^a, Adrien Lesage^a, Emily Wagner^b, Camille Charrière^a, Pierre-Marie Chevillard^a, Bérangère Evrard^a, Dan Maloney^c, Kiersten M. Ruff^b, Rohit V. Pappu^b, Stefan Wagner^d, Jeanne M. Nerbonne^{e,f}, Jonathan R. Silva^b, R. Reid Townsend^{f,g}, Lars S. Maier^d and Céline Marionneau^{a†}

^aUniversité de Nantes, CNRS, INSERM, l'institut du thorax, F-44000 Nantes, France; ^bDepartment of Biomedical Engineering, Washington University in Saint Louis, MO, USA; ^cBioinformatics Solutions Inc., Waterloo, ON, Canada; ^dDepartment of Internal Medicine II, University Heart Center, University Hospital Regensburg, Regensburg, Germany; Departments of ^eDevelopmental Biology, ^fMedicine and ^gCell Biology and Physiology, Washington University Medical School, Saint Louis, MO, USA.

†Correspondence to: Céline Marionneau, l'institut du thorax, INSERM UMR1087, CNRS UMR6291, IRS-Université de Nantes, 8 Quai Moncousu, BP 70721, 44007 Nantes Cedex 1, France, Tel: +33 2 28 08 01 63, Email: celine.marionneau@univ-nantes.fr

Running Title: Proteomic and functional mapping of cardiac Nav1.5 channel phosphorylation

Proteomic and functional mapping of cardiac Nav1.5 channel phosphorylation

52 **Abstract**

53

54 Phosphorylation of Nav1.5 channels regulates cardiac excitability, yet the phosphorylation sites
55 regulating channel function and the underlying mechanisms remain largely unknown. Using a systematic
56 quantitative phosphoproteomic approach, we analyzed Nav1.5 channel complexes purified from non-
57 failing and failing mouse left ventricles, and we identified 42 phosphorylation sites on Nav1.5. Most sites
58 are clustered, and three of these clusters are highly phosphorylated. Analyses of phosphosilent and
59 phosphomimetic Nav1.5 mutants revealed the roles of three phosphosites in regulating Nav1.5 channel
60 expression and gating. The phosphorylated serines-664 and -667 regulate the voltage-dependence of
61 channel activation in a cumulative manner, whereas phosphorylation of the nearby serine-671, which is
62 increased in failing hearts, decreases cell surface Nav1.5 expression and peak Na⁺ current. No additional
63 roles could be assigned to the other clusters of phosphosites. Taken together, the results demonstrate that
64 ventricular Nav1.5 is highly phosphorylated, and that the phosphorylation-dependent regulation of
65 Nav1.5-encoded channels is highly complex, site-specific and dynamic.

66

67 **Keywords:** Cardiac Nav1.5 channels; phosphoproteomics, native phosphorylation sites; phosphorylation
68 clusters; heart failure

69

70 **Abbreviations:** A, alanine; E, glutamate; HEK-293, Human Embryonic Kidney 293 cells; I_{Na}, peak Na⁺
71 current; I_{NaL}, late Na⁺ current; IP, immunoprecipitation; mαNavPAN, anti-Nav channel subunit mouse
72 monoclonal antibody; MS, Mass Spectrometry; MS1, mass spectrum of peptide precursors; MS2 or
73 MS/MS, fragmentation mass spectrum of peptides selected in narrow mass range (2 Da) from MS1 scan;
74 Nav, voltage-gated Na⁺ channel; pS, phosphoserine; pT, phosphothreonine; S, serine; T, threonine; TAC,
75 Transverse Aortic Constriction; TMT, Tandem Mass Tag.

76

77

78

79

80

81

82

83

84

85

86

87

88

89

90

91

92

93

94

95

96

97

98

99

100

101

102

Proteomic and functional mapping of cardiac Nav1.5 channel phosphorylation

103 **Introduction**

104
105 Voltage-gated Na⁺ (Nav) channels are key determinants of myocardial excitability, and defects in
106 Nav channel expression or functioning in the context of inherited or acquired cardiac disease increase
107 propensity to develop lethal arrhythmias (1). Ventricular Nav channels, composed primarily of the Nav1.5
108 channel pore-forming subunit, in association with several accessory/regulatory proteins, generate the
109 transient, peak Na⁺ current (I_{Na}) responsible for the action potential upstroke and rapid intercellular
110 conduction. While cardiac myocyte Nav channels inactivate quickly, there is a finite probability (~0.5%)
111 of channels remaining open, resulting in the late component of the Na⁺ current (I_{NaL}), which contributes to
112 determining action potential duration. In the ventricular myocardium, the Nav1.5 protein is subject to
113 many post-translational modifications, each of which fine-tunes channel expression and functioning in
114 various physiological and disease contexts. Among the eleven different post-translational modifications
115 previously shown to regulate cardiac Nav1.5 channels, phosphorylation at serine, threonine and tyrosine
116 residues is certainly the best characterized (reviewed in (2), (3-5)).

117 A role for phosphorylation in regulating cardiac Nav1.5 channels was first suggested in a
118 pioneering study demonstrating that β-adrenergic receptors couple to Nav channels not only through a
119 direct G-protein pathway, but also through an indirect, Protein Kinase A (PKA)-dependent pathway (6).
120 The involvement of several additional kinases and phosphatases in regulating both I_{Na} and/or I_{NaL} later
121 spotlighted the functional relevance of cardiac Nav1.5 channel phosphorylation. Perhaps most strikingly,
122 progress in mass spectrometry (MS)-based phosphoproteomic analyses recently buttressed the field by
123 revealing the existence of multiple phosphorylation sites on native ventricular (7,8) and heterologously-
124 expressed (9) Nav1.5 channels. Yet, little is known about the roles and detailed molecular mechanisms
125 that underlie phosphorylation-dependent regulations of cardiac Nav1.5 channels.

126 Phosphorylation of Nav1.5 channels has also recently been suggested as an arrhythmogenic
127 mechanism in heart failure (10-15). The Nav channel defects associated with heart failure are most often
128 characterized by increased I_{NaL} and/or decreased I_{Na}, contributing to action potential prolongation and
129 conduction slowing, respectively (10,14,16-19). The increase in I_{NaL} has reportedly been linked to the
130 activation of kinases, mainly the Ca²⁺/Calmodulin-dependent protein Kinase II (CaMKII) (10,13-15), and
131 several studies have focused on identifying the CaMKII-dependent Nav1.5 phosphorylation sites
132 (7,9,20,21). Notably, increased CaMKII-dependent Nav1.5 phosphorylation at serine-571 has been
133 reported and suggested to increase I_{NaL} in non-ischemic human heart failure (12) and in animal models of
134 heart disease (11,12,14). Nevertheless, Nav1.5 channel phosphorylation may not be the sole mechanism
135 involved in the observed pathophysiological defects, as other evidence suggests roles for upregulation of
136 the neuronal Nav1.1 (18,22), Nav1.6 (18) or Nav1.8 (23) channels. Intensive investigations were also
137 undertaken to understand the causes of the reduced I_{Na}, yet the detailed underlying molecular mechanisms
138 remain unclear. While most studies failed to detect any changes in Nav1.5 transcript or total protein
139 expression in failing human hearts (24) or in animal models of heart failure (17,19), several mechanisms
140 have been suggested to contribute to reduced I_{Na}, including the generation of a C-terminal truncation
141 splicing variant switch in Nav1.5 transcripts (25,26), elevated NADH and reactive oxygen species
142 production (27), or increased intracellular Ca²⁺ concentration and subsequent increased expression of the
143 E3 ubiquitin ligase Nedd4-2 (28). In line with reduced I_{Na}, a recent study using high-resolution imaging
144 and functional techniques showed a reduction in Nav1.5 cluster size and a corresponding decreased
145 number of open channels at the lateral membranes of ventricular myocytes from mice subjected to
146 Transverse Aortic Constriction (TAC), without any changes in Nav1.5 transcript or total protein
147 expression (29).

148 In this study, we investigated the patterns of phosphorylation of native mouse left ventricular
149 Nav1.5 channels and the roles of identified phosphorylation sites in regulating Nav1.5 channel expression
150 and functioning. Using quantitative MS-based phosphoproteomic analyses, we identified and quantified
151 *in situ* the native phosphorylation sites of the Nav1.5 in a mouse model of pressure overload-induced
152 heart failure produced by TAC. By analyzing the expression and the functional properties of
153 phosphosilent and phosphomimetic Nav1.5 mutant channels in human embryonic kidney (HEK-293)

Proteomic and functional mapping of cardiac Na_v1.5 channel phosphorylation

154 cells, as well as simulating the consequences of phosphorylation on Na_v1.5 peptide segment expansion,
155 we identified phosphorylation hot spots for regulation of both channel cell surface expression and gating.
156

157
158
159
160
161
162
163
164
165
166
167
168
169
170
171
172
173
174
175
176
177
178
179
180
181
182
183
184
185
186
187
188
189
190
191
192
193
194
195
196
197
198
199
200
201
202
203
204

Proteomic and functional mapping of cardiac Nav1.5 channel phosphorylation

205 **Results**

206

207 **Purification and characterization of Nav channel complexes from Sham and TAC mouse** 208 **left ventricles**

209 Nav channel complexes from four Sham-operated and five TAC mouse left ventricles were
210 purified by immunoprecipitation (IP) using an anti-NavPAN mouse monoclonal (m α NavPAN) antibody,
211 and characterized using the quantitative isobaric tandem mass tag (TMT)-based analysis. As illustrated in
212 **Figure 1 - Table Supplement 1**, and consistent with previous findings (14), the echocardiographic
213 analysis confirmed increased left ventricular masses (LVM/BW ratios), reduced ejection fractions, but
214 unaltered left ventricular end-diastolic diameters (LVID;d) five weeks after the TAC surgery,
215 demonstrating left ventricular concentric hypertrophy and systolic contractile dysfunction or heart failure
216 in the TAC animals. Western blot analyses of total lysates showed similar total Nav1.5 protein expression
217 in Sham and TAC left ventricles, which resulted in similar Nav1.5 immunoprecipitation yields in the nine
218 samples (**Figure 1 - Figure Supplement 1A**). Isolated Nav channel complexes were then digested with
219 trypsin, and peptide mixtures were labeled with different TMT tags and combined in the same TMT set for
220 multiplexed MS/MS analysis. As illustrated in **Table 1**, the Nav1.5 protein was the most represented
221 protein in the m α NavPAN-IPs, with 310 unique and Nav1.5-specific peptides identified and 56% amino
222 acid sequence coverage (70% with the transmembrane domains removed, **Figure 2**).

223 Consistent with the homogenous yields in the Nav1.5 immunoprecipitation, the relative
224 abundance of the Nav1.5 peptides detected by MS in the nine samples was similar, and used for
225 normalization of each single protein and peptide abundance (**Figure 1 - Figure Supplement 1B**).
226 Accordingly, the distribution of normalized abundance ratios of Nav1.5 peptides (in log₂) in TAC, *versus*
227 Sham, m α NavPAN-IPs was centered on zero (**Figure 1 - Figure Supplement 1C**). Altogether, therefore,
228 these observations attest to a high reproducibility across biological replicates, and a low technical
229 variability inherent to experimental procedures. Of note, and as described previously (30), two Nav1.5
230 peptides differing by the presence or absence of a glutamine (Q) at position-1080 were detected (**Table 1**
231 **& Figure 2**), reflecting the expression of at least two distinct Nav1.5 splice variants in mouse left
232 ventricles; Q1080del corresponding to the commonly reported hH1C variant. Interestingly, these analyses
233 also allowed the identification of eight additional Nav channel pore-forming subunits, among which
234 Nav1.4 is the most abundant, with 86 unique Nav1.4-specific peptides detected (**Table 1**). In addition,
235 several previously identified Nav1.5 channel associated/regulatory proteins, including calmodulin, the VY
236 variant of Fibroblast growth factor Homologous Factor 2 (FHF2-VY) and ankyrin-G, were detected, with
237 no significant differences in abundance between Sham and TAC m α NavPAN-IPs (**Table 1**).

238

239 **Identification and quantification of 42 Nav1.5 phosphorylation sites in Sham and TAC** 240 **mouse left ventricles**

241 The phosphoproteomic analysis of the m α NavPAN-IPs from Sham and TAC mouse left
242 ventricles allowed the unambiguous identification of 42 native phosphorylation sites in the Nav1.5
243 protein, 22 of which have never, to our knowledge, been previously described in native cardiac tissues
244 (**Figures 1A & 2**). **Table 2** lists the phosphopeptides enabling the best phosphorylation site assignment(s)
245 for each phosphorylation site; and corresponding MS/MS spectra are presented in **Table 2 - Figure**
246 **Supplement 1**. Interestingly, the vast majority of these phosphorylation sites are clustered, with the first
247 intracellular linker loop of Nav1.5 revealed as a hot spot for phosphorylation, with a total of 21 sites
248 identified. Further label-free quantitative analysis of the areas of extracted MS1 peptide ion
249 chromatograms revealed large differences in the relative abundances of the individual phosphopeptides,
250 and the existence of three highly phosphorylated clusters at positions S457 to S460, S483 to T486, and
251 S664 to S671 (**Figure 1B**). In addition, and in contrast to the other phosphorylation sites, the
252 phosphorylated peptides assigning these three phosphorylation clusters are more abundant than their non-
253 phosphorylated counterparts, suggesting that these sites are mostly phosphorylated in native Nav1.5
254 channels in wild-type mouse left ventricles. Looking into the detailed quantification of single

Proteomic and functional mapping of cardiac Nav1.5 channel phosphorylation

255 phosphorylation sites inside each of these clusters, however, major differences in phosphopeptide
256 abundance are evident (**Figure 1 - Figure Supplement 2**). This is the case, for example, of
257 phosphorylation at S664 or S667, which is about 10-fold more abundant than at residues T670 or S671.

258 To determine whether phosphorylation of Nav1.5 is regulated in heart failure, the relative
259 abundance of each Nav1.5 phosphopeptide in TAC, *versus* Sham, α NavPAN-IPs was calculated using
260 the relative abundance of TMT reporter ions. As illustrated in **Figure 1C**, peptides exhibiting
261 phosphorylation(s) on serine-671 (S671) alone or in combination with serines-664 (S664 + S671) or -667
262 (S667 + S671) are significantly more abundant in the TAC, compared with the Sham, α NavPAN-IPs.
263 The relative abundances of their non-phosphorylated counterparts, however, are similar in Sham and TAC
264 α NavPAN-IPs (data not shown). Additionally, none of the other Nav1.5 phosphopeptides showed any
265 significant differences in the Sham and TAC α NavPAN-IPs (**Table 2**). In addition to Nav1.5, four
266 phosphorylation sites on Nav1.4 and one on Nav1.3 could also be detected (**Table 2 - Table Supplement**
267 **1 & Figure Supplement 1**). Taken together, these quantitative phosphoproteomic analyses identified 42
268 native phosphorylation sites on Nav1.5, among which three clusters of phosphorylation in the first loop of
269 the channel are highly phosphorylated, and one serine at position-671 shows increased phosphorylation in
270 TAC left ventricles.

271

272 **Functional mapping of Nav1.5 channel phosphorylation clusters**

273 The identification of several clusters of phosphorylation sites on Nav1.5 suggests that these sites
274 may be involved in the coordinated regulation of channel expression and/or function. Out of the eight
275 clusters of phosphorylation identified in the mouse Nav1.5 protein, seven are conserved in the human
276 Nav1.5 protein sequence; only the mouse T1105 is not conserved (**Figure 3 - Figure Supplement 1**). In
277 order to investigate the functional roles of these (seven) phosphorylation clusters, phosphosilent and
278 phosphomimetic Nav1.5 channel constructs in the human Nav1.5 hH1C cDNA sequence were generated,
279 transiently expressed in HEK-293 cells, and characterized in whole-cell voltage-clamp recordings. In the
280 phosphosilent constructs, mutations were introduced to replace serines/threonines with alanines, whereas
281 in the phosphomimetic constructs, mutations were introduced to substitute glutamates for
282 serines/threonines, to mimic phosphorylation.

283 As illustrated in **Figure 3B**, these whole-cell voltage-clamp analyses demonstrated that the
284 voltage-dependence of activation of Nav1.5-S664-671A phosphosilent channels is significantly ($p < 0.001$)
285 shifted towards depolarized potentials, compared to WT channels (see distributions, detailed properties
286 and statistics in **Figure 3 - Figure Supplement 2A & Table Supplement 1**). The activation curve of the
287 Nav1.5-S664-671E phosphomimetic channel was also significantly ($p < 0.001$) shifted, although to a lesser
288 extent, when compared with the phosphosilent channel. Together, therefore, these findings suggest that
289 the S664-671 cluster is phosphorylated in HEK-293 cells, and that disruption of phosphorylation at these
290 sites shifts the voltage-dependence of channel activation towards depolarized potentials. In addition, the
291 time to peak Na⁺ current (**Figure 3D**), as well as the inactivation time constants, τ_{fast} and τ_{slow} (**Figures 3E**
292 **& 3F**), were shifted towards depolarized potentials until reaching full activation at ~ 0 mV. The peak Na⁺
293 current density of the Nav1.5-S664-671E phosphomimetic channel was significantly ($p < 0.05$) reduced
294 compared to the WT channel, whereas no significant changes were observed with the Nav1.5-S664-671A
295 phosphosilent channel (**Figure 3C**, see distributions at -20 mV and statistics in **Figure 3 - Figure**
296 **Supplement 2B & Table Supplement 1**). In contrast, the voltage-dependence of steady-state inactivation
297 (**Figure 3B**) and the kinetic of recovery from inactivation (**Figure 3 - Figure Supplement 2D & Table**
298 **Supplement 1**) of both S664-671 phosphomutant channels were not changed. Additionally, and to our
299 surprise, no differences in current densities, or in the kinetics or voltage-dependences of current activation
300 and inactivation, or in the kinetics of recovery from inactivation were observed for any of the six other
301 heterologously-expressed (in HEK-293 cells) paired phosphosilent or phosphomimetic Nav1.5 channels
302 (**Figure 3 - Figure Supplement 2 & Table Supplement 1**). Taken together, therefore, these analyses
303 revealed a key role for phosphorylation at S664-671 in regulating the voltage-dependence of Nav1.5

Proteomic and functional mapping of cardiac Nav1.5 channel phosphorylation

304 channel activation and peak Na⁺ current density, whereas regulation mediated by the other
305 phosphorylation sites investigated most likely involve more complex mechanisms.

306
307 **Phosphorylation at S664 and S667 shifts the voltage-dependence of current activation**
308 **towards hyperpolarized potentials whereas phosphorylation at S671 decreases the peak Na⁺ current**
309 **density**

310 To decipher the respective contributions of the S664, S667, T670 and S671 phosphorylation sites
311 in regulating the voltage-dependence of current activation and peak Na⁺ current density, each of these
312 serines/threonine was mutated individually to alanine or glutamate, and the densities and properties of
313 Na⁺ currents from single phosphosilent or phosphomimetic channels were examined in transiently
314 transfected HEK-293 cells. These analyses showed that the voltage-dependences of activation of the
315 Nav1.5-S664 (**Figure 4A**) and Nav1.5-S667 (**Figure 4B**) phosphomutant channels are significantly
316 ($p < 0.001$) shifted towards depolarized potentials, compared to the WT channels, whereas no changes
317 were observed with the Nav1.5-T670 or Nav1.5-S671 phosphomutant channels (**Figures 4C & 4D**, see
318 detailed properties and statistics in **Figure 4 - Table Supplement 1**). Of note, the ~6 mV shifts observed
319 with the single Nav1.5-S664 and Nav1.5-S667 phosphomutant channels were two-fold smaller than the
320 ~10 mV shift obtained with the quadruple Nav1.5-S664-671A phosphosilent channel, suggesting that the
321 effects at S664 and S667 are additive. Additionally, these analyses revealed that sole the Nav1.5-S671E
322 phosphomimetic channel shows a significant ($p < 0.05$) decrease in peak Na⁺ current density (**Figure 4H**),
323 whereas none of the other single phosphomutant channels showed any significant differences (**Figures**
324 **4E, 4F & 4G**).

325 Because phosphorylation at S671 was found to be increased in the TAC, compared with the
326 Sham, α NavPAN-IPs (**Figure 1C**), and because it was previously suggested that phosphorylation of
327 Nav1.5 may mediate increased I_{NaL} in heart failure (10-15), additional voltage-clamp experiments were
328 designed to test whether phosphorylation at S671 regulates I_{NaL} . These analyses showed that none of the
329 single mutations at S671, or quadruple mutations at S664-671 affect TTX-sensitive I_{NaL} density in HEK-
330 293 cells (**Figure 4 - Figure Supplement 1**). Altogether, therefore, these analyses suggest that
331 phosphorylation at S664 and S667 shifts the voltage-dependence of current activation towards
332 hyperpolarized potentials in a cumulative manner, whereas phosphorylation at S671 decreases the peak
333 Na⁺ current density.

334
335 **Phosphorylation at S671 decreases the cell surface expression of Nav1.5 channels**

336 Additional cell surface biotinylation experiments in transiently transfected HEK-293 cells were
337 designed to determine whether phosphorylation at S671 regulates the cell surface expression of the
338 Nav1.5 channel protein. Interestingly, these experiments revealed that the cell surface expression of the
339 Nav1.5-S671E phosphomimetic channel is significantly ($p < 0.001$) decreased, compared with the WT or
340 the Nav1.5-S671A phosphosilent channels, whereas no differences in total Nav1.5 protein expression
341 were observed (**Figures 5A & 5B**). Importantly, the decrease observed with the phosphomimetic mutant,
342 compared with the phosphosilent mutant, suggests that not only this channel locus, but most probably
343 phosphorylation at this particular site, underlies the observed decrease in cell surface expression.
344 Together with the electrophysiological findings, therefore, these biochemical analyses demonstrate a key
345 role for S671 in regulating the cell surface expression of Nav1.5, and suggest that phosphorylation at this
346 site decreases the cell surface expression of Nav1.5-encoded channels.

347
348 **Simulated consequences of phosphorylation on the first intracellular linker loop of Nav1.5**

349 Like many heavily phosphorylated protein segments (31,32), the first two intracellular linker
350 loops of Nav1.5 are predicted to be intrinsically disordered. Conformational heterogeneity is one of the
351 defining hallmarks of intrinsically disordered regions (IDRs). Heterogeneity is manifest in the amplitude
352 of fluctuations of overall size, shape, and local secondary structural preferences. There is growing
353 recognition of sequence-specificity whereby the ensembles accessible to an IDR are governed by the
354 amino acid composition, extent of phosphorylation, and patterning of residues within the linear sequence.

Proteomic and functional mapping of cardiac Nav1.5 channel phosphorylation

355 These sequence-ensemble relationships can be uncovered using all atom simulations. Given the disparate
356 timescales and length scales involved, a robust and efficient approach is to use Markov Chain Metropolis
357 Monte Carlo (MC) simulations based on the ABSINTH implicit solvent model as implemented in the
358 CAMPARI simulation (33-35). Here, we used simulations to quantify sequence-ensemble relationships
359 for the first intracellular linker loop of human Nav1.5 containing the phosphorylation clusters S457-460,
360 S483-486, S497-499, and S664-671 identified by mass spectrometry. For our simulations, we used
361 segments between thirty and forty residues in length, containing each cluster in an approximately central
362 position (441-480 for S457-460, 465-501 for S483-486, 481-515 for S497-499, 651-684 for S664-671).
363 For each cluster, we performed simulations for the WT sequence, as well as phosphomimetic mutations
364 where serine(s)/threonine(s) are replaced with glutamate(s). The results of simulations were analyzed
365 using the device of internal scaling plots. These plots quantify the variation of ensemble-averaged
366 distances between residues i and j as a function of sequence separation $|j-i|$. Multiple pairs of residues
367 contribute to a given sequence separation $|j-i|$. The internal scaling profiles can be calibrated against
368 reference profiles that pertain to two kinds of random-coil ensembles. These are designated as EV for
369 excluded volume, which pertains to profiles extracted for self-avoiding walks, and FRC for Flory random
370 coil, which pertains to profiles extracted Flory random coils. Details of these reference ensembles have
371 been published elsewhere.

372 Simulations of the 441-480 segment showed that the conformational preferences of the
373 unphosphorylated (WT) peptide are akin to those of the FRC reference (**Figure 6A**). This implies that
374 sequence encodes a conformational averaging whereby the peptide-solvent and peptide-peptide
375 interactions are mutually compensatory, thereby giving rise to an ensemble that is maximally
376 heterogeneous. Introduction of phosphomimetic substitutions S457E, S459E and/or S460E did not have a
377 large effect on the ensemble-averaged internal scaling profiles when compared to the unmodified
378 sequence. We obtained similar results for the 465-501 segment, which is also largely unaffected by the
379 introduction of the phosphomimetic mutation(s) of the S483-486 cluster (**Figure 6B**). Conversely, the
380 481-515 and 651-684 segments were noticeably sensitive to the addition of the negative charges (**Figures**
381 **6C & 6D**). When unphosphorylated, these segments preferred conformations that are considerably more
382 compact than the FRC reference. Upon the introduction of cumulative phosphomimetic mutations, these
383 segments gradually expanded in the direction of the EV limit.

384 Taken together, the results suggest that the intrinsic conformational preferences of the WT
385 sequence dictate the extent of responsiveness of the conformational ensemble to multisite
386 phosphorylation. Sequence stretches that have an intrinsic preference for FRC-like conformations are
387 relatively insensitive to phosphomimetic substitutions of serine/threonine residues. This insensitivity has
388 been quantified for IDRs that undergo multisite phosphorylation (36). In contrast, sequences that have an
389 intrinsic preference for compact conformations become responsive to phosphomimetic substitutions. This
390 would appear to derive from the increased fraction of charged residues (which engenders preferential
391 solvation) and electrostatic repulsions (34). The fraction of charged residues (FCR) and the net charge per
392 residue (NCPR) are known to be direct determinants of the conformational preferences of IDRs (37).
393 Both the 441-480 and 465-501 segments have a higher FCR than the 481-515 and 651-684 segments. The
394 addition of a single negative charge would lead to a greater percent increase in the FCR of the 481-515
395 and 651-684 segments than it would for the 441-480 and 464-501 segments. As the latter are already
396 expanded, additional charges do not have a large impact on the conformational preference. The more
397 compact starting point of the former allows the phosphomimetic mutations to have a greater effect. While
398 the results for three of the clusters were consistent with the experimental data, those for the S497-499
399 cluster present an apparent inconsistency. These observations suggest that the ability of this segment to
400 expand due to the addition of charge is not connected to channel gating. Together with the
401 electrophysiological analyses, therefore, these simulations suggest that the effect of phosphorylation at
402 S664 and S667 on the voltage-dependence of channel activation is mediated by the expansion of the area
403 containing the phosphorylation sites, and that this expansion is likely to regulate channel activation
404 allosterically.

405

Proteomic and functional mapping of cardiac Nav1.5 channel phosphorylation

406 **Discussion**

407
408 The results presented here provide a novel, detailed phosphorylation map of the native mouse left
409 ventricular Nav1.5 channel protein, and identify the functional roles of three of these phosphorylation
410 sites in regulating the expression and gating properties of Nav1.5-encoded channels. The highly
411 phosphorylated S664 and S667 shift the voltage-dependence of channel activation towards hyperpolarized
412 potentials in an additive manner, whereas phosphorylation at S671, which is increased in TAC mouse left
413 ventricles, decreases Nav1.5 cell surface expression and peak Na⁺ current density. No additional roles
414 could be assigned to the other clusters of Nav1.5 phosphorylation sites, suggesting additional complexity
415 in the mechanisms mediating the phosphorylation-dependent regulation of cardiac Nav1.5 channels.

416 417 **Phosphorylation map of native mouse left ventricular Nav1.5 channels**

418 The present phosphoproteomic analysis confidently identified a total of 42 native phosphorylation
419 sites in the Nav1.5 channel protein purified from mouse left ventricles, of which 22 are novel. Seventeen
420 of these sites were also found to be phosphorylated in heterologously-expressed Nav1.5 channels (9),
421 suggesting that about half of this phosphorylation pattern is conserved among species (mouse and human)
422 and cellular systems (native channels in left ventricles and recombinant channels in HEK-293 cells),
423 whereas the other half may be associated with more specific and/or localized regulation. Among the sites
424 identified, only six were previously suggested to be the targets for specific kinases using *in silico* and/or
425 *in vitro* analyses: S36 and S525 were attributed to the regulation by PKA, S484 and S664 were assigned
426 to the Serum- and Glucocorticoid-inducible Kinase 3 (SGK3), and S516 and S571 were ascribed to
427 CaMKII (reviewed in (2)). In marked contrast, several previously described phosphorylation sites were
428 not detected in the present study, including the PKA-dependent S528, the CaMKII-associated T594, the
429 Protein Kinase C (PKC)-dependent S1503, the Adenosine Monophosphate-activated Protein Kinase
430 (AMPK)-dependent T101 (38), and the six Fyn-dependent tyrosines (39,40).

431 Strikingly, and consistent with previous studies from our laboratory (7,8) and the Bers group (9),
432 the results obtained and presented here again revealed that the first intracellular linker loop of Nav1.5 is a
433 hotspot for phosphorylation, with a total of 21 sites identified. Comparisons of the relative abundances of
434 the phosphopeptides identified three highly abundant (and highly phosphorylated) clusters of
435 phosphorylation sites in the first intracellular linker loop of Nav1.5 in mouse left ventricles. The simplest
436 interpretation of this finding is that these three phosphorylation clusters, at positions S457 to S460, S483
437 to T486, and S664 to S671, are likely involved in regulating the basal and/or gating properties of native
438 cardiac Nav1.5 channels. Conversely, the other phosphorylation sites, with lower stoichiometries, may
439 play spatially- or temporally-distinct roles in the physiological or more pathophysiological regulation of
440 channel expression or gating. This suggestion is highlighted for residue S671, for example, which is
441 substantially (10-fold) less phosphorylated than the nearby S664 and S667 residues in WT mouse left
442 ventricles, but is (2-fold) upregulated in TAC left ventricles. Remarkably, this mass spectrometry analysis
443 also revealed that the vast majority of identified phosphorylation sites (at least 26) are clustered,
444 suggesting concomitant phosphorylation and roles in regulating channel expression and/or function.
445 Unexpectedly, however, except for S664, S667 and S671, no apparent effects of phosphomimetic or
446 phosphosilent mutations were observed on heterologously-expressed (in HEK-293 cells) Nav1.5 current
447 densities or biophysical properties, suggesting a greater complexity than anticipated in the mechanisms
448 contributing to phosphorylation-dependent regulation of Nav1.5 channels.

450 **Phosphorylation at S664 and S667 shifts the voltage-dependence of Nav1.5 channel** 451 **activation towards hyperpolarized potentials**

452 The electrophysiological analyses presented here identified key roles of S664 and S667 in
453 regulating the voltage-dependence of Nav1.5 channel activation. Indeed, the data demonstrate that the
454 voltage-dependence of activation of quadruple phosphosilent channels at positions S664-671 is shifted
455 towards depolarized potentials, compared to WT channels, whereas phosphomimetic channels display a
456 smaller shift. These findings are consistent with WT channels being phosphorylated at S664 and S667 in

Proteomic and functional mapping of cardiac Nav1.5 channel phosphorylation

457 HEK-293 cells, as previously reported (9), and suggest that disruption of phosphorylation at these sites
458 impact channel gating. Confounding this simple interpretation of the data is the fact that glutamate
459 substitution only partially mimics phosphorylation.

460 Further analyses of the roles of each of the four phosphorylation sites in this cluster revealed the
461 specific involvement of S664 and S667 in regulating gating, whereas modifying T670 or S671 was
462 without effects. Single glutamate mutations at S664 and S667, however, produce the same effects as the
463 single phosphosilent channels. These findings could be attributed to the fact that the side chain of the
464 glutamate only has a single negative charge and a small hydrated shell, which is quite distinct from the
465 covalently attached phosphate group characterized by a doubly negative charge and a large hydrated shell
466 (41). It is likely, therefore, that one glutamate (in single phosphomimetic channels) is not sufficient to
467 mimic phosphorylation at this locus, and that two glutamates (in the quadruple phosphomimetic channel)
468 only partially mimic phosphorylation. The fact that the shifts induced by the single phosphosilent
469 mutations are half the shift generated by the quadruple mutation further supports this hypothesis, and
470 suggests that regulation involving these two sites is cumulative and most likely concomitant.
471 Nevertheless, further investigations, aimed at demonstrating the role of phosphorylation, rather than any
472 other structural determinants associated with this locus, are certainly warranted. In this regard, our
473 findings are also in accordance with previous data reporting the role of SGK3 in shifting the voltage-
474 dependence of channel activation towards more hyperpolarized potentials in *Xenopus* oocytes, whereas
475 the opposite effect was observed with the Nav1.5-S664A phosphosilent channel (42). Although the
476 involvement of SGK3 and S664 in a shared regulation was not directly shown in this previous study, it is
477 tempting to speculate that SGK3 may constitute the kinase phosphorylating S664 and S667 and mediating
478 this regulation.

479 The effects of phosphorylation were also analyzed using all-atom simulations approach to
480 determine how the introduction of negative charges affects the conformational ensemble of the segments
481 containing the phosphorylation clusters identified by mass spectrometry. These simulations demonstrate
482 that the introduction of negative charges at positions S497-S499 and S664-671 could expand the structure
483 of the containing segments, whereas no effects are likely with the segments containing the S457-460 and
484 S483-486 phosphorylation clusters. Furthermore, for both of the affected segments, the expansion likely
485 gradually increases with the cumulative addition of charges. Interestingly, the simulation findings are
486 consistent with the additive roles of S664 and S667 in regulating the voltage-dependence of channel
487 activation observed in the electrophysiological analyses. Consistent with the proximity of the S664-671
488 phosphorylation cluster to the DII voltage-sensing domain (DII-VSD) of Nav1.5, which is tightly linked
489 to channel activation (43), our findings suggest that phosphorylation at S664 and S667 regulates channel
490 activation through the expansion of the C-terminal extremity of the first intracellular linker loop of the
491 channel. However, no effects on channel gating were observed with the S497-499 phosphomimetic
492 mutant, even though the simulation showed an effect on its ability to expand. This result suggests that the
493 expansion of this segment, which is more distal to the DII-VSD, does not regulate channel gating.

494 495 **Phosphorylation at S671 decreases Nav1.5 channel cell surface expression and peak Na⁺** 496 **current density**

497 The functional analyses also demonstrate that mimicking phosphorylation at S671 decreases the
498 expression of the Nav1.5 protein at the cell surface, as well as peak Na⁺ current density in HEK-293 cells.
499 These results suggest that S671 is not phosphorylated in HEK-293 cells, which is in agreement with the
500 previously published mass spectrometric analyses (9). While the phosphomimetic mutation greatly
501 decreases the cell surface expression of Nav1.5, the phosphosilent mutation also reduces Nav1.5 surface
502 expression, albeit to a much smaller extent. These confounding results suggest that the regulation
503 mediated by this locus highly depends on structural changes, and that the phosphomimetic mutation
504 affects the cell surface expression of the channel in part through a change in the structure of the locus.
505 One could further suggest that the greater effect of the phosphomimetic channel may be caused by
506 additional attributes common to the phosphate group and the glutamate side chain. Together, therefore,

Proteomic and functional mapping of cardiac Nav1.5 channel phosphorylation

507 these findings highlight the novel role of this locus, and of phosphorylation at this site, in regulating the
508 cell surface expression of Nav1.5 channels.

509 Interestingly, the mass spectrometric analyses also revealed that phosphorylation at this site is
510 increased in the left ventricles of TAC mice, suggesting a role in mediating the Nav channel defects
511 associated with heart failure. Because previous studies have suggested that CaMKII-dependent
512 phosphorylation of Nav1.5 may constitute one of the molecular mechanisms mediating the increased late
513 Na⁺ current in heart failure (10-15), this finding prompted us to examine the late Na⁺ current generated by
514 the phosphosilent and phosphomimetic Nav1.5 mutants at position-671. Our results herein appeared
515 negative, although it cannot be excluded that this regulation may require a specific molecular and cellular
516 environment which is not recapitulated in HEK-293 cells. Additionally, and to our surprise, no changes in
517 phosphorylation at S571 were observed in our TAC model, in contrast with previous findings in
518 nonischemic human heart failure (12) and in several animal models of heart disease (11,12,14). These
519 seemingly disparate findings may reflect technical and/or experimental differences, including differences
520 in the models used and/or stages of disease.

521 The results presented here raise the interesting and novel possibility that increased
522 phosphorylation at S671 participates in decreasing the peak Na⁺ current often observed in heart failure.
523 Consistent with this suggestion, a recent study by the Remme group, using superresolution microscopy,
524 showed a reduction in the size of Nav1.5 clusters in TAC ventricular myocytes without any changes in
525 Nav1.5 transcript or total protein expression (29). Although further studies will be required to determine
526 directly whether these observations are causally linked to increased phosphorylation at S671, the results
527 here provide new hints towards understanding the molecular basis of the decreased peak Na⁺ current in
528 heart failure.

529 Altogether, the results presented here demonstrate that native mouse ventricular Nav1.5 is highly
530 phosphorylated, and that the mechanisms mediating the phosphorylation-dependent regulation of Nav1.5-
531 encoded channels are site-specific, complex, dynamic, and lead to diverse physiological and/or
532 pathological consequences on both channel gating and expression.

533
534
535
536
537
538
539
540
541
542
543
544
545
546
547
548
549
550
551
552
553
554
555
556
557

Proteomic and functional mapping of cardiac Nav1.5 channel phosphorylation

558 **Materials and methods**

559

560 **Statement on the use of murine tissue**

561 All investigations conformed to directive 2010/63/EU of the European Parliament, to the Guide
562 for the Care and Use of Laboratory Animals published by the US National Institutes of Health (NIH
563 Publication No. 85-23, revised 1985) and to local institutional guidelines.

564

565 **Animal model of heart failure**

566 Heart failure was induced by transverse aortic constriction (TAC) as described previously (14).
567 Eight-week-old male C57/BL6J mice were anesthetized using intraperitoneal injections of medetomidine
568 (0.5 mg/kg), midazolam (5 mg/kg) and fentanyl (0.05 mg/kg body weight). A horizontal incision (1-1.5
569 cm) at the jugulum was used to display the transverse aorta, and a 27-gauge needle was tied against the
570 aorta using a 6.0 non-absorbable suture. After removal of the 27-gauge needle, the skin was closed, and
571 the mice were kept on a heating plate until recovered from the anesthesia. Sham animals underwent the
572 same procedure except for the banding of the transverse aorta. At the end of the surgery, anesthesia was
573 antagonized using intraperitoneal injections of atipamezol (2.5 mg/kg), flumazenil (0.5 mg/kg) and
574 buprenorphine (0.1 mg/kg body weight). For analgesia, metamizole (1.33 mg/ml) was added to the
575 drinking water 2 days before surgery, and supplied for 7 days after operation. In addition, buprenorphine
576 (60 µg/kg body weight) was administered s.c. 1 hr before surgery. A TAC with a mean gradient of less
577 than 5 mmHg was deemed insufficient to induce heart failure and, if observed, the animal was excluded
578 from later analysis. Mice were sacrificed 5 weeks after TAC by cervical dislocation, and left ventricles
579 were harvested, flash-frozen and stored for further analyses.

580

581 **Mouse echocardiography**

582 Transthoracic echocardiography was performed blinded before and 5 weeks after TAC using a
583 Vevo3100 system (VisualSonics, Toronto, Canada) equipped with a 30-MHz center frequency transducer,
584 as described previously (14). The animals were initially anesthetized with 3% isoflurane, while
585 temperature-, respiration-, and electrocardiogram-controlled anesthesia was maintained with 1.5%
586 isoflurane. Two-dimensional cine loops with frame rates of >200 frames/sec of a long axis view and a
587 short axis view at mid-level of the papillary muscles, as well as M-mode loops of the short axis view were
588 recorded. Thicknesses of the anterior (LVAW) and posterior (LVPW) walls of the left ventricle, the inner
589 diameter of the left ventricle (LVID), and the area of the left ventricular cavity were measured in systole
590 (s) and diastole (d) from the short axis view according to standard procedures (44). Maximal left
591 ventricular length was measured from the long axis view. Systolic and diastolic left ventricular volumes
592 (LV vol) were calculated using the area-length method, and the ejection fraction (EF) was derived. Left
593 ventricular mass (LVM) was calculated from anterior and posterior wall thicknesses using Vevo LAB
594 Software (VisualSonics). PW Doppler ultrasound was used to assess mean gradients (MG) 3 days after
595 the TAC procedure.

596

597 **Immunoprecipitation of Nav channel complexes**

598 Flash-frozen left ventricles from 4 Sham and 5 TAC mice were homogenized individually in ice-
599 cold lysis buffer containing 20 mM HEPES (pH 7.4), 150 mM NaCl, 0.5% amidosulfobetaine, 1X
600 complete protease inhibitor cocktail tablet, 1 mM phenylmethylsulfonyl fluoride (PMSF), 0.7 µg/ml
601 pepstatin A (Thermo Fisher Scientific, Waltham, MA) and 1X Halt phosphatase inhibitor cocktail
602 (Thermo Fisher Scientific) as described previously (8). All reagents were from Sigma (Saint Louis, MO)
603 unless otherwise noted. After 15-min rotation at 4°C, 8 mg of the soluble protein fractions were pre-
604 cleared with 200 µL of protein G-magnetic Dynabeads (Thermo Fisher Scientific) for 1 hr, and
605 subsequently used for immunoprecipitations (IP) with 48 µg of an anti-NavPAN mouse monoclonal
606 antibody (mαNavPAN, Sigma, #S8809), raised against the SP19 epitope (45) located in the third
607 intracellular linker loop and common to all Nav channel pore-forming subunits. Prior to the IP, antibodies

Proteomic and functional mapping of cardiac Nav1.5 channel phosphorylation

608 were cross-linked to 200 μ l of protein G-magnetic Dynabeads using 20 mM dimethyl pimelimidate
609 (Thermo Fisher Scientific) (46). Protein samples and antibody-coupled beads were mixed for 2 hrs at 4°C.
610 Magnetic beads were then collected, washed rapidly four times with ice-cold lysis buffer, and isolated
611 protein complexes were eluted from the beads in 1X SDS sample buffer (Bio-Rad Laboratories, Hercules,
612 CA) at 60°C for 10 min. Ninety-nine percent of the immunoprecipitated mouse left ventricular Nav
613 channel protein complexes were analyzed by MS, and the remaining one percent was used to verify IP
614 yields by western blotting using a rabbit polyclonal anti-Nav1.5 antibody (Rb α Nav1.5, 1:1000, Alomone
615 labs, Jerusalem, Israel, #ASC-005).

616 617 **Peptide preparation and isobaric labeling for LC-MS**

618 The IP eluates were thawed on ice, reduced, and denatured by heating for 10 min at 95°C. The
619 Cys residues were alkylated with iodoacetamide (10 mM) for 45 min at room temperature in the dark. The
620 peptides were prepared using a modification (47) of the filter-aided sample preparation method (48).
621 After the addition of 300 μ L of 100 mM Tris buffer (pH 8.5) containing 8 M urea (UT) and vortexing, the
622 samples were transferred to YM-30 filter units (Millipore, MRCF0R030) and spun for 14 min at 10,000
623 rcf (Eppendorf, Model No. 5424). The filters were washed with 200 μ l of UT buffer, and the spin-wash
624 cycle was repeated twice. The samples were then exchanged into digest buffer with the addition of 200
625 μ L of 50 mM Tris buffer, pH 8.0, followed by centrifugation (10,000 rcf for 10 min). After transferring
626 the upper filter units to new collection tubes, 80 μ L of digest buffer was added, and the samples were
627 digested with trypsin (1 μ g) for 4 h at 37°C. The digestion was continued overnight after adding another
628 aliquot of trypsin. The filter units were then spun for 10 min (10,000 rcf) in an Eppendorf
629 microcentrifuge. The filter was washed with 50 μ L of Tris buffer (100 mM, pH 8.0), followed by
630 centrifugation. The digests were extracted three times with 1 ml of ethyl acetate, and acidified to 1%
631 trifluoroacetic acid (TFA) using a 50% aqueous solution. The pH was < 2.0 by checking with pH paper.
632 The solid phase extraction of the peptides was performed using porous graphite carbon micro-tips (49).
633 The peptides were eluted with 60% acetonitrile in 0.1% TFA, and pooled for drying in a Speed-Vac
634 (Thermo Scientific, Model No. Savant DNA 120 concentrator) after adding TFA to 5%. The peptides
635 were dissolved in 20 μ L of 1% acetonitrile in water. An aliquot (10%) was removed for quantification
636 using the Pierce Quantitative Fluorometric Peptide Assay kit (Thermo Scientific, Cat. No. 23290). The
637 remainder of the peptides from each IP samples (~0.5-3.5 μ g) and 1.16 μ g of reference pool peptide were
638 transferred into a new 0.5 mL Eppendorf tube, dried in the Speed-Vac, and dissolved in 12 μ L of HEPES
639 buffer (100 mM, pH 8.0, Sigma, H3537).

640 The samples were labeled with tandem mass tag reagents (TMT11, Thermo Scientific) according
641 to manufacturer's protocol. The labeled samples were pooled, dried, and resuspended in 120 μ L of 1%
642 formic acid (FA). The TMT11 labeled sample was desalted as described above for the unlabeled peptides.
643 The eluates were transferred to autosampler vials (Sun-Sri, Cat. No. 200046), dried, and stored at -80°C
644 for capillary liquid chromatography interfaced to a mass spectrometer (nano-LC-MS).

645 646 **Nano-LC-MS**

647 The samples in formic acid (1%) were loaded (2.5 μ L) onto a 75 μ m i.d. \times 50 cm Acclaim®
648 PepMap 100 C18 RSLC column (Thermo-Fisher Scientific) on an EASY nano-LC (Thermo Fisher
649 Scientific). The column was equilibrated using constant pressure (700 bar) with 20 μ L of solvent A (0.1%
650 FA). The peptides were eluted using the following gradient program with a flow rate of 300 nL/min and
651 using solvents A and B (acetonitrile with 0.1% FA): solvent A containing 5% B for 1 min, increased to
652 25% B over 87 min, to 35% B over 40 min, to 70% B in 6 min and constant 70% B for 6 min, to 95% B
653 over 2 min and constant 95% B for 18 min. The data were acquired in data-dependent acquisition (DDA)
654 mode. The MS1 scans were acquired with the Orbitrap™ mass analyzer over $m/z = 375$ to 1500 and
655 resolution set to 70,000. Twelve data-dependent high-energy collisional dissociation spectra (MS2) were
656 acquired from each MS1 scan with a mass resolving power set to 35,000, a range of $m/z = 100 - 1500$, an
657 isolation width of 2 Th, and a normalized collision energy setting of 32%. The maximum injection time

Proteomic and functional mapping of cardiac Nav1.5 channel phosphorylation

658 was 60 ms for parent-ion analysis and 120 ms for product-ion analysis. The ions that were selected for
659 MS2 were dynamically excluded for 20 sec. The automatic gain control (AGC) was set at a target value
660 of 3e6 ions for MS1 scans and 1e5 ions for MS2. Peptide ions with charge states of one or ≥ 7 were
661 excluded for higher-energy collision-induced dissociation (HCD) acquisition.

662

663 MS data analysis

664 Peptide identification from raw MS data was performed using PEAKS Studio 8.5 (Bioinformatics
665 Solutions Inc., Waterloo, Canada) (50). The Uni-mouse-Reference-20131008 protein database was used
666 for spectral matching. The precursor and product ion mass tolerances were set to 20 ppm and 0.05 Da,
667 respectively, and the enzyme cleavage specificity was set to trypsin, with a maximum of three missed
668 cleavages allowed. Carbamidomethylation (Cys) and TMT tags (Lys and/or peptide N-terminus) were
669 treated as fixed modifications, while oxidation (Met), pyro-glutamination (Gln), deamidation (Asn and/or
670 Gln), methylation (Lys and/or Arg), dimethylation (Lys and/or Arg), acetylation (Lys) and
671 phosphorylation (Ser, Thr and/or Tyr) were considered variable modifications. The definitive annotation
672 of each Nav1.5 phosphopeptide-spectrum match was obtained by manual verification and interpretation.
673 The phosphorylation site assignments were based on the presence or absence of the unphosphorylated and
674 phosphorylated b- and y-ions flanking the site(s) of phosphorylation, ions referred to as site-
675 discriminating ions throughout this study. When site-discriminating ions were not all detected, the
676 assignment of phosphorylation sites was narrowed down to several possibilities by elimination (for
677 example, pS1056 and/or pT1058). Representative MS/MS spectra, PEAKS -10lgP scores, mass errors of
678 parent ions (in ppm) and charge state confirmations of site-discriminating b- and y-ions are presented in
679 **Table 2, Table 2 - Table Supplement 1 & Figure Supplement 1.**

680 The protein and peptide relative abundances in TAC, *versus* Sham, α NavPAN-IPs were
681 calculated using quantification of TMT reporter ions. Reporter ion intensities in each TMT channel were
682 normalized to the mean reporter ion intensities of Nav1.5-derived peptides (normalization to spike) to
683 correct for differences in IP yields and technical variabilities. Normalization factors are presented in
684 **Figure 1 - Figure Supplement 1B.** Quantification values of each peptide-spectrum match were exported
685 into Excel, and the mean peptide abundance ratios were calculated from the abundance ratios of all
686 manually verified peptide-spectrum matches assigning to the phosphorylation site(s) of interest. Label-free
687 quantitative analysis of the areas of extracted MS1 chromatograms of phosphorylated and non-
688 phosphorylated peptide ions covering the phosphorylation site(s) of interest was used to evaluate the
689 proportion of phosphorylated to non-phosphorylated peptides at each position, as well as the relative
690 abundances of phosphopeptides.

691

692 Plasmids

693 The Nav1.5 phosphomutant constructs were generated by mutating the serine(s)/threonine(s) to
694 alanine(s) (A) or glutamate(s) (E) by site-directed mutagenesis of a pCI-Nav1.5 plasmid containing the
695 human Nav1.5 hH1C cDNA (30) (NCBI Reference Sequence NM_000335) using the QuikChange II XL
696 Site-Directed Mutagenesis kit (Agilent, Sant Clara, CA) or the Q5 Site-Directed Mutagenesis kit (New
697 England Biolabs, Ipswich, MA). The mutated constructs were then digested with restriction
698 endonucleases to excise the mutated fragments, which were then subcloned into the original pCI-Nav1.5
699 plasmid. The human Nav β 1 (NM_001037, a gift from A. L. George) cDNAs was subcloned into
700 pRc/CMV. All constructs were sequenced to ensure that no unintentional mutations were introduced.

701

702 Culture and transient transfections

703 Human Embryonic Kidney 293 (HEK-293) cells were maintained in Dulbecco's Modified
704 Eagle's Medium (DMEM, Thermo Fisher Scientific), supplemented with 10% fetal bovine serum, 100
705 U/ml penicillin and 100 μ g/ml streptomycin, in 37°C, 5% CO₂: 95% air incubator. Cells were transiently
706 transfected at 70-80% confluence in 35 mm dishes with 0.6 μ g of the WT or phosphomutant Nav1.5
707 plasmid and 1.2 μ g of the Nav β 1 plasmid using 2 μ L of Lipofectamine 2000 (Thermo Fisher Scientific)

Proteomic and functional mapping of cardiac Nav1.5 channel phosphorylation

708 following the manufacturer's instructions. For whole-cell recordings, transfections also contained 0.2 μ g
709 of the pEGFP plasmid (Enhanced Green Fluorescent Protein plasmid, Clontech), and EGFP expression
710 served as a marker of transfection. The absolute amounts of the various constructs were calculated and the
711 empty pcDNA3.1 plasmid was used as a filler plasmid to keep the total DNA constant at 2 μ g in each
712 transfection.

713

714 **Electrophysiological recordings**

715 Whole-cell Nav currents were recorded at room temperature from transiently transfected HEK-
716 293 cells using an Axopatch 200A amplifier (Axon Instruments, Molecular Devices, San Jose, CA) 48
717 hours after transfection. Voltage-clamp protocols were applied using the pClamp 10.2 software package
718 (Axon Instruments) interfaced to the electrophysiological equipment using a Digidata 1440A digitizer
719 (Axon Instruments). Current signals were filtered at 10 kHz prior to digitization at 50 kHz and storage.
720 Patch-clamp pipettes were fabricated from borosilicate glass (OD: 1.5 mm, ID: 0.86 mm, Sutter
721 Instrument, Novato, CA) using a P-97 micropipette puller (Sutter Instrument), coated with wax, and fire-
722 polished to a resistance between 1.5 and 2.5 M Ω when filled with internal solution. The internal solution
723 contained (in mM): NaCl 5, CsF 115, CsCl 20, HEPES 10, EGTA 10 (pH 7.35 with CsOH, ~300 mosM).
724 The external solution contained (in mM): NaCl 10 (NaCl 20 for analysis of single phosphomutants), CsCl
725 103, TEA-Cl (tetraethylammonium chloride) 25, HEPES 10, Glucose 5, CaCl₂ 1, MgCl₂ 2 (pH 7.4 with
726 CsOH, ~300 mosM). All chemicals were purchased from Sigma. After establishing the whole-cell
727 configuration, three minutes were allowed to ensure stabilization of voltage-dependence of activation and
728 inactivation properties, at which time 25 ms voltage steps to \pm 10 mV from a holding potential (HP) of -
729 70 mV were applied to allow measurement of whole-cell membrane capacitances, input and series
730 resistances. Only cells with access resistance < 7 M Ω were used, and input resistances were typically > 5
731 G Ω . After compensation of series resistance (80%), the membrane was held at a HP of -120 mV, and the
732 voltage-clamp protocols were carried out as indicated below. Leak currents were always < 200 pA at HP
733 (-120 mV), and were corrected offline. Cells exhibiting peak current amplitudes < 500 or > 5000 pA were
734 excluded from analyses of biophysical properties because of leak or voltage-clamp issues, respectively,
735 but conserved in analyses of peak current density to avoid bias in evaluation of current densities.

736 Data were compiled and analyzed using ClampFit 10.2 (Axon Instruments), Microsoft Excel, and
737 Prism (GraphPad Software, San Diego, CA). Whole-cell membrane capacitances (C_m) were determined
738 by analyzing the decays of capacitive transients elicited by brief (25 ms) voltage steps to \pm 10 mV from
739 the HP (-70 mV). Input resistances were calculated from the steady-state currents elicited by the same
740 \pm 10 mV steps (from the HP). Series resistances were calculated by dividing the decay time constants of
741 the capacitive transients (fitted with single exponentials) by the C_m. To determine peak Na⁺ current-
742 voltage relationships, currents were elicited by 50-ms depolarizing pulses to potentials ranging from -80
743 to +40 mV (presented at 5-s intervals in 5-mV increments) from a HP of -120 mV. Peak current
744 amplitudes were defined as the maximal currents evoked at each voltage. Current amplitudes were leak-
745 corrected, normalized to the C_m, and current densities are presented.

746 To analyze voltage-dependence of current activation properties, conductances (G) were
747 calculated, and conductance-voltage relationships were fitted with the Boltzmann equation $G = G_{\max} / (1 +$
748 $\exp(-(V_m - V_{1/2}) / k))$, in which $V_{1/2}$ is the membrane potential of half-activation and k is the slope factor.
749 The time courses of inactivation of macroscopic currents were fitted with bi-exponential functions, $I(t) =$
750 $A_{\text{fast}} \times \exp(-t/\tau_{\text{fast}}) + A_{\text{slow}} \times \exp(-t/\tau_{\text{slow}}) + A_0$, in which A_{fast} and A_{slow} are the amplitudes of the fast and
751 slow inactivating current components, respectively, and τ_{fast} and τ_{slow} are the decay time constants of A_{fast}
752 and A_{slow} , respectively. A standard two-pulse protocol was used to examine the voltage-dependences of
753 steady-state inactivation. From a HP of -120 mV, 1-s conditioning pulses to potentials ranging from -120
754 to -45 mV (in 5-mV increments) were followed by 20-ms test depolarizations to -20 mV (interpulse
755 intervals were 5-s). Current amplitudes evoked from each conditioning voltage were measured and
756 normalized to the maximal current (I_{\max}) evoked from -120 mV, and normalized currents were plotted as a
757 function of the conditioning voltage. The resulting steady-state inactivation curves were fitted with the
758 Boltzmann equation $I = I_{\max} / (1 + \exp((V_m - V_{1/2}) / k))$, in which $V_{1/2}$ is the membrane potential of half-

Proteomic and functional mapping of cardiac Nav1.5 channel phosphorylation

759 inactivation and k is the slope factor. To examine the rates of recovery from inactivation, a three-pulse
760 protocol was used. Cells were first depolarized to -20 mV (from a HP of -120 mV) to inactivate the
761 channels, and subsequently repolarized to -120 mV for varying times (ranging from 1 to 200 ms),
762 followed by test depolarizations to -20 mV to assess the extent of recovery (interpulse intervals were 5-s).
763 The current amplitudes at -20 mV, measured following each recovery period, were normalized to the
764 maximal current amplitude and plotted as function of the recovery time. The resulting plot was fitted with
765 a single exponential function $I(t) = A \times (1 - \exp(-t / \tau_{\text{rec}}))$ to determine the recovery time constant. For
766 each of these biophysical properties, data from individual cells were first fitted and then averaged.

767 The currents generated on expression of each phosphosilent and phosphomimetic Nav1.5 mutant
768 were recorded and compared to currents generated by the Nav1.5-WT construct obtained on the same
769 days of patch-clamp analyses. The densities and properties of Nav1.5-WT currents in each data set were
770 similar, and for the sake of clarity, a single representative Nav1.5-WT channel data set was chosen and
771 presented in **Figure 3 - Figure Supplement 2 and Table Supplement 1 and Figure 4 - Table**
772 **Supplement 1**.

773 In experiments aimed at recording the tetrodotoxin (TTX)-sensitive late Na⁺ current, cells were
774 bathed in external solution containing (in mM): NaCl 120, TEA-Cl 25, HEPES 10, Glucose 5, CaCl₂ 1,
775 MgCl₂ 2 (pH 7.4 with CsOH, ~300 mosM). Repetitive 350-ms test pulses to -20 mV from a HP of -120
776 mV (at 5-s intervals) were applied to cells to record Na⁺ currents in the absence of TTX. Cells were then
777 superfused locally with the external solution supplemented with 30 μM TTX (Bio-Techne SAS, Rennes,
778 France). Only cells exhibiting peak current amplitudes > 4000 pA were used (those with peak currents <
779 4000 pA did not show measurable late Na⁺ current), and cells with difference in leak current amplitudes
780 before and after TTX application > 5 pA at -20 mV (calculated from leak currents at -120 mV) were
781 excluded from analyses. TTX-sensitive currents from individual cells were determined by offline digital
782 subtraction of average leak-subtracted currents obtained from 5 recordings in the absence and in the
783 presence of TTX after achieving steady state. The amplitude of TTX-sensitive late Na⁺ current was
784 defined as the steady-state current amplitude (A_0) obtained by fitting the inactivation decay of
785 macroscopic TTX-sensitive current with the double exponential function $I(t) = A_{\text{fast}} \times \exp(-t/\tau_{\text{fast}}) + A_{\text{slow}} \times$
786 $\exp(-t/\tau_{\text{slow}}) + A_0$. For each cell, the TTX-sensitive late Na⁺ current amplitude was normalized to the peak
787 Na⁺ current amplitude, and expressed as a percentage of the peak Na⁺ current.

788

789 Cell surface biotinylation and western blot analyses

790 Surface biotinylation of HEK-293 cells was completed as described previously (51). Briefly, cells
791 were incubated with the cleavable EZ-Link Sulfo-NHS-SS-Biotin (0.5 mg/ml, Thermo Fisher Scientific)
792 in ice-cold PBS (pH 7.4) for 30 min at 4°C. Free biotin was quenched with Tris-saline (10 mM Tris (pH
793 7.4), 120 mM NaCl), and detergent-soluble cell lysates were prepared. Biotinylated cell surface proteins
794 were affinity-purified using NeutrAvidin-conjugated agarose beads (Thermo Fisher Scientific), and
795 purified cell surface proteins were analyzed by western blot using the mαNavPAN antibody (1:2000,
796 Sigma, #S8809), the anti-transferrin receptor mouse monoclonal antibody (TransR, 1:1000, Thermo
797 Fisher Scientific), and the anti-glyceraldehyde 3-phosphate dehydrogenase mouse monoclonal antibody
798 (GAPDH, 1:100000, Santa Cruz Biotechnology). Bound primary antibodies were detected using
799 horseradish peroxidase-conjugated goat anti-mouse secondary antibodies (Cell Signaling Technology,
800 Inc., Danvers, MA), and protein signals were visualized using the SuperSignal West Dura Extended
801 Duration Substrate (Thermo Fisher Scientific). Bands corresponding to Nav1.5 were normalized to bands
802 corresponding to TransR from the same sample. Nav1.5 phosphomutant protein expression (total or cell
803 surface) is expressed relative to Nav1.5-WT protein expression (total or cell surface).

804

805 Molecular simulations

806 Molecular simulations were performed with the CAMPARI software package (35), using the
807 ABSINTH implicit solvation model (52) and parameters from the OPLS-AA forcefield. Markov Chain
808 Metropolis Monte Carlo moves sampled the conformational space of each protein segment. To mimic a 5

Proteomic and functional mapping of cardiac Nav1.5 channel phosphorylation

809 mM NaCl concentration, neutralizing and excess Na⁺ and Cl⁻ ions were modeled explicitly with the
810 protein segments in spherical droplets of (5 x number of residues) Å radius. Ten simulation runs were
811 performed for each sequence construct, and the average of these ten runs was then plotted. The
812 simulations denoted as EV (Excluded Volume) and FRC (Flory Random Coil) are reference models. In
813 the EV limit, the only interactions considered are the pairwise repulsions. In the FRC limit, conformations
814 are constructed by randomly sampling residue-specific backbone dihedral angles. Three EV and three
815 FRC simulation runs were performed for each protein segment, and the averages were plotted.

816

817 **Statistical analyses**

818 Results are expressed as means ± SEM. Data were first tested for normality using the D'Agostino
819 and Pearson normality test. Depending on the results of normality tests, statistical analyses were then
820 performed using the Mann-Whitney nonparametric test, the Kruskal-Wallis one-way ANOVA followed
821 by the Dunn's post-hoc test, or the one-way ANOVA followed by the Dunnett's post-hoc test, as
822 indicated in Figures and Tables. All these analyses, as well as plots and graphs were performed using
823 Prism (GraphPad Software).

824

825

826

827

828

829

830

831

832

833

834

835

836

837

838

839

840

841

842

843

844

845

846

847

848

849

850

851

852

853

854

855

856

857

858

859

Proteomic and functional mapping of cardiac Nav1.5 channel phosphorylation

860 **Acknowledgements:** This work was supported by the *Agence Nationale de la Recherche* [ANR-15-
861 CE14-0006-01 and ANR-16-CE92-0013-01 to CM], the Deutsche Forschungsgemeinschaft (DFG) [Ma
862 1982/5-1 to LSM], and the National Institutes of Health [R01-HL148803 to CM, RVP and JRS; R01-
863 HL034161 and R01-HL142520 to JMN; and 5R01NS056114 to RVP]. The mass spectrometric
864 experiments were performed at the Washington University Proteomics Shared Resource (WU-PSR). The
865 WU-PSR is supported in part by the WU Institute of Clinical and Translational Sciences (NCATS UL1
866 TR000448), the Mass Spectrometry Research Resource (NIGMS P41 GM103422) and the Siteman
867 Comprehensive Cancer Center Support Grant (NCI P30 CA091842). ML was supported by a *Groupe de*
868 *Réflexion sur la Recherche Cardiovasculaire-Société Française de Cardiologie* predoctoral fellowship
869 [SFC/GRRC2018]. SB was supported by a Lefoulon-Delalande postdoctoral fellowship. The expert
870 technical assistance of Petra Erdmann-Gilmore, Yiling Mi and Rose Connors is gratefully acknowledged.
871 The content of the research reported is solely the responsibility of the authors and does not necessarily
872 represent the official view of the funding agencies.

873
874 **Competing Interests:** The authors declare that they have no conflicts of interest with the contents of this
875 article.

876
877 **Author Contributions:** CM designed the study and wrote the paper. CM, DM, JMN, RRT and LSM
878 designed, performed and/or analyzed the mass spectrometry experiments. ML, SB, AL, CC, PMC, BE,
879 JMN and CM designed, performed and/or analyzed the functional analyses. EW, KMR, RVP and JRS
880 designed, performed and/or analyzed the modeling analyses. SW and LSM provided the Sham/TAC mice
881 and performed mouse echocardiography. All authors reviewed the results and approved the final version
882 of the manuscript.

883
884
885
886
887
888
889
890
891
892
893
894
895
896
897
898
899
900
901
902
903
904
905
906
907
908

Proteomic and functional mapping of cardiac Nav1.5 channel phosphorylation

909 **References**

- 910
- 911 1. Remme, C. A., and Bezzina, C. R. (2010) Sodium channel (dys)function and cardiac arrhythmias.
- 912 *Cardiovasc Ther* **28**, 287-294
- 913 2. Marionneau, C., and Abriel, H. (2015) Regulation of the cardiac Na channel Na1.5 by post-
- 914 translational modifications. *J Mol Cell Cardiol* **82**, 36-47
- 915 3. Pei, Z., Xiao, Y., Meng, J., Hudmon, A., and Cummins, T. R. (2016) Cardiac sodium channel
- 916 palmitoylation regulates channel availability and myocyte excitability with implications for
- 917 arrhythmia generation. *Nat Commun* **7**, 12035
- 918 4. Plant, L. D., Xiong, D., Romero, J., Dai, H., and Goldstein, S. A. N. (2020) Hypoxia Produces Pro-
- 919 arrhythmic Late Sodium Current in Cardiac Myocytes by SUMOylation of Nav1.5 Channels. *Cell*
- 920 *Rep* **30**, 2225-2236 e2224
- 921 5. Yu, P., Hu, L., Xie, J., Chen, S., Huang, L., Xu, Z., Liu, X., Zhou, Q., Yuan, P., Yan, X., Jin, J.,
- 922 Shen, Y., Zhu, W., Fu, L., Chen, Q., Yu, J., Hu, J., Cao, Q., Wan, R., and Hong, K. (2018) O-
- 923 GlcNAcylation of cardiac Nav1.5 contributes to the development of arrhythmias in diabetic hearts.
- 924 *Int J Cardiol* **260**, 74-81
- 925 6. Schubert, B., VanDongen, A. M., Kirsch, G. E., and Brown, A. M. (1989) Beta-adrenergic
- 926 inhibition of cardiac sodium channels by dual G-protein pathways. *Science* **245**, 516-519
- 927 7. Burel, S., Coyan, F. C., Lorenzini, M., Meyer, M. R., Lichti, C. F., Brown, J. H., Loussouarn, G.,
- 928 Charpentier, F., Nerbonne, J. M., Townsend, R. R., Maier, L. S., and Marionneau, C. (2017) C-
- 929 terminal phosphorylation of Nav1.5 impairs FGF13-dependent regulation of channel inactivation.
- 930 *J Biol Chem* **292**, 17431-17448
- 931 8. Marionneau, C., Lichti, C. F., Lindenbaum, P., Charpentier, F., Nerbonne, J. M., Townsend, R. R.,
- 932 and Merot, J. (2012) Mass Spectrometry-Based Identification of Native Cardiac Nav1.5 Channel
- 933 alpha Subunit Phosphorylation Sites. *J Proteome Res* **11**, 5994-6007
- 934 9. Herren, A. W., Weber, D. M., Rigor, R. R., Margulies, K. B., Phinney, B. S., and Bers, D. M.
- 935 (2015) CaMKII Phosphorylation of Na(V)1.5: Novel in Vitro Sites Identified by Mass
- 936 Spectrometry and Reduced S516 Phosphorylation in Human Heart Failure. *J Proteome Res* **14**,
- 937 2298-2311
- 938 10. Aiba, T., Barth, A. S., Hesketh, G. G., Hashambhoy, Y. L., Chakir, K., Tunin, R. S., Greenstein, J.
- 939 L., Winslow, R. L., Kass, D. A., and Tomaselli, G. F. (2013) Cardiac resynchronization therapy
- 940 improves altered Na channel gating in canine model of dyssynchronous heart failure. *Circ*
- 941 *Arrhythm Electrophysiol* **6**, 546-554
- 942 11. Glynn, P., Musa, H., Wu, X., Unudurthi, S. D., Little, S., Qian, L., Wright, P. J., Radwanski, P. B.,
- 943 Gyorke, S., Mohler, P. J., and Hund, T. J. (2015) Voltage-Gated Sodium Channel Phosphorylation
- 944 at Ser571 Regulates Late Current, Arrhythmia, and Cardiac Function In Vivo. *Circulation* **132**,
- 945 567-577
- 946 12. Koval, O. M., Snyder, J. S., Wolf, R. M., Pavlovicz, R. E., Glynn, P., Curran, J., Leymaster, N. D.,
- 947 Dun, W., Wright, P. J., Cardona, N., Qian, L., Mitchell, C. C., Boyden, P. A., Binkley, P. F., Li,
- 948 C., Anderson, M. E., Mohler, P. J., and Hund, T. J. (2012) Ca²⁺/Calmodulin-Dependent Protein
- 949 Kinase II-Based Regulation of Voltage-Gated Na⁺ Channel in Cardiac Disease. *Circulation* **126**,
- 950 2084-2094
- 951 13. Maltsev, V. A., Reznikov, V., Undrovinas, N. A., Sabbah, H. N., and Undrovinas, A. (2008)
- 952 Modulation of late sodium current by Ca²⁺, calmodulin, and CaMKII in normal and failing dog
- 953 cardiomyocytes: similarities and differences. *Am J Physiol Heart Circ Physiol* **294**, H1597-1608
- 954 14. Toischer, K., Hartmann, N., Wagner, S., Fischer, T. H., Herting, J., Danner, B. C., Sag, C. M.,
- 955 Hund, T. J., Mohler, P. J., Belardinelli, L., Hasenfuss, G., Maier, L. S., and Sossalla, S. (2013) Role
- 956 of late sodium current as a potential arrhythmogenic mechanism in the progression of pressure-
- 957 induced heart disease. *J Mol Cell Cardiol* **61**, 111-122

Proteomic and functional mapping of cardiac Nav1.5 channel phosphorylation

- 958 15. Wagner, S., Dybkova, N., Rasenack, E. C., Jacobshagen, C., Fabritz, L., Kirchhof, P., Maier, S. K.,
959 Zhang, T., Hasenfuss, G., Brown, J. H., Bers, D. M., and Maier, L. S. (2006) Ca²⁺/calmodulin-
960 dependent protein kinase II regulates cardiac Na⁺ channels. *J Clin Invest* **116**, 3127-3138
- 961 16. Maltsev, V. A., Silverman, N., Sabbah, H. N., and Undrovinas, A. I. (2007) Chronic heart failure
962 slows late sodium current in human and canine ventricular myocytes: implications for
963 repolarization variability. *Eur J Heart Fail* **9**, 219-227
- 964 17. Valdivia, C. R., Chu, W. W., Pu, J., Foell, J. D., Haworth, R. A., Wolff, M. R., Kamp, T. J., and
965 Makielski, J. C. (2005) Increased late sodium current in myocytes from a canine heart failure model
966 and from failing human heart. *J Mol Cell Cardiol* **38**, 475-483
- 967 18. Xi, Y., Wu, G., Yang, L., Han, K., Du, Y., Wang, T., Lei, X., Bai, X., and Ma, A. (2009) Increased
968 late sodium currents are related to transcription of neuronal isoforms in a pressure-overload model.
969 *Eur J Heart Fail* **11**, 749-757
- 970 19. Zicha, S., Maltsev, V. A., Nattel, S., Sabbah, H. N., and Undrovinas, A. I. (2004) Post-
971 transcriptional alterations in the expression of cardiac Na⁺ channel subunits in chronic heart failure.
972 *J Mol Cell Cardiol* **37**, 91-100
- 973 20. Ashpole, N. M., Herren, A. W., Ginsburg, K. S., Brogan, J. D., Johnson, D. E., Cummins, T. R.,
974 Bers, D. M., and Hudmon, A. (2012) Ca²⁺/Calmodulin-dependent Protein Kinase II (CaMKII)
975 Regulates Cardiac Sodium Channel Nav1.5 Gating by Multiple Phosphorylation Sites. *J Biol Chem*
976 **287**, 19856-19869
- 977 21. Hund, T. J., Koval, O. M., Li, J., Wright, P. J., Qian, L., Snyder, J. S., Gudmundsson, H., Kline, C.
978 F., Davidson, N. P., Cardona, N., Rasband, M. N., Anderson, M. E., and Mohler, P. J. (2010) A
979 beta(IV)-spectrin/CaMKII signaling complex is essential for membrane excitability in mice. *J Clin*
980 *Invest* **120**, 3508-3519
- 981 22. Mishra, S., Reznikov, V., Maltsev, V. A., Undrovinas, N. A., Sabbah, H. N., and Undrovinas, A.
982 (2014) Contribution of sodium channel neuronal isoform Nav1.1 to late sodium current in
983 ventricular myocytes from failing hearts. *J Physiol*
- 984 23. Dybkova, N., Ahmad, S., Pabel, S., Tirilomis, P., Hartmann, N., Fischer, T. H., Bengel, P.,
985 Tirilomis, T., Ljubojevic, S., Renner, A., Gummert, J., Ellenberger, D., Wagner, S., Frey, N., Maier,
986 L. S., Streckfuss-Bomeke, K., Hasenfuss, G., and Sossalla, S. (2018) Differential regulation of
987 sodium channels as a novel proarrhythmic mechanism in the human failing heart. *Cardiovasc Res*
988 **114**, 1728-1737
- 989 24. Kaab, S., Dixon, J., Duc, J., Ashen, D., Nabauer, M., Beuckelmann, D. J., Steinbeck, G.,
990 McKinnon, D., and Tomaselli, G. F. (1998) Molecular basis of transient outward potassium current
991 downregulation in human heart failure: a decrease in Kv4.3 mRNA correlates with a reduction in
992 current density. *Circulation* **98**, 1383-1393
- 993 25. Noyes, A. M., Zhou, A., Gao, G., Gu, L., Day, S., Andrew Wasserstrom, J., and Dudley, S. C.
994 (2017) Abnormal sodium channel mRNA splicing in hypertrophic cardiomyopathy. *Int J Cardiol*
995 **249**, 282-286
- 996 26. Shang, L. L., Pfahnl, A. E., Sanyal, S., Jiao, Z., Allen, J., Banach, K., Fahrenbach, J., Weiss, D.,
997 Taylor, W. R., Zafari, A. M., and Dudley, S. C., Jr. (2007) Human heart failure is associated with
998 abnormal C-terminal splicing variants in the cardiac sodium channel. *Circ Res* **101**, 1146-1154
- 999 27. Liu, M., Gu, L., Sulkin, M. S., Liu, H., Jeong, E. M., Greener, I., Xie, A., Efimov, I. R., and Dudley,
1000 S. C., Jr. (2013) Mitochondrial dysfunction causing cardiac sodium channel downregulation in
1001 cardiomyopathy. *J Mol Cell Cardiol* **54**, 25-34
- 1002 28. Luo, L., Ning, F., Du, Y., Song, B., Yang, D., Salvage, S. C., Wang, Y., Fraser, J. A., Zhang, S.,
1003 Ma, A., and Wang, T. (2017) Calcium-dependent Nedd4-2 upregulation mediates degradation of
1004 the cardiac sodium channel Nav1.5: implications for heart failure. *Acta Physiol (Oxf)* **221**, 44-58
- 1005 29. Rivaud, M. R., Agullo-Pascual, E., Lin, X., Leo-Macias, A., Zhang, M., Rothenberg, E., Bezzina,
1006 C. R., Delmar, M., and Remme, C. A. (2017) Sodium Channel Remodeling in Subcellular
1007 Microdomains of Murine Failing Cardiomyocytes. *J Am Heart Assoc* **6**

Proteomic and functional mapping of cardiac Nav1.5 channel phosphorylation

- 1008 30. Makielski, J. C., Ye, B., Valdivia, C. R., Pagel, M. D., Pu, J., Tester, D. J., and Ackerman, M. J.
1009 (2003) A ubiquitous splice variant and a common polymorphism affect heterologous expression of
1010 recombinant human SCN5A heart sodium channels. *Circ Res* **93**, 821-828
- 1011 31. Iakoucheva, L. M., Radivojac, P., Brown, C. J., O'Connor, T. R., Sikes, J. G., Obradovic, Z., and
1012 Dunker, A. K. (2004) The importance of intrinsic disorder for protein phosphorylation. *Nucleic
1013 Acids Res* **32**, 1037-1049
- 1014 32. Wright, P. E., and Dyson, H. J. (2015) Intrinsically disordered proteins in cellular signalling and
1015 regulation. *Nat Rev Mol Cell Biol* **16**, 18-29
- 1016 33. Das, R. K., and Pappu, R. V. (2013) Conformations of intrinsically disordered proteins are
1017 influenced by linear sequence distributions of oppositely charged residues. *Proc Natl Acad Sci U S
1018 A* **110**, 13392-13397
- 1019 34. Mao, A. H., Crick, S. L., Vitalis, A., Chicoine, C. L., and Pappu, R. V. (2010) Net charge per
1020 residue modulates conformational ensembles of intrinsically disordered proteins. *Proc Natl Acad
1021 Sci U S A* **107**, 8183-8188
- 1022 35. Vitalis, A., and Pappu, R. V. (2009) Methods for Monte Carlo simulations of biomacromolecules.
1023 *Annu Rep Comput Chem* **5**, 49-76
- 1024 36. Martin, E. W., Holehouse, A. S., Grace, C. R., Hughes, A., Pappu, R. V., and Mittag, T. (2016)
1025 Sequence Determinants of the Conformational Properties of an Intrinsically Disordered Protein
1026 Prior to and upon Multisite Phosphorylation. *J Am Chem Soc* **138**, 15323-15335
- 1027 37. Holehouse, A. S., and Pappu, R. V. (2018) Collapse Transitions of Proteins and the Interplay
1028 Among Backbone, Sidechain, and Solvent Interactions. *Annu Rev Biophys*
- 1029 38. Liu, X., Chen, Z., Han, Z., Liu, Y., Wu, X., Peng, Y., Di, W., Lan, R., Sun, B., Xu, B., and Xu, W.
1030 (2019) AMPK-mediated degradation of Nav1.5 through autophagy. *FASEB J* **33**, 5366-5376
- 1031 39. Ahern, C. A., Zhang, J. F., Wookalis, M. J., and Horn, R. (2005) Modulation of the cardiac sodium
1032 channel Nav1.5 by Fyn, a Src family tyrosine kinase. *Circ Res* **96**, 991-998
- 1033 40. Iqbal, S. M., Aufy, M., Shabbir, W., and Lemmens-Gruber, R. (2018) Identification of
1034 phosphorylation sites and binding pockets for modulation of Nav 1.5 channel by Fyn tyrosine
1035 kinase. *FEBS J* **285**, 2520-2530
- 1036 41. Hunter, T. (2012) Why nature chose phosphate to modify proteins. *Philos Trans R Soc Lond B Biol
1037 Sci* **367**, 2513-2516
- 1038 42. Boehmer, C., Wilhelm, V., Palmada, M., Wallisch, S., Henke, G., Brinkmeier, H., Cohen, P.,
1039 Pieske, B., and Lang, F. (2003) Serum and glucocorticoid inducible kinases in the regulation of the
1040 cardiac sodium channel SCN5A. *Cardiovasc Res* **57**, 1079-1084
- 1041 43. Varga, Z., Zhu, W., Schubert, A. R., Pardieck, J. L., Krumholz, A., Hsu, E. J., Zaydman, M. A.,
1042 Cui, J., and Silva, J. R. (2015) Direct Measurement of Cardiac Na⁺ Channel Conformations
1043 Reveals Molecular Pathologies of Inherited Mutations. *Circ Arrhythm Electrophysiol* **8**, 1228-1239
- 1044 44. Gao, S., Ho, D., Vatner, D. E., and Vatner, S. F. (2011) Echocardiography in Mice. *Curr Protoc
1045 Mouse Biol* **1**, 71-83
- 1046 45. Vassilev, P. M., Scheuer, T., and Catterall, W. A. (1988) Identification of an intracellular peptide
1047 segment involved in sodium channel inactivation. *Science* **241**, 1658-1661
- 1048 46. Schneider, C., Newman, R. A., Sutherland, D. R., Asser, U., and Greaves, M. F. (1982) A one-step
1049 purification of membrane proteins using a high efficiency immunomatrix. *J Biol Chem* **257**, 10766-
1050 10769
- 1051 47. Erde, J., Loo, R. R., and Loo, J. A. (2014) Enhanced FASP (eFASP) to increase proteome coverage
1052 and sample recovery for quantitative proteomic experiments. *J Proteome Res* **13**, 1885-1895
- 1053 48. Wisniewski, J. R., Zougman, A., Nagaraj, N., and Mann, M. (2009) Universal sample preparation
1054 method for proteome analysis. *Nat Methods* **6**, 359-362
- 1055 49. Chen, Z. W., Fuchs, K., Sieghart, W., Townsend, R. R., and Evers, A. S. (2012) Deep amino acid
1056 sequencing of native brain GABAA receptors using high-resolution mass spectrometry. *Mol Cell
1057 Proteomics* **11**, M111 011445

Proteomic and functional mapping of cardiac Nav1.5 channel phosphorylation

- 1058 50. Zhang, J., Xin, L., Shan, B., Chen, W., Xie, M., Yuen, D., Zhang, W., Zhang, Z., Lajoie, G. A., and
1059 Ma, B. (2012) PEAKS DB: de novo sequencing assisted database search for sensitive and accurate
1060 peptide identification. *Mol Cell Proteomics* **11**, M111 010587
- 1061 51. Marionneau, C., Carrasquillo, Y., Norris, A. J., Townsend, R. R., Isom, L. L., Link, A. J., and
1062 Nerbonne, J. M. (2012) The sodium channel accessory subunit Navbeta1 regulates neuronal
1063 excitability through modulation of repolarizing voltage-gated K(+) channels. *J Neurosci* **32**, 5716-
1064 5727
- 1065 52. Vitalis, A., and Pappu, R. V. (2009) ABSINTH: a new continuum solvation model for simulations
1066 of polypeptides in aqueous solutions. *J Comput Chem* **30**, 673-699
- 1067
1068
1069
1070
1071
1072
1073
1074
1075
1076
1077
1078
1079
1080
1081
1082
1083
1084
1085
1086
1087
1088
1089
1090
1091
1092
1093
1094
1095
1096
1097
1098
1099
1100
1101
1102
1103
1104
1105
1106
1107
1108

Proteomic and functional mapping of cardiac Nav1.5 channel phosphorylation

1109 **Figure Legends**

1110
1111 **Figure 1.** Localization and quantification of 42 MS-identified Nav1.5 phosphorylation sites in
1112 m α NavPAN-IPs from Sham and TAC mouse left ventricles. (A) Schematic representation of
1113 phosphorylation sites on the Nav1.5 protein (UniProt reference sequence K3W4N7). Two
1114 phosphorylation site locations are possible at amino acids S1056-T1058. (B) The areas of extracted MS1
1115 ion chromatograms, corresponding to MS2 spectra assigning phosphorylated (in red) and non-
1116 phosphorylated (in white) Nav1.5 peptides at indicated phosphorylation site(s), in m α NavPAN-IPs from
1117 Sham and TAC left ventricles are indicated. (C) Distributions and mean \pm SEM relative abundances of
1118 individual Nav1.5 phosphopeptides allowing assignments of indicated phosphorylation site(s), in TAC
1119 LV (n=5, in black), *versus* Sham LV (n=4, in white), m α NavPAN-IPs, were obtained using TMT reporter
1120 ion intensities. The relative abundances of Nav1.5 phosphopeptides exhibiting phosphorylation(s) on
1121 serine-671 (S671, n=12 peptides) alone, or in combination with serines-664 (S664 + S671, n=9 peptides)
1122 or -667 (S667 + S671, n=7 peptides) are increased (** p <0.01, *** p <0.001, Mann-Whitney test) in TAC
1123 LV, *versus* Sham LV, m α NavPAN-IPs.

1124
1125 **Figure 1 - Figure Supplement 1.** Immunoprecipitation yields and relative quantification of Nav1.5
1126 peptide abundances from Sham and TAC mouse left ventricles. (A) Representative western blots of total
1127 lysates and m α NavPAN-IPs from Sham and TAC left ventricles probed with the anti-Nav1.5 rabbit
1128 polyclonal (Rb α Nav1.5) and anti-GAPDH mouse monoclonal antibodies. (B) Normalization factors used
1129 in MS1 and MS2 analyses to correct for technical variabilities in Nav1.5 protein abundance in
1130 m α NavPAN-IPs from Sham and TAC left ventricles. (C) Distribution of TAC/Sham log₂ normalized
1131 ratios of Nav1.5 peptide-spectrum matches. Both biochemical (A) and mass spectrometry (B, C) analyses
1132 of Nav1.5 immunoprecipitation yields and peptide relative abundance demonstrate low technical
1133 variability.

1134
1135 **Figure 1 - Figure Supplement 2.** Relative abundances of phosphorylated Nav1.5 peptides at indicated
1136 phosphorylation site(s) in m α NavPAN-IPs from Sham and TAC mouse left ventricles. Values correspond
1137 to the areas of extracted MS1 ion chromatograms corresponding to MS2 spectra assigning phosphorylated
1138 peptides at indicated phosphorylation site(s). The brackets indicate the subgroups of phosphorylation sites
1139 analyzed in **Figure 1B**. Independent quantification of S459 and S460 phosphorylated peptides was not
1140 possible because localization of the phosphorylation site in most of the phosphorylated peptides could not
1141 be discriminated.

1142
1143 **Figure 2.** Nav1.5 amino acid sequence coverage and localization of 42 Nav1.5 phosphorylation sites in
1144 m α NavPAN-IPs from Sham and TAC mouse left ventricles. Covered sequence and MS-identified
1145 phosphorylation sites are highlighted in yellow and red, respectively; transmembrane segments (S1-S6) in
1146 each domain (I-IV) are in bold and underlined in black; and loops I, II and III correspond to interdomains
1147 I-II, II-III and III-IV, respectively. Two peptides differing by the presence or absence of a glutamine (Q)
1148 at position-1080 were detected, reflecting the expression of two Nav1.5 variants (the Q1080 variant
1149 corresponds to UniProt reference sequence K3W4N7; and the Q1080del variant corresponds to Q9JJV9).
1150 Two phosphorylation site locations are possible at amino acids S1056-T1058 (in green).

1151
1152 **Figure 3.** Phosphorylation at positions S664-671 regulates the voltage-dependence of current activation
1153 and peak Na⁺ current density. (A) Representative whole-cell voltage-gated Na⁺ currents recorded forty-
1154 eight hours following transfection of HEK-293 cells with Nav1.5-WT + Nav β 1 (black), Nav1.5-S664-
1155 671A + Nav β 1 (blue) or Nav1.5-S664-671E + Nav β 1 (red) using the protocols illustrated in each panel.
1156 Scale bars are 1 nA and 2 ms. (B) Voltage-dependences of current activation and steady-state
1157 inactivation. The voltage-dependence of current activation is shifted towards depolarized potentials in
1158 cells expressing the Nav1.5-S664-671A or Nav1.5-S664-671E mutants, compared to cells expressing

Proteomic and functional mapping of cardiac Nav1.5 channel phosphorylation

1159 Nav_v1.5-WT. (C) Mean \pm SEM peak Na⁺ current (I_{Na}) densities plotted as a function of test potential. The
1160 peak I_{Na} density is reduced in cells expressing the Nav_v1.5-S664-671E mutant, compared to cells
1161 expressing Nav_v1.5-WT. Mean \pm SEM times to peak (D), and fast (τ_{fast} , E) and slow (τ_{slow} , F) inactivation
1162 time constants plotted as a function of test potential. The time to peak, τ_{fast} and τ_{slow} are higher in cells
1163 expressing the Nav_v1.5-S664-671A or Nav_v1.5-S664-671E mutants, compared to cells expressing Nav_v1.5-
1164 WT. Current densities, time- and voltage-dependent properties, as well as statistical comparisons across
1165 groups, are provided in **Figure 3 - Figure Supplement 2 & Table Supplement 1**.

1167 **Figure 3 - Figure Supplement 1.** Conservation of phosphorylation sites in mouse and human Nav_v1.5.
1168 The mouse (Reference sequence NP_001240789.1) and human (NP_000326.2) Nav_v1.5 sequences are
1169 aligned, and phosphorylation sites identified on the mouse sequence and conserved in human are
1170 highlighted in red. Two phosphorylation site locations are possible at amino acids S1056-T1058 (in
1171 green). Transmembrane segments (S1-S6) in each domain (I-IV) are in bold and underlined in black;
1172 loops I, II and III correspond to interdomains I-II, II-III and III-IV, respectively. The seven
1173 phosphorylation clusters analyzed electrophysiologically are boxed in red.

1174
1175 **Figure 3 - Figure Supplement 2.** Distributions and mean \pm SEM membrane potentials for half-activation
1176 (A) and half-inactivation (C), peak Na⁺ current (I_{Na}) densities (B), and time constants of recovery from
1177 inactivation (D) of WT and mutant Nav_v1.5 channels. Currents were recorded as described in the legend to
1178 **Figure 3**. The I_{Na} densities presented were determined from analyses of records obtained on
1179 depolarizations to -20 mV (HP=-120 mV). * p <0.05 versus Nav_v1.5-WT; one-way ANOVA followed by
1180 the Dunnett's post-hoc test. *** p <0.001 versus Nav_v1.5-WT; Kruskal-Wallis followed by the Dunn's post-
1181 hoc test. Current densities, time- and voltage-dependent properties, as well as statistical comparisons
1182 across groups, are provided in **Figure 3 - Table Supplement 1**.

1183
1184 **Figure 4.** Phosphorylation at S664 and S667 regulates the voltage-dependence of current activation,
1185 whereas phosphorylation at S671 regulates the peak Na⁺ current density. Currents were recorded as
1186 described in the legend to **Figure 3**. The voltage-dependence of current activation is shifted towards more
1187 depolarized potentials in cells expressing Nav_v1.5-S664A (A), Nav_v1.5-S664E (A), Nav_v1.5-S667A (B) or
1188 Nav_v1.5-S667E (B), compared to cells expressing Nav_v1.5-WT, whereas no significant differences are
1189 observed with the Nav_v1.5-T670 (C) or Nav_v1.5-S671 (D) phosphomutants. (E to H) The mean \pm SEM
1190 peak Na⁺ current (I_{Na}) densities are plotted as a function of test potential. The peak I_{Na} density is reduced
1191 in cells expressing Nav_v1.5-S671E (H), compared to cells expressing Nav_v1.5-WT, whereas no significant
1192 differences are observed with the other phosphomutants. Current densities, time- and voltage-dependent
1193 properties, as well as statistical comparisons across groups, are provided in **Figure 4 - Table Supplement**
1194 **1**.

1195
1196 **Figure 4 - Figure Supplement 1.** Distributions and mean \pm SEM TTX-sensitive late Na⁺ current (I_{NaL})
1197 densities of quadruple S664-671 (A) and simple S671 (B) Nav_v1.5 phosphomutants. TTX-sensitive I_{NaL}
1198 were evoked during prolonged depolarizations (350 ms at -20 mV, HP=-120 mV) forty-eight hours after
1199 transfection of HEK-293 cells with WT (black), phosphosilent (blue) and phosphomimetic (red) Nav_v1.5
1200 channels and Nav β 1. No significant differences between mutant and WT channels were observed.

1201
1202 **Figure 5.** Phosphorylation at S671 regulates the cell surface expression of Nav_v1.5. (A) Representative
1203 western blots of total (left panel) and cell surface (right panel) Nav_v1.5 from HEK-293 cells transiently
1204 transfected with Nav_v1.5-WT + Nav β 1, Nav_v1.5-S671A + Nav β 1 or Nav_v1.5-S671E + Nav β 1. Samples were
1205 probed in parallel with the anti-transferrin receptor (TransR) and anti-glyceraldehyde 3-phosphate
1206 dehydrogenase (GAPDH) antibodies. (B) Mean \pm SEM total and cell surface Nav_v1.5 protein expression in
1207 transiently transfected HEK-293 cells (n=12 in 6 different experiments). Expression of Nav_v1.5 in each
1208 sample was first normalized to the TransR protein in the same blot and then expressed relative to Nav_v1.5
1209 protein expression (total or cell surface) in cells transfected with Nav_v1.5-WT + Nav β 1. Relative (mean \pm

Proteomic and functional mapping of cardiac Nav1.5 channel phosphorylation

1210 SEM) Nav_v1.5 cell surface expression is different (***) $p < 0.001$, one-way ANOVA followed by the
1211 Dunnett's post-hoc test) in cells expressing Nav_v1.5-WT, Nav_v1.5-S671A and Nav_v1.5-S671E channels.

1212
1213 **Figure 6.** Simulations of phosphorylation of segments of the first intracellular linker loop of Nav_v1.5. The
1214 sequential distance between pair of residues is on the x-axis, and the average spatial distance between a
1215 pair of residues separated by the specified sequential distance is on the y-axis. $\langle R_{ij} \rangle$ is the average
1216 simulated spatial distance between all residue pairs separated in the amino acid sequence by $|j-i|$ residues.
1217 The WT sequences are plotted in black. Phosphorylation is simulated by single or multiple replacement of
1218 serines/threonines with glutamates (E), and resulting simulations are plotted in gradation of reds. The
1219 Flory Random Coil (FRC, in blue) and Excluded Volume (EV, in purple) limits are plotted for reference
1220 (see text). **(A)** Sequence 441-480 contains the phosphosites S457, S459 and S460; **(B)** sequence 465-501
1221 contains the phosphosites S483, S484 and T486; **(C)** sequence 481-515 contains the phosphosites S497
1222 and S499; and **(D)** sequence 651-684 contains the phosphosites S664, S667, T670 and S671.

1223
1224 **Table 2 - Figure Supplement 1.** Representative MS/MS spectra of singly or doubly phosphorylated
1225 Nav_v1.5, Nav_v1.4 and Nav_v1.3 tryptic peptides (listed in **Table 2 & Table 2 - Table Supplement 1**). The
1226 presence of the b- (highlighted in blue) and y- (in red) ion series describing the amino acid sequences, and
1227 of the unphosphorylated and phosphorylated site-discriminating ions unambiguously supported the
1228 assignments of the indicated phosphorylation site(s). The PEAKS -10lgP peptide scores and the mass
1229 errors of parent ions (in ppm) for each phosphopeptide are indicated at the top of each page. The charge
1230 state confirmations of site-discriminating ions are presented in **Table 2 & Table 2 - Table Supplement**
1231 **1.**

Table 1. Proteins identified in immunoprecipitated Na_v channel complexes from Sham and TAC mouse left ventricles using MS

Protein	UniProt accession number	Number of exclusive unique peptides	% Amino acid sequence coverage	TAC/Sham ratio	Protein	UniProt accession number	Number of exclusive unique peptides	% Amino acid sequence coverage	TAC/Sham ratio
Na _v 1.5 (Q1080)	K3W4N7	310	56%	1.0	N-cadherin	P15116	13	24%	0.8
Na _v 1.5 (Q1080del)	Q9JJV9				Plakophilin-2	Q9CQ73	13	20%	0.7
Na _v 1.4	G3X8T7	86	40%	0.8	Plakophilin-1	P97350	5	8%	0.8
Na _v 1.3	A2ASI5	24	17%	0.9	Telethonin	O70548	5	44%	0.8
Na _v 1.8	Q6QIY3	13	9%	0.9	Desmoglein-2	O55111	13	19%	0.7
Na _v 1.7	Q62205	3	2%	0.7	Flotillin-1	O08917	22	59%	0.9
Na _v 1.9	Q9R053	1	1%	1.2	Flotillin-2	Q60634	21	54%	0.8
Na _v 1.1	A2APX8	1	0.5%	1.3	14-3-3 zeta/delta	P63101	5	27%	0.9
Na _v 1.2	B1AWN6	1	0.5%	1.2	14-3-3 epsilon	P62259	3	17%	1.0
Na _v 1.6	F6U329	1	0.6%	1.0	14-3-3 gamma	P61982	3	14%	1.0
Navβ4	Q7M729	11	44%	0.7	14-3-3 beta/alpha	Q9CQV8	1	6%	1.1
Navβ1	P97952	9	41%	1.0	14-3-3 sigma	O70456	1	3%	0.9
Navβ2	Q56A07	6	37%	0.8	Slmap	Q3URD3	1	1%	1.1
Calmodulin	Q3UKW2	12	53%	0.8	αB-crystallin	P23927	14	71%	0.7
FHF2-VY	P70377	37	84%	0.8	Cx43	P23242	15	50%	0.7
FHF4	P70379	1	7%	0.7	Kir2.1	P35561	3	11%	0.8
Ankyrin-G	G5E8K5	47	32%	1.0	CaMKII _γ	Q923T9	11	26%	0.8
Ankyrin-R	Q02357	2	2%	1.0	CaMKII _δ	E9Q1T1	2	6%	1.1
Ankyrin-B	S4R245	1	0.4%	0.8	CaMKII _α	P11798	2	4%	0.8
Dystrophin	P11531	88	29%	0.9	CaMKII _β	Q5SVI2	1	3%	0.9
α-1-syntrophin	A2AKD7	20	53%	0.8	PKA, catalytic subunit, α	P05132	2	9%	1.0
β-2-syntrophin	Q61235	19	35%	0.9	PKAβ-2	Q6PAM0	1	4%	1.1
α-actinin-2	Q9JI91	50	60%	0.5	PKCβ	P68404	2	3%	1.6
Caveolin-1	P49817	6	39%	0.8	Fyn	P39688	1	2%	1.1
Caveolin-2	Q9WVC3	3	28%	0.9	PP2A-C	P63330	1	3%	1.1
Caveolin-3	P51637	2	11%	0.8					
Vinculin	Q64727	25	29%	0.7					

The numbers of exclusive unique peptides, the percent (%) amino acid sequence coverages and the fold change abundance ratios in TAC LV (n=5) versus Sham LV (n=4) mNa_vPAN-IPs for each identified protein are presented. No significant differences in protein abundance were observed between TAC and Sham IPs. Abbreviations: Na_v, voltage-gated Na⁺ channel; FHF, Fibroblast growth factor Homologous Factor; Slmap, sarcolemmal membrane-associated protein; Cx, connexin; Kir, inward rectifier K⁺ channel; CaMKII, Ca²⁺/Calmodulin-dependent protein Kinase II; PKA, Protein Kinase A; PKC, Protein Kinase C. PP2A-C, Catalytic subunit of Protein Phosphatase 2A.

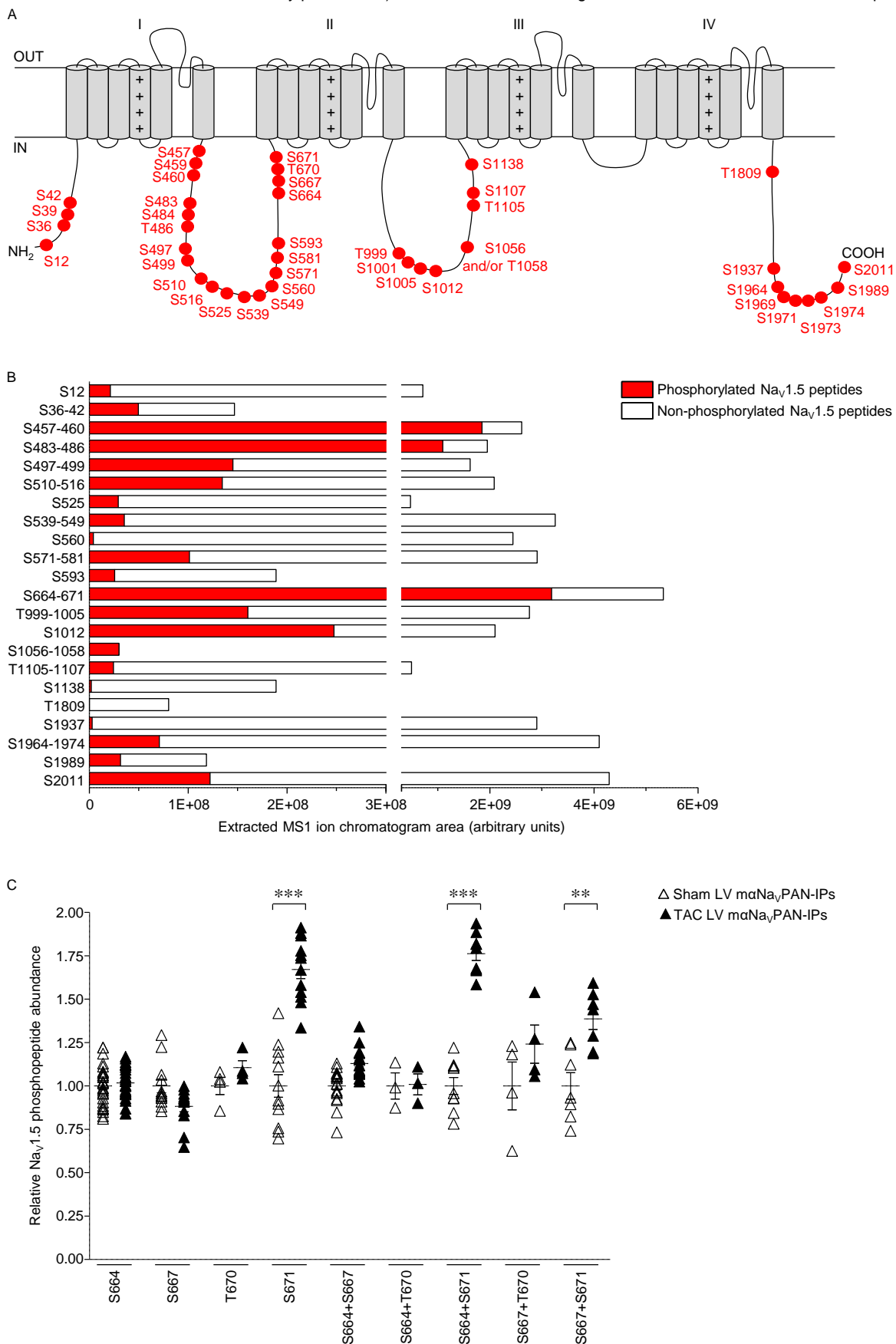
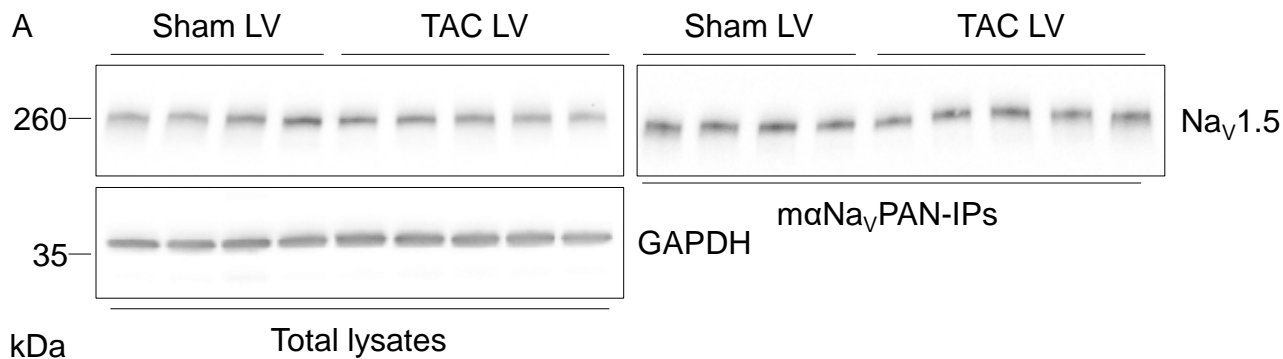


Figure 1.

Figure 1 - Table Supplement 1. Echocardiographic parameters of Sham and TAC mice before and 5 weeks after surgery

	Before surgery			After surgery			Sham before/after surgery	TAC before/after surgery
	Sham (n=4)	TAC (n=5)	<i>p</i> value	Sham (n=4)	TAC (n=5)	<i>p</i> value	<i>p</i> value	<i>p</i> value
BW (g)	27.1 ± 1.0	26.9 ± 0.7	0.905	28.8 ± 0.9	29.3 ± 0.6	0.905	0.200	0.095
HR (bpm)	455 ± 14	468 ± 20	0.905	472 ± 9	479 ± 4	0.556	0.343	0.421
LVAW;d (mm)	0.87 ± 0.05	0.91 ± 0.05	0.730	1.10 ± 0.03	1.04 ± 0.05	0.556	0.029	0.151
LVID;d (mm)	3.97 ± 0.15	3.74 ± 0.10	0.190	3.98 ± 0.23	4.03 ± 0.12	0.905	1.000	0.151
LVPW;d (mm)	0.82 ± 0.02	0.73 ± 0.04	0.176	0.78 ± 0.05	1.05 ± 0.06	0.032	0.686	0.012
LVM (mg)	99.1 ± 6.5	87.7 ± 4.9	0.286	120.2 ± 7.8	138.3 ± 9.6	0.286	0.114	0.008
LVM/BW (mg/g)	3.7 ± 0.2	3.2 ± 0.1	0.286	4.2 ± 0.2	4.7 ± 0.3	0.190	0.343	0.008
LV vol;d (μl)	69.3 ± 6.0	60.1 ± 4.0	0.190	70.2 ± 9.3	71.8 ± 5.1	0.905	1.000	0.151
SV (μl)	42.3 ± 4.7	39.7 ± 4.5	0.556	43.8 ± 5.5	29.3 ± 2.1	0.063	0.686	0.095
CO (mL/min)	19.2 ± 2.1	18.5 ± 2.1	0.905	20.6 ± 2.6	14.0 ± 1.0	0.063	0.686	0.095
EF (%)	60.9 ± 3.6	65.4 ± 3.5	0.730	62.5 ± 1.2	40.8 ± 0.9	0.016	1.000	0.008
MG (mmHg)	N/A	N/A	N/A	1.1 ± 0.2	12.1 ± 2.7	0.016	N/A	N/A

All values are means ± SEM. *p* values were obtained using the Mann-Whitney test. Abbreviations: BW, body weight; HR, heart rate; LVAW;d, LV anterior wall thickness at end-diastole; LVID;d, LV inner diameter at end-diastole; LVPW;d, LV posterior wall thickness at end-diastole; LVM, LV mass; LVM/BW, LV mass to body weight ratio; LV vol;d, LV volume at end-diastole; SV, stroke volume; CO, cardiac output; EF, ejection fraction; MG, mean gradient; bpm, beats per minute.



B

Sample	Channel	Normalization factor
Sham LV 2	TMT10-127N	1.04
Sham LV 6	TMT10-127C	0.99
Sham LV 9	TMT10-128N	1.15
Sham LV 10	TMT10-128C	0.99
TAC LV 3	TMT10-129N	1.17
TAC LV 4	TMT10-129C	1.00
TAC LV 5	TMT10-130N	1.26
TAC LV 7	TMT10-130C	1.08
TAC LV 8	TMT10-131	1.22

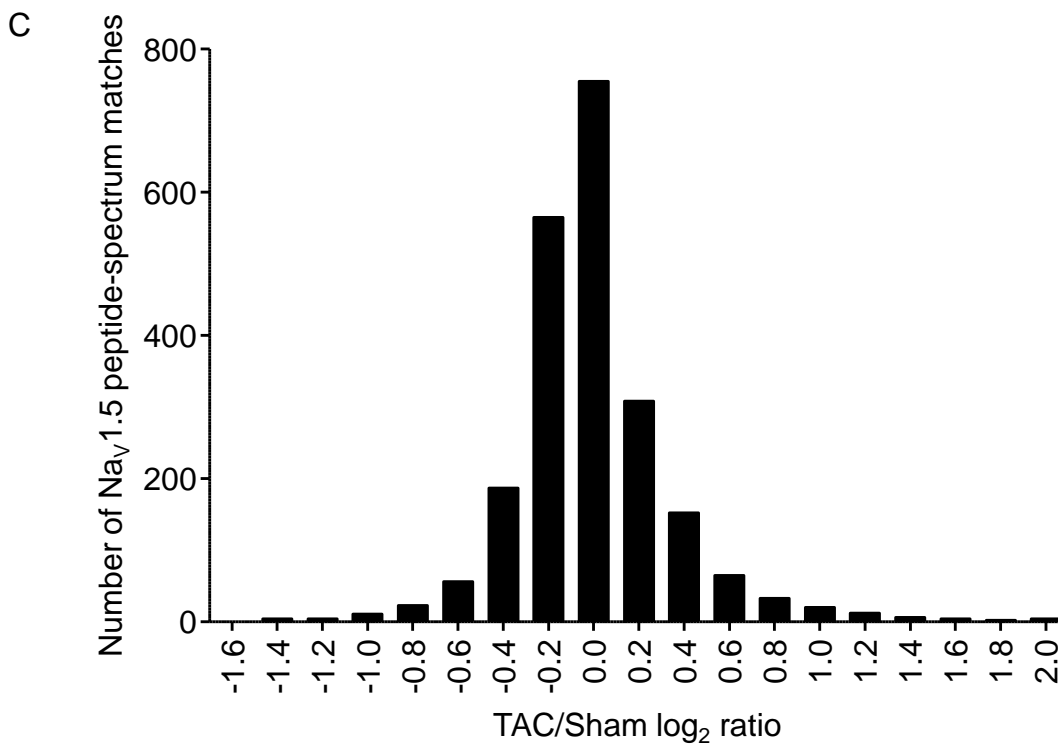


Figure 1 - Figure Supplement 1.

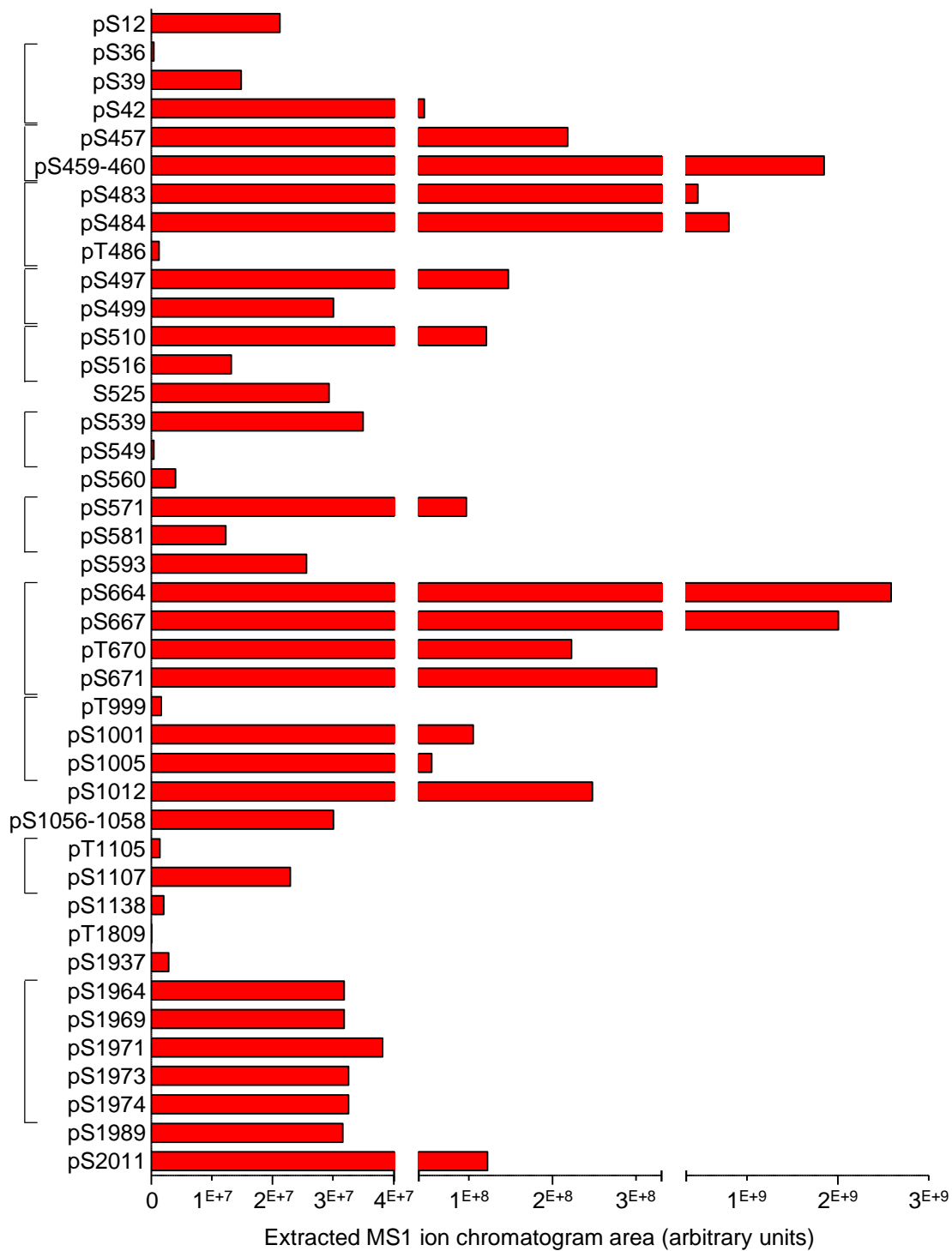


Figure 1 - Figure Supplement 2.

Table 2. Phosphorylation sites, phosphopeptides and site-discriminating ions identified in immunoprecipitated Na_v1.5 proteins from Sham and TAC mouse left ventricles using MS

Phosphorylation site(s)	Phosphopeptide sequence	m/z (charge)	-10lgP score	b ion	Phospho b ion	y ion	Phospho y ion	TAC/Sham ratio
S12	9-GTS(pS)FRR	560.279(+2)	21.6	b3 (+1)	(-)	y3	(-)	1.2 (n=1)
S36	35-G(pS)ATSQESR	616.279(+2)	32.1	b1	(-)	y7	(-)	1.3 (n=1)
S42	35-GSATSQE(pS)REGLPEEEAPRQLDLQASK	887.947(+4)	73.1	b7 (+1)	(-)	y19 (+2)	y21 (+2)	1.5 ± 0.03 (n=3)
S39 + S42	35-GSAT(pS)QE(pS)REGLPEEEAPRQLDLQASK	907.937(+4)	68.4	b4 (+1)	(-)	y19 (+2)	y21	1.2 ± 0.12 (n=2)
S457 (+ S459 or S460)	452-GVDTV(pS)RSSLEMSPLAPVTNHER	957.782(+3)	77.1	b5 (+1)	b7(-98) (+2)	y14 (+1)	(-)	1.1 ± 0.09 (n=10)
S459 + S460	452-GVDTVSR(pS)(pS)LEMSPLAPVTNHER	958.117(+3)	41.5	b7 (+2)	b11 (+2)	y12 (+1)	(-)	1.2 (n=1)
S460	459-S(pS)LEMSPLAPVTNHER	1039.003(+2)	61.2	b1 (+1)	b4 (+1)	y14 (+1)	(-)	1.0 ± 0.05 (n=18)
S483	481-RL(pS)SGTEDGGDDRLPK	561.038(+4)	52.4	b2	b3	y13 (+2)	(-)	1.0 ± 0.03 (n=10)
S484	482-LS(pS)GTEDGGDDRR	759.319(+2)	45.7	b2	(-)	y9 (+1)	(-)	1.2 ± 0.07 (n=12)
T486	484-SG(pT)EDGGDDRLPK	628.973(+3)	21.9	b1	b5	y8 (+2)	(-)	1.2 (n=1)
S483 + S484	480-KRL(pS)(pS)GTEDGGDDRLPK	536.476(+5)	63	b3	(-)	y12 (+2)	(-)	1.3 ± 0.04 (n=19)
S497	482-LSSGTEDEGGDDRLPK(pS)DSEDGPR	732.845(+4)	60.2	b12 (+2)	(-)	y7 (+1)	y12	1.3 ± 0.07 (n=7)
S483 + S497	481-RL(pS)SGTEDEGGDDRLPK(pS)DSEDGPR	791.862(+4)	40.1	b2	b3 (-98)	y6 (+1)	y12 (+2)	0.7 (n=1)
S484 + S497	482-LS(pS)GTEDGGDDRLPK(pS)DSEDGPR	1003.448(+3)	54.8	b2 (+1)	b3	y7 (+1)	y12 (+2)	1.7 ± 0.04 (n=2)
S499	497-SD(pS)EDGPR	586.245(+2)	42	b2	b5	y4 (+1)	y6	1.4 ± 0.17 (n=3)
S510	505-ALNQL(pS)LTHTGLSR	573.643(+3)	51.8	b4 (+1)	(-)	y7 (+1)	(-)	0.9 ± 0.03 (n=3)
S516	505-ALNQLSLTHTGL(pS)R	573.644(+3)	46.7	b9	(-)	y1 (+1)	(-)	0.9 (n=1)
S525	524-S(pS)RGSIFTFR	489.584(+3)	40.7	b1 (+1)	(-)	y8 (+2)	(-)	0.8 ± 0.09 (n=3)
S539	536-DQG(pS)EADFADDENSTAGESESHR	921.701(+3)	70.9	b3 (+1)	b5 (+1)	y14 (+1)	(-)	1.5 ± 0.09 (n=9)
S549	534-RRDQGSSEADFADDEN(pS)TAGESESHR	769.579(+4)	55.3	b15 (+2)	(-)	y9 (+1)	(-)	3.2 (n=1)
S560	559-T(pS)LLVPWPLR	745.921(+2)	30.2	b1	b4	y8 (+1)	(-)	1.0 (n=1)
S571	569-RP(pS)TQQQPGFGTSAPGHVNLGK	911.466(+3)	55.2	b1 (+1)	b7 (+1), b7 (+2)	y19	(-)	0.8 ± 0.03 (n=19)
S581	569-RPSTQQQPGFGT(pS)APGHVNLGK	683.856(+4)	48.5	b12 (+2)	(-)	y8 (+2)	(-)	0.9 (n=1)
S593	591-RN(pS)TVDCNGLVSVLLGAGDAEATSPGSHLLR	841.660(+4)	71.7	b2	b3	y16 (+1)	(-)	0.8 ± 0.05 (n=4)
S664	662-AL(pS)AVSVLTSALEELEESHK	936.506(+3)	60.6	b2 (+1)	b5 (+1)	y18 (+2)	(-)	1.0 ± 0.04 (n=28)
S667	662-ALSAV(pS)VLTSALEELEESHK	817.416(+3)	64.1	b5 (+1)	b7 (+1)	y13 (+1)	(-)	0.9 ± 0.06 (n=12)
T670	662-ALSAVSVL(pT)SALEELEESHK	702.629(+4)	54.3	b7 (+1)	(-)	y12 (+2)	(-)	1.1 ± 0.1 (n=4)
S671	662-ALSAVSVLT(pS)ALEELEESHK	702.629(+4)	63.2	b9 (+2)	b10 (+2)	y11 (+2)	(-)	1.7 ± 0.17 (n=12)***
S664 + S667	662-AL(pS)AV(pS)VLTSALEELEESHK	886.771(+3)	58.8	b2	b3	y15 (+2)	y18	1.1 ± 0.05 (n=18)
S664 + T670	662-AL(pS)AVSVL(pT)SALEELEESHK	844.072(+3)	59.3	b2 (+1)	b5 (+1), b8 (+1)	y11 (+1)	(-)	1.0 ± 0.14 (n=3)
S664 + S671	662-AL(pS)AVSVLT(pS)ALEELEESHK	844.072(+3)	58.3	b2 (+1)	b5 (+1), b9 (+2)	y10 (+1)	(-)	1.8 ± 0.13 (n=9)***
S667 + T670	662-ALSAV(pS)VL(pT)SALEELEESHK	722.621(+4)	54.1	b5 (+1)	b8	y12 (+2)	(-)	1.2 ± 0.37 (n=4)
S667 + S671	662-ALSAV(pS)VLT(pS)ALEELEESHK	844.073(+3)	60.5	b5 (+1)	b8 (+1), b9	y10 (+1)	(-)	1.4 ± 0.17 (n=7)**
T999	993-KPAALA(pT)HSQLPSCIAAPR	824.114(+3)	48.8	b6 (+1)	(-)	y12 (+1)	(-)	0.8 (n=1)
S1001	1001-(pS)QLPSCIAAPR	503.591(+3)	32.6	(-)	b2 (+1)	y8 (+1)	(-)	1.0 ± 0.11 (n=4)
S1005	993-KPAALATHSQLP(pS)CIAAPRSPPPPEVEKAPPAR	702.389(+6)	71.4	b11 (+2)	(-)	y18 (+2)	y21 (+2)	0.8 ± 0.16 (n=2)
S1012	1012-(pS)PPPEVEK	759.405(+2)	42.3	(-)	b1 (+1)	y8 (+1)	(-)	0.9 ± 0.03 (n=17)
S1056 and/or T1058	1030-FEEDKRPQGTPGDTEPVCVPIAIAESDTEDEEENSLGT EEEESSK (1 Phospho)	1230.559(+5)	57.3	b24 (+2)	(-)	y11 (+1)	(-)	1.8 ± 0.04 (n=5)
T1105	1097-AWSQVSET(pT)SSEAEASTSQADWQQR	1070.132(+3)	64.3	b8 (+1)	b9	y12 (+1)	(-)	1.1 (n=1)
S1107	1097-AWSQVSETTS(pS)EAEASTSQADWQQR	1070.135(+3)	69.9	b10 (+1)	b15 (+1)	y14 (+1)	(-)	1.2 (n=1)
S1138	1136-ED(pS)YSEGSTADMTNTADLLEIQIPDLGEDVKDPEDCFTEGCVR	1312.582(+4)	44.7	(-)	b3 (+1)	y23 (+2)	(-)	1.3 ± 0.01 (n=2)
T1809	1809-(pT)QFIEYLALSDFADALSEPLR	903.451(+3)	54.8	(-)	b1, b2 (+1)	y14 (+1)	(-)	0.8 (n=1)
S1937	1933-QQAG(pS)SGLSDEDAPER	978.430(+2)	60.1	b4 (+1)	(-)	y11 (+1)	(-)	1.3 (n=1)
S1964	1964-(pS)GPLSSSSISSTSFPPSYDSVTR	885.752(+3)	50.3	(-)	b1 (+1), b4 (+1)	y14 (+1)	(-)	1.2 ± 0.11 (n=3)
S1969	1964-SGPLS(pS)SSISSTSFPPSYDSVTR	885.753(+3)	56.9	b5	b6 (+2)	y14 (+1)	(-)	1.0 ± 0.04 (n=3)
S1971	1963-RSGPLSSS(pS)SSTSFPPSYDSVTR	937.787(+3)	48.5	b8 (+1)	(-)	y14 (+1)	(-)	0.9 ± 0.09 (n=3)
S1973	1964-SGPLSSS(pS)STSFPPSYDSVTR	885.750(+3)	61.8	b9 (+1)	b10 (+2)	y13	(-)	0.9 ± 0.02 (n=6)
S1974	1964-SGPLSSS(pS)TSFPPSYDSVTR	885.750(+3)	61.8	b10	(-)	y12 (+1)	(-)	0.9 ± 0.03 (n=2)
S1989	1987-AT(pS)DNLPVR	641.324(+2)	37.7	b2	b5	y6 (+1)	(-)	0.8 ± 0.07 (n=2)
S2011	2002-SEDLADFP(pS)PDRDR	675.975(+3)	38.8	b7 (+1)	(-)	y5 (+2)	y8	1.0 ± 0.05 (n=15)

The site-discriminating ions observed in MS/MS spectra of each annotated Na_v1.5 (UniProt reference sequence K3W4N7) phosphopeptide support the assignment of the indicated phosphorylation site(s). The -10lgP scores attest quality of peptide identification. The manually verified charge state of unphosphorylated and phosphorylated site-discriminating b and y ions is reported in parentheses. The (-) symbol indicates that the ion was not detected. Mean ± SEM phosphopeptide abundance ratios in TAC LV (n=5) versus Sham LV (n=4) maNa_vPAN-IPs were calculated from n phosphopeptide(s). **, p < 0.01; ***, p < 0.001, Mann-Whitney test.

Table 2 - Table Supplement 1. Phosphorylation sites, phosphopeptides and site-discriminating ions identified in co-immunoprecipitated Na_v α subunits from Sham and TAC mouse left ventricles using MS

Na _v α subunit	Phosphorylation site(s)	Phosphopeptide sequence	m/z (charge)	-10lgP	b ion	Phospho b ion	y ion	Phospho y ion	TAC/Sham ratio
Na _v 1.4	S522 + S525	512-GPPRPSCSAE(pS)AI(pS)DAMEELEEAAHQK	861.889 (+4)	48.1	b10 (+2)	b12	y11	(-)	1.0 ± 0.01 (n=2)
Na _v 1.4	S525	512-GPPRPSCSAESA(pS)AI(pS)DAMEELEEAAHQK	841.893 (+4)	60.3	b13 (+2)	b15 (+2)	y10 (+2)	(-)	1.0 ± 0.07 (n=2)
Na _v 1.4	S900	899-S(pS)IEMDHLNFNNPYLTIHVPIASEESDLEMPTEEETDTFSEPEDIK	1486.948 (+4)	54.2	b1	b2	(-)	(-)	1.3 (n=1)
Na _v 1.4	S1819	1790-EKDSTEDAGPTTEVTAPSSSDTALTPPPP(pS)PPPPSSPPQGQTVRPGVK	927.474 (+6)	52.0	(-)	(-)	y18 (+2)	y19 (+2)	0.7 ± 0.17 (n=2)
Na _v 1.3	S658	656-AM(pS)IASILTNTMEELEESR	817.386 (+3)	64.0	b2	b5	(-)	(-)	0.7 (n=1)

The site-discriminating ions observed in MS/MS spectra of each annotated Na_v1.4 and Na_v1.3 phosphopeptide support the assignment of the indicated phosphorylation site(s). The -10lgP scores attest quality of peptide identification. The manually verified charge state of unphosphorylated and phosphorylated site-discriminating b and y ions is reported in parentheses. The (-) symbol indicates that the ion was not detected. Mean ± SEM phosphopeptide abundance ratios in TAC LV (n=5) versus Sham LV (n=4) mdNa_vPAN-IPs were calculated from n phosphopeptide(s). No significant differences between TAC and Sham IPs were observed.

1 MANFLLPRGTSSFRRTFTRESLAAIEKRMAEKQARGSATSQESREGLPEEEAPRPQLDLQASKKLPDLYGNPPREL
 N-TERM
 76 IGEPLEDLDPFYSTQKTFIVLNKGTKTIFRFSATNALYVLSFPFHPVRAAVKILVHSLFMSLIMCTILTNCVFMAQ
 N-TERM IS1
 151 HDPPPWTKYVEYFTTATAYTFESLVKILARGFCLHAFTFLRDPWNWLDFSVIVMAYTTEFVDLGNVSALRTRFRVLR
 IS2 IS3 IS4
 226 ALKTISVISGLKTIVGALIQSVKKLADVMVLTVFCLSVFALIGLQLEFMGNLRHKCVRNFTELNGTNGSVEADGIV
 IS5
 301 WNSLDVYLNDPANYLLKNGTTDVLCCGNSSDAGTCPEGYRCLKAGENPDHGYSFDSFAWAFLALFRIMTQDCWE
 376 RLYQQTLRSAGKIYMIFFMLVIFLGSFYLVNLI LAVVAMAYEEQNQATIAETEEKKRFQEAMEMLKKEHEALTI
 IS6
 451 RGVDTVSRSSLEMSPLAPVTNHERRSKRRKRLSSGTEEDGGDRLPKSDSEDPALRNQLSLTHGLSRRTSMRPRSS
 Loop I
 526 RGSIFTFRRRDQGS EADFADDENS TAGESESHRTSLLVPWPLRRPSTQGQPGFGTSPAGHVLNGKRNS TVDCNGV
 Loop I
 601 VSLLGAGDAEATSPGSHLLRPIVLDLDRPPDTTTPSEEPGGQMLTPQAPCADGFEEPGARQRALSAVSVLTSALEE
 Loop I
 676 LEESSHRKCPPCWNRFQHYLIWECCPLWMSIKQKVKFVMDPFADLTITMCIVLNTLFMALEHYNMATAEFEEMLQ
 IIS1
 751 VGNLVFTGIFTAEMTFKIIIALDPYFYFQGGWNIFDSIIIVILSIMEGLSRMGNLSVLRSEFRLLRVEFKLAKSWPTL
 IIS2 IIS3 IIS4
 826 NTLIKIIGNSVGALGNLTLVLAIIVFIFAVVGMQLFGKNYSELRRHRI SDSGLLPRWHMMDFFHAFLIIFRILCGE
 IIS5
 901 WIETMWDCEVSGQSLCLLVFLLVMVIGNLVVLNLFALLLSSFSADNLTAPDEDGEMNNLQALALARIQRGLRFV
 IIS6
 976 KRTTWDFCCGLLRRRPKKPAALATHS QLPSCIAAPRSPPPPEVEKAPPARKETRFEECDKRPQGOTPGDTEPVCVP
 Loop II
 1051 IAVAESDIDDQEEDEENSLGTEEEESSK [Q] QESQVVS GGHEPPQEPRAWSQVSETTSS EAEASTSQADWQQERE
 Loop II
 1124 AEPRAPGCGETPEDSYSEGSTADMTNTADLLEQIPDLGEDVKDPEDCFTEGCVRRCPCCMVDTTQAPGKVVWRLR
 Loop II
 1199 KTCYRIVEHSWFETFIIFMILLSSGALAFEDIYLEERKTIKVLLEYADKMFTYVFVLEMLLKWVAYGFKKYFTNA
 IIS1 IIS2
 1274 WCWLDFLIVDVSILVANLTLGFAEMGPIKSLRTRLRALRPLRALSREFGMRVVVNALVGAIPSI MNVLLVCLIFW
 IIS3 IIS4
 1349 LIFSIMGVNLFAGKFGRCINQTEGDLPLNYTIVNNKSECESFNVTGELYWTKVKVNFNDVNGAGYLALLQVATFKG
 IIS5
 1424 WMDIMYAAVDVSRGYEEQPQWEDNLYMYIYFVVFIIFGSFFTLNLFIVGVIIDNFNQOKKKLGGQDIFMTEEQKKYY
 IIS6
 1499 NAMKKLGSKKPQKPIPRPLNKYQGFIFDIVTKQAFDVTIMFLICLNMVTMMVETDDQSPEKVNILAKINLLEVAI
 Loop III IVS1 IVS2
 1574 FTGECIVKMAALRHYYFTNSWNI FDFVVVILSIVGTVLSDIQKYFFSPTLFRVIRLARIGRIILRLIRGAKGIRT
 IVS3 IVS4
 1649 LLFALMMSLPALFNI GLLLEFLVMFIYSIFGMANFAYVKEWAGIDDMFNFQTFAN SMLCLFQITTSAGWDGLLSPI
 IVS5
 1724 LNTGPPYCDPNLPNSNGSRGNCGSPAVGILFFTTYIIISFLIVVNMYIAIILENF SVATEEESTEPLSEDDDFDMFY
 IVS6
 1799 EIWEKFDPEATQFIEYLALSDFADALSEPLRIAKPNQISLINMDLPMVSGDRIHCM DILFAFTKRVLGESGEMDA
 C-TERM
 1874 LKIQMEEKFMAANPSKISYEPITTTLRKHEEVSATVIQRAFRRHLLQRSVKHASFLFRQQAGSSGLSDEDAPER
 C-TERM
 1949 EGLIAYMMNENFSRRSGPLSSSSISSTSFPFSYDSVTRATSDNLPVRASDYRSSEDLADFPSPDRDRESIV
 C-TERM

Figure 2.

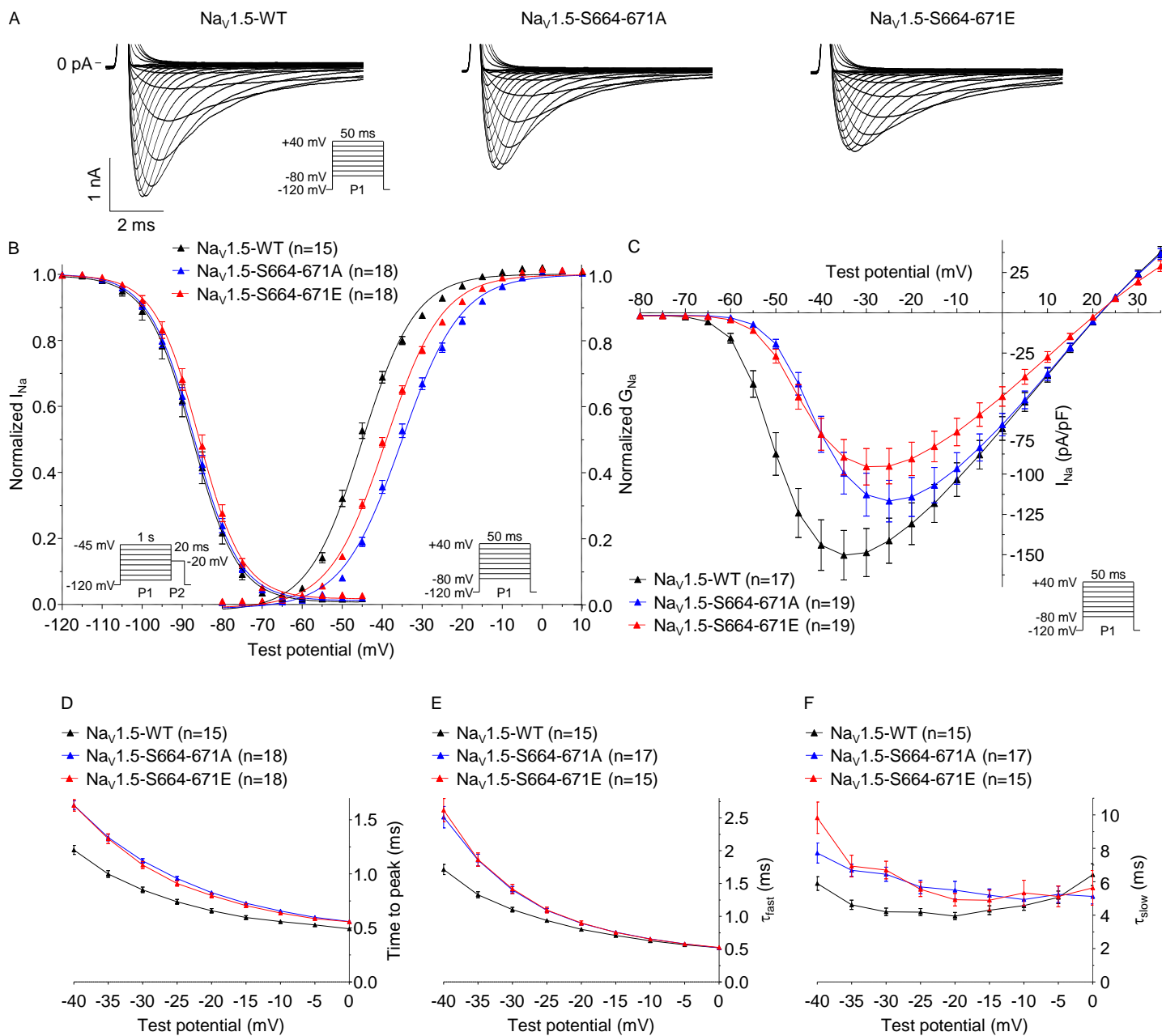


Figure 3.

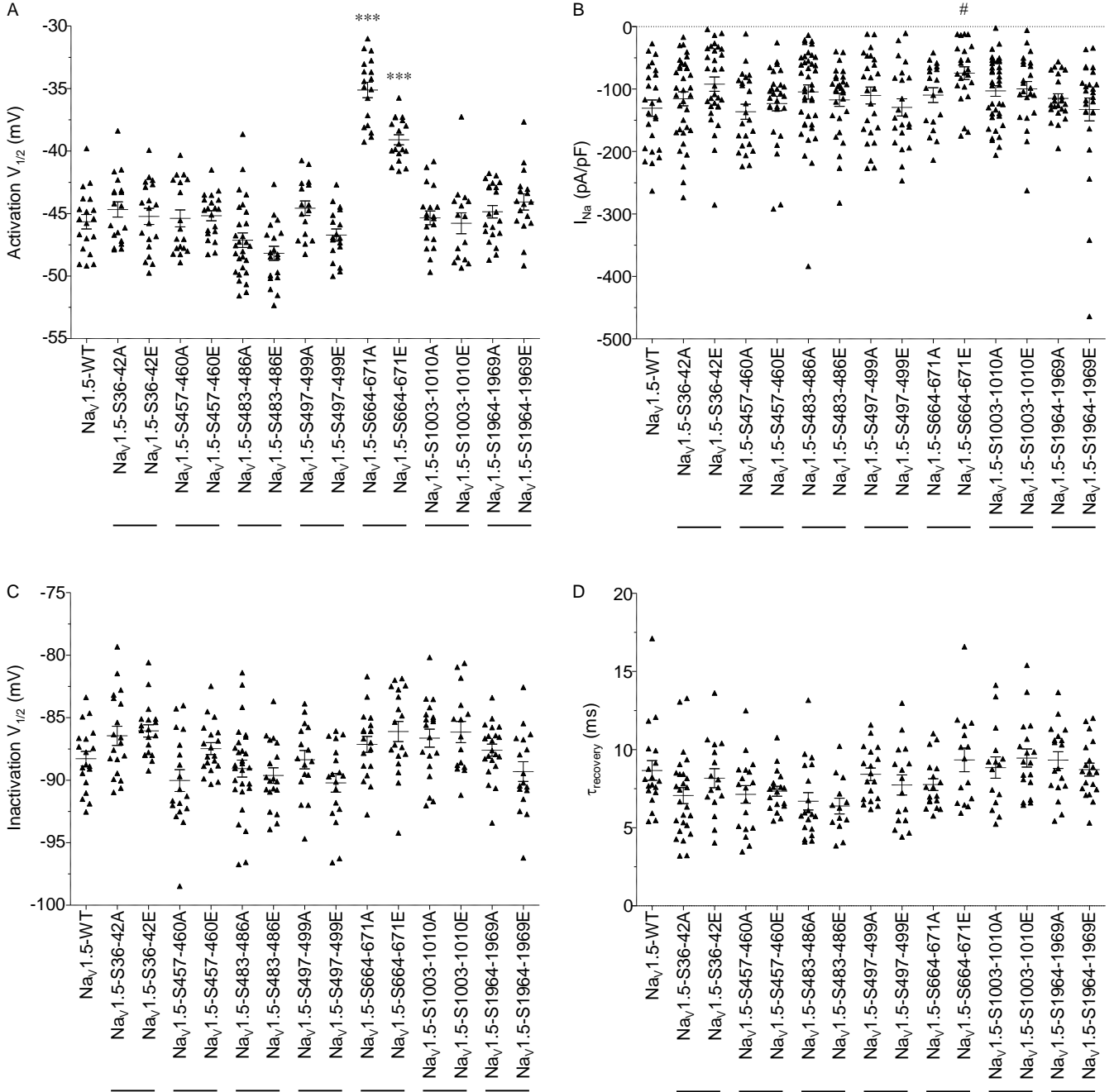


Figure 3 - Figure Supplement 2.

Figure 3 - Table Supplement 1. Current densities and properties of Na_v1.5 channels mutant for the phosphorylation clusters in transiently transfected HEK293 cells

	I _{Na} (pA/pF)	Time to peak (ms)	Time course of inactivation			Voltage-dependence of activation		Voltage-dependence of inactivation		Recovery from inactivation τ _{rec} (ms)
			τ _{fast} (ms)	τ _{slow} (ms)	A _{fast} /A _{slow}	V _{1/2} (mV)	k (mV)	V _{1/2} (mV)	k (mV)	
Nav1.5-WT	-130.8 ± 13.1 (25)	0.60 ± 0.01 (19)	0.72 ± 0.02 (18)	3.6 ± 0.2 (18)	15.5 ± 1.0 (18)	-45.7 ± 0.6 (19)	6.8 ± 0.2 (19)	-88.3 ± 0.6 (19)	4.9 ± 0.1 (19)	8.7 ± 0.6 (19)
Nav1.5-S36-42A	-115.7 ± 11.2 (35)	0.63 ± 0.02 (19)	0.75 ± 0.02 (19)	3.6 ± 0.2 (19)	13.3 ± 1.0 (19)	-44.7 ± 0.6 (19)	6.7 ± 0.1 (19)	-86.5 ± 0.8 (19)	4.9 ± 0.1 (19)	7.1 ± 0.6 (18)
Nav1.5-S36-42E	-92.2 ± 11.4 (31)	0.59 ± 0.02 (19)	0.72 ± 0.02 (17)	3.5 ± 0.2 (17)	13.6 ± 1.9 (17)	-45.2 ± 0.6 (19)	6.6 ± 0.1 (19)	-86.1 ± 0.5 (19)	4.6 ± 0.1 (19)	7.3 ± 0.3 (18)
Nav1.5-S457-460A	-136.5 ± 12.1 (24)	0.60 ± 0.01 (18)	0.75 ± 0.02 (18)	4.6 ± 0.4 (18)	15.6 ± 1.2 (18)	-45.4 ± 0.7 (18)	7.0 ± 0.2 (18)	-90.0 ± 0.9 (18)	5.2 ± 0.1 (18)	9.3 ± 0.5 (18)
Nav1.5-S457-460E	-123.3 ± 11.6 (28)	0.60 ± 0.02 (20)	0.74 ± 0.02 (19)	3.7 ± 0.2 (19)	17.5 ± 1.8 (19)	-45.2 ± 0.4 (20)	6.8 ± 0.1 (20)	-87.5 ± 0.5 (19)	4.7 ± 0.1 (19)	8.7 ± 0.4 (19)
Nav1.5-S483-486A	-104.7 ± 11.3 (40)	0.61 ± 0.02 (28)	0.61 ± 0.02 (26)	3.2 ± 0.1 (26)	12.7 ± 1.0 (26)	-47.1 ± 0.6 (28)	6.3 ± 0.2 (28)	-89.1 ± 0.7 (28)	5.0 ± 0.1 (28)	7.1 ± 0.5 (26)
Nav1.5-S483-486E	-117.4 ± 10.4 (29)	0.55 ± 0.02 (19)	0.59 ± 0.02 (16)	2.9 ± 0.2 (16)	14.2 ± 1.2 (16)	-48.2 ± 0.6 (19)	6.3 ± 0.2 (19)	-89.6 ± 0.6 (19)	4.8 ± 0.1 (19)	8.2 ± 0.6 (16)
Nav1.5-S497-499A	-110.5 ± 13.5 (25)	0.62 ± 0.02 (16)	0.76 ± 0.03 (12)	4.6 ± 0.4 (12)	18.0 ± 1.4 (12)	-44.6 ± 0.6 (16)	7.1 ± 0.1 (16)	-88.4 ± 0.7 (16)	4.8 ± 0.1 (16)	8.8 ± 0.7 (15)
Nav1.5-S497-499E	-129.5 ± 13.8 (22)	0.56 ± 0.01 (18)	0.70 ± 0.02 (17)	3.8 ± 0.2 (17)	16.7 ± 1.0 (17)	-46.7 ± 0.5 (18)	7.2 ± 0.1 (18)	-90.2 ± 0.7 (18)	4.9 ± 0.1 (18)	9.5 ± 0.6 (18)
Nav1.5-S664-671A	-109.8 ± 11.8 (19)	0.83 ± 0.02*** (18)	0.89 ± 0.02** (17)	5.5 ± 0.5* (17)	18.1 ± 1.2 (17)	-35.1 ± 0.6*** (18)	7.3 ± 0.1 (18)	-87.1 ± 0.6 (18)	5.4 ± 0.1 (18)	8.4 ± 0.4 (18)
Nav1.5-S664-671E	-74.5 ± 10.2 [#] (23)	0.80 ± 0.02*** (18)	0.90 ± 0.03* (15)	4.9 ± 0.4 (15)	18.8 ± 1.9 (15)	-39.1 ± 0.4*** (18)	7.0 ± 0.1 (18)	-86.1 ± 0.8 (18)	5.1 ± 0.1 (18)	7.7 ± 0.6 (16)
Nav1.5-S1003-1010A	-103.0 ± 8.5 (38)	0.62 ± 0.01 (19)	0.76 ± 0.02 (19)	4.2 ± 0.2 (19)	7.4 ± 0.7 (19)	-45.3 ± 0.5 (19)	6.5 ± 0.2 (19)	-86.6 ± 0.7 (19)	6.0 ± 0.2 (19)	6.7 ± 0.6 (19)
Nav1.5-S1003-1010E	-99.9 ± 11.9 (23)	0.61 ± 0.01 (15)	0.74 ± 0.02 (15)	3.9 ± 0.1 (15)	7.8 ± 0.6 (15)	-45.8 ± 0.8 (15)	6.5 ± 0.2 (15)	-86.2 ± 0.8 (15)	5.6 ± 0.2 (15)	6.4 ± 0.5 (13)
Nav1.5-S1964-1969A	-115.0 ± 7.4 (23)	0.63 ± 0.01 (21)	0.77 ± 0.02 (20)	4.1 ± 0.2 (20)	15.8 ± 0.9 (20)	-44.9 ± 0.5 (21)	6.6 ± 0.2 (21)	-87.6 ± 0.5 (21)	5.1 ± 0.1 (21)	7.8 ± 0.4 (18)
Nav1.5-S1964-1969E	-132.8 ± 18.3 (26)	0.66 ± 0.02 (17)	0.81 ± 0.02 (15)	4.0 ± 0.2 (15)	13.9 ± 0.8 (15)	-44.1 ± 0.6 (17)	7.2 ± 0.2 (17)	-89.3 ± 0.8 (17)	4.9 ± 0.1 (17)	9.3 ± 0.8 (15)

The peak Na⁺ current density (I_{Na}), time to peak, and time course of inactivation properties presented were determined from analyses of records obtained on depolarizations to -20 mV (HP=-120 mV). All values are means ± SEM. The number of cells analyzed is provided in parentheses. [#]p<0.05 versus Nav1.5-WT; one-way ANOVA followed by the Dunnett's post-hoc test. *p<0.05, **p<0.01, ***p<0.001 versus Nav1.5-WT; Kruskal-Wallis followed by the Dunn's post-hoc test.

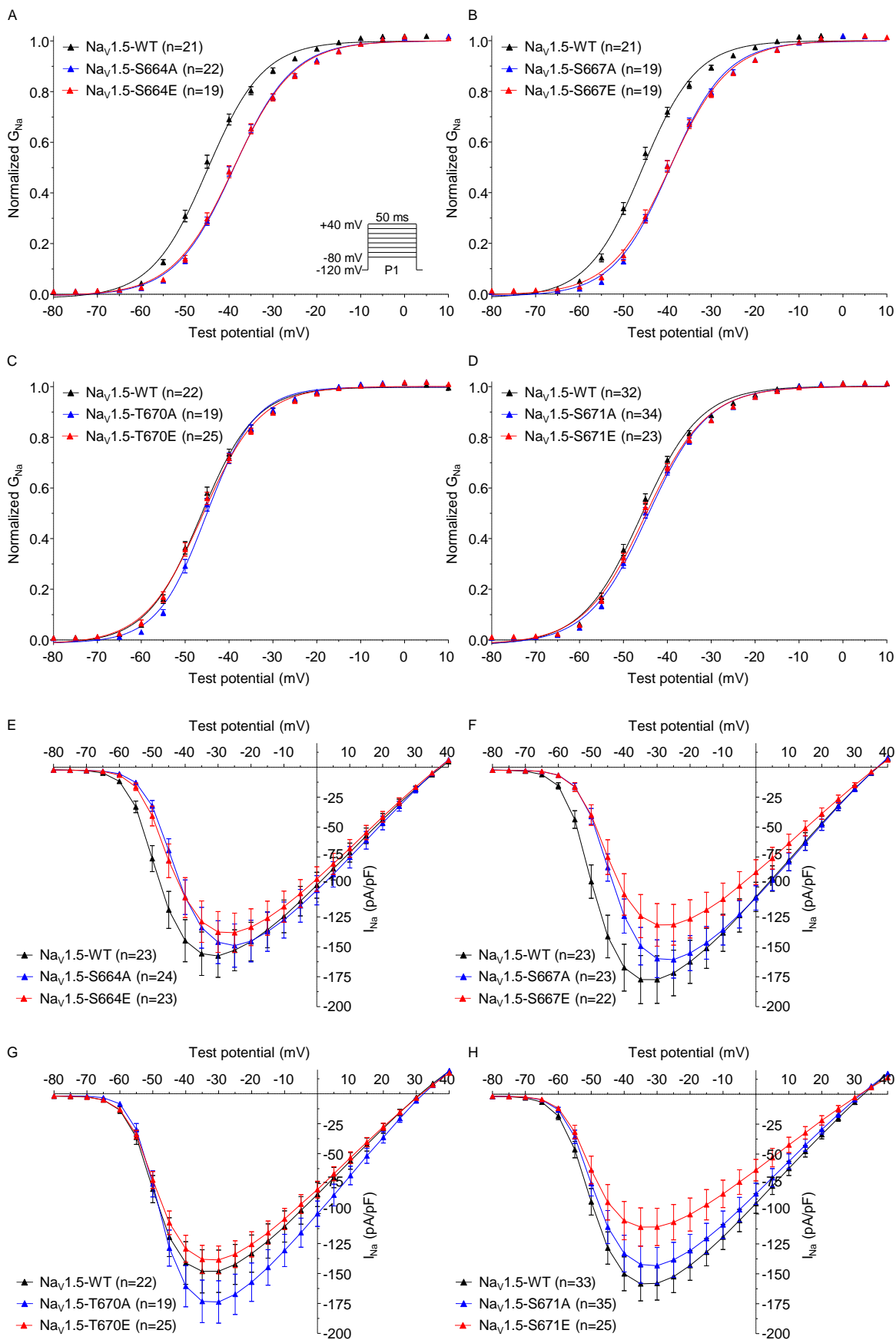


Figure 4.

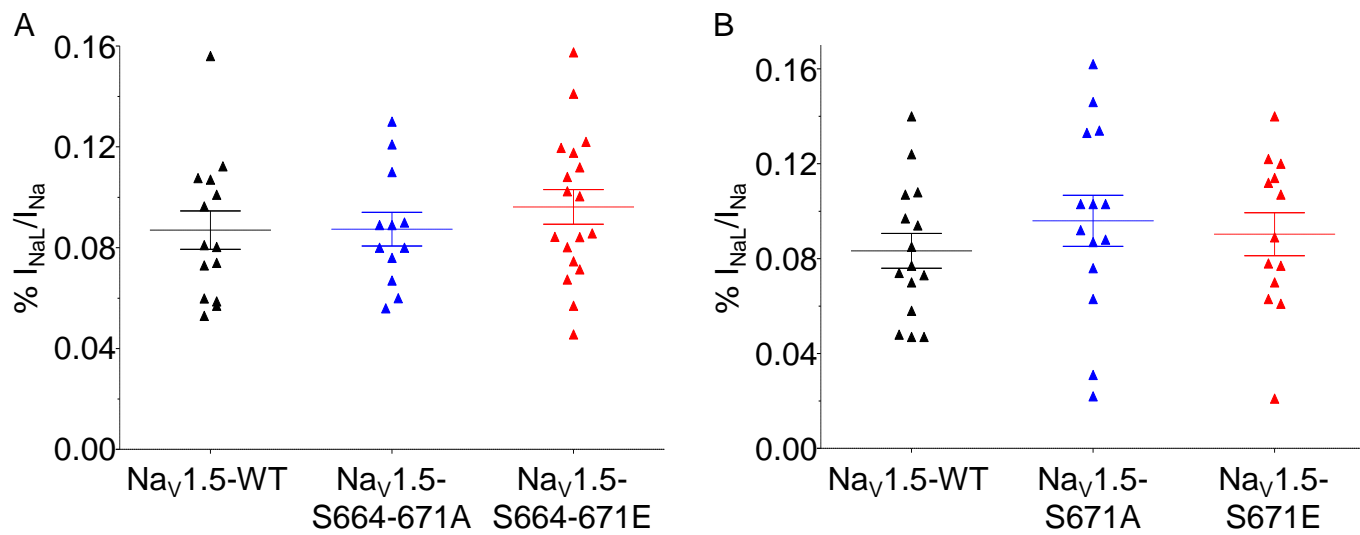


Figure 4 - Figure Supplement 1.

Figure 4 - Table Supplement 1. Current densities and properties of Na_v1.5 channels mutant for S664, S667, T670 and S671 in transiently transfected HEK293 cells

	I _{Na} (pA/pF)	Time to peak (ms)	Time course of inactivation			Voltage-dependence of activation		Voltage-dependence of inactivation		Recovery from inactivation τ _{rec} (ms)
			τ _{fast} (ms)	τ _{slow} (ms)	A _{fast} /A _{slow}	V _{1/2} (mV)	k (mV)	V _{1/2} (mV)	k (mV)	
Nav1.5-WT	-162.5 ± 18.0 (23)	0.62 ± 0.02 (21)	0.75 ± 0.02 (19)	3.3 ± 0.2 (19)	13.8 ± 1.5 (19)	-45.7 ± 0.6 (21)	6.0 ± 0.2 (21)	-85.0 ± 0.6 (21)	4.7 ± 0.1 (21)	6.0 ± 0.4 (17)
Nav1.5-S664A	-145.2 ± 17.4 (24)	0.75 ± 0.01* (22)	0.82 ± 0.02 (21)	4.1 ± 0.2 (21)	16.7 ± 1.4 (21)	-38.9 ± 0.5*** (22)	6.6 ± 0.1 (22)	-84.0 ± 0.7 (22)	4.8 ± 0.1 (22)	6.6 ± 0.6 (22)
Nav1.5-S664E	-133.6 ± 15.4 (23)	0.73 ± 0.02 (19)	0.79 ± 0.03 (14)	3.3 ± 0.2 (14)	11.7 ± 1.1 (14)	-39.0 ± 0.6*** (19)	6.7 ± 0.1 (19)	-83.4 ± 0.8 (19)	4.7 ± 0.1 (19)	6.1 ± 0.5 (19)
Nav1.5-S667A	-155.3 ± 14.6 (23)	0.75 ± 0.02 (19)	0.78 ± 0.03 (16)	3.9 ± 0.2 (16)	14.1 ± 1.0 (16)	-39.4 ± 0.5*** (19)	6.3 ± 0.2 (19)	-83.7 ± 0.6 (19)	4.9 ± 0.1 (19)	6.0 ± 0.4 (16)
Nav1.5-S667E	-126.7 ± 16.0 (22)	0.76 ± 0.02* (19)	0.81 ± 0.02 (14)	4.0 ± 0.2 (14)	14.9 ± 1.3 (14)	-39.5 ± 0.7*** (19)	6.6 ± 0.1 (19)	-83.8 ± 0.9 (19)	4.7 ± 0.1 (19)	6.7 ± 0.7 (19)
Nav1.5-T670A	-157.2 ± 16.0 (19)	0.63 ± 0.02 (19)	0.64 ± 0.02 (18)	3.0 ± 0.2 (18)	11.2 ± 1.5 (18)	-45.1 ± 0.6 (19)	5.4 ± 0.2 (19)	-86.9 ± 0.9 (16)	4.8 ± 0.1 (16)	8.4 ± 0.6 (14)
Nav1.5-T670E	-125.7 ± 10.5 (25)	0.59 ± 0.02 (25)	0.70 ± 0.02 (22)	3.5 ± 0.4 (22)	14.3 ± 1.9 (22)	-46.2 ± 0.7 (25)	6.3 ± 0.2 (25)	-87.7 ± 1.0 (20)	4.6 ± 0.1 (20)	9.8 ± 1.0 (20)
Nav1.5-S671A	-130.7 ± 13.7 (35)	0.54 ± 0.02 (34)	0.59 ± 0.02 (25)	2.3 ± 0.1 (25)	10.3 ± 0.9 (25)	-44.4 ± 0.5 (34)	6.5 ± 0.1 (34)	-84.9 ± 0.6 (32)	4.5 ± 0.1 (32)	5.6 ± 0.3 (30)
Nav1.5-S671E	-100.6 ± 13.8 [#] (25)	0.52 ± 0.01 (23)	0.65 ± 0.02 (11)	2.7 ± 0.3 (11)	9.9 ± 1.6 (11)	-45.0 ± 0.5 (23)	6.8 ± 0.1 (23)	-86.1 ± 0.5 (23)	4.4 ± 0.1 (23)	6.4 ± 0.3 (21)

The peak Na⁺ current density (I_{Na}), time to peak, and time course of inactivation properties presented were determined from analyses of records obtained on depolarizations to -20 mV (HP=-120 mV). All values are means ± SEM. The number of cells analyzed is provided in parentheses. [#]p<0.05 versus Nav1.5-WT; one-way ANOVA followed by the Dunnett's post-hoc test. *p<0.05, ***p<0.001 versus Nav1.5-WT; Kruskal-Wallis followed by the Dunn's post-hoc test.

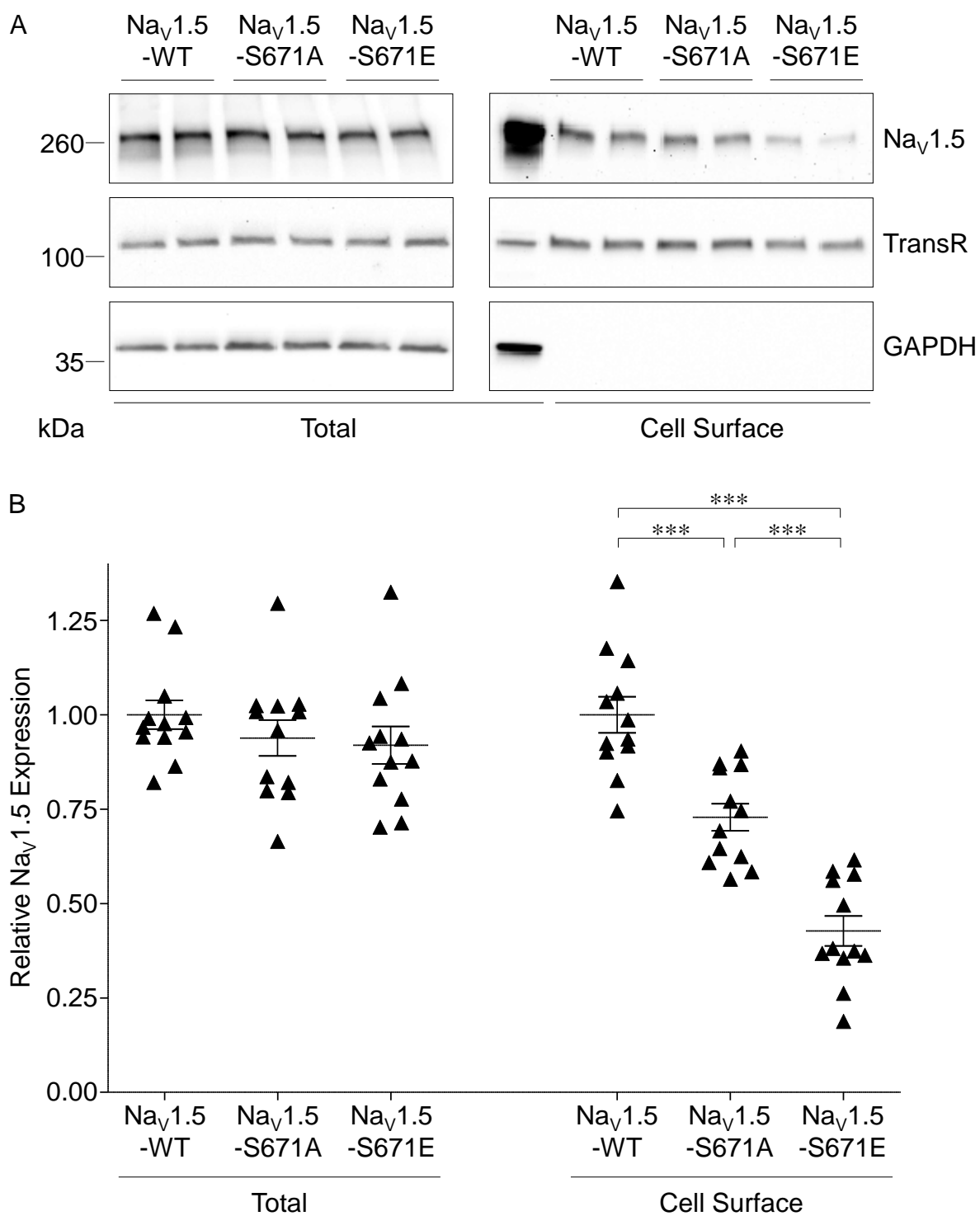


Figure 5.

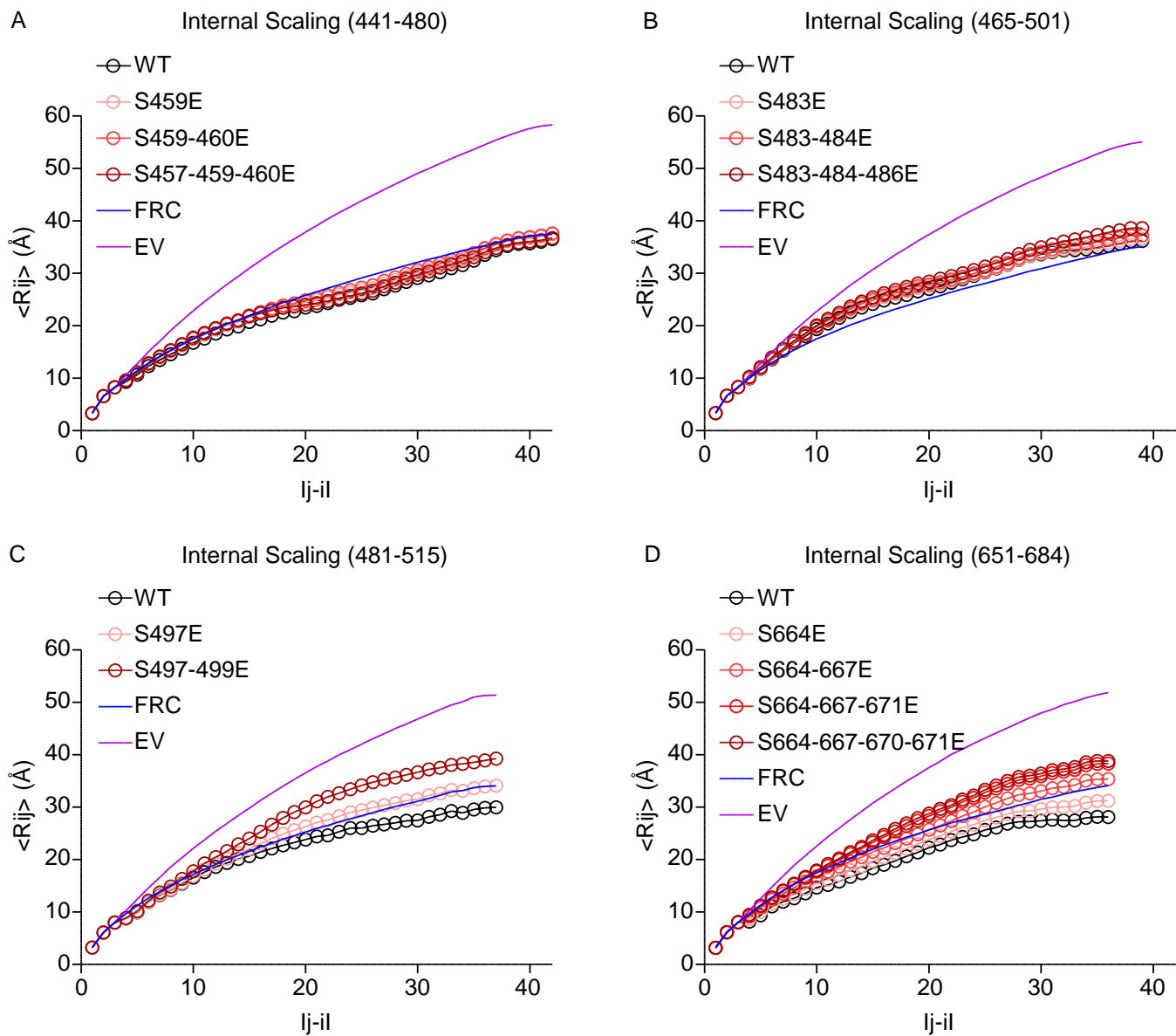


Figure 6.

Scan 6678, m/z=560.2791, z=2, -10lgP=21.64, ppm=0.0 (pS12)

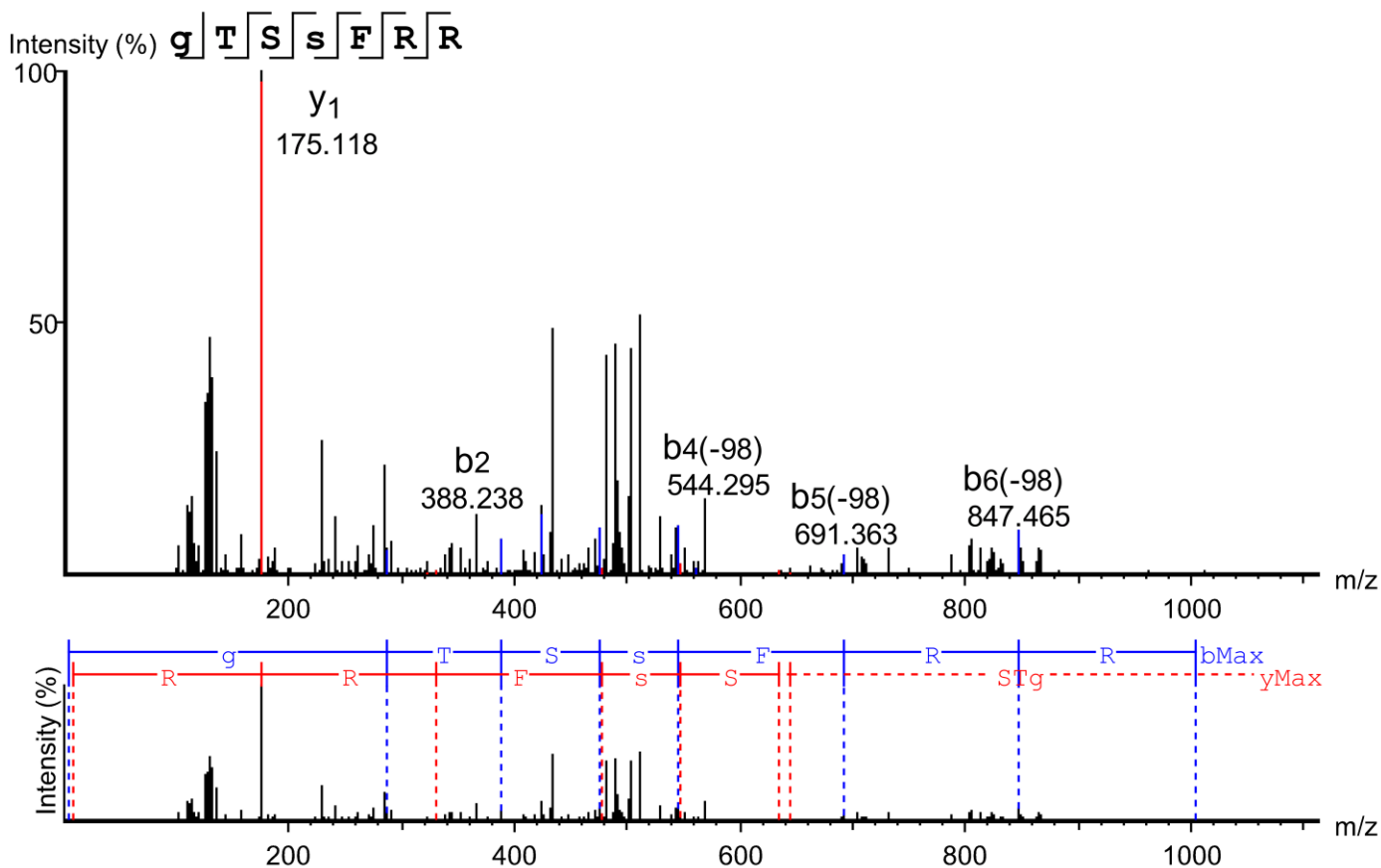


Table 2 - Figure Supplement 1.

Scan 4234, m/z=616.2795, z=2, -10lgP=32.06, ppm=0.1 (pS36)

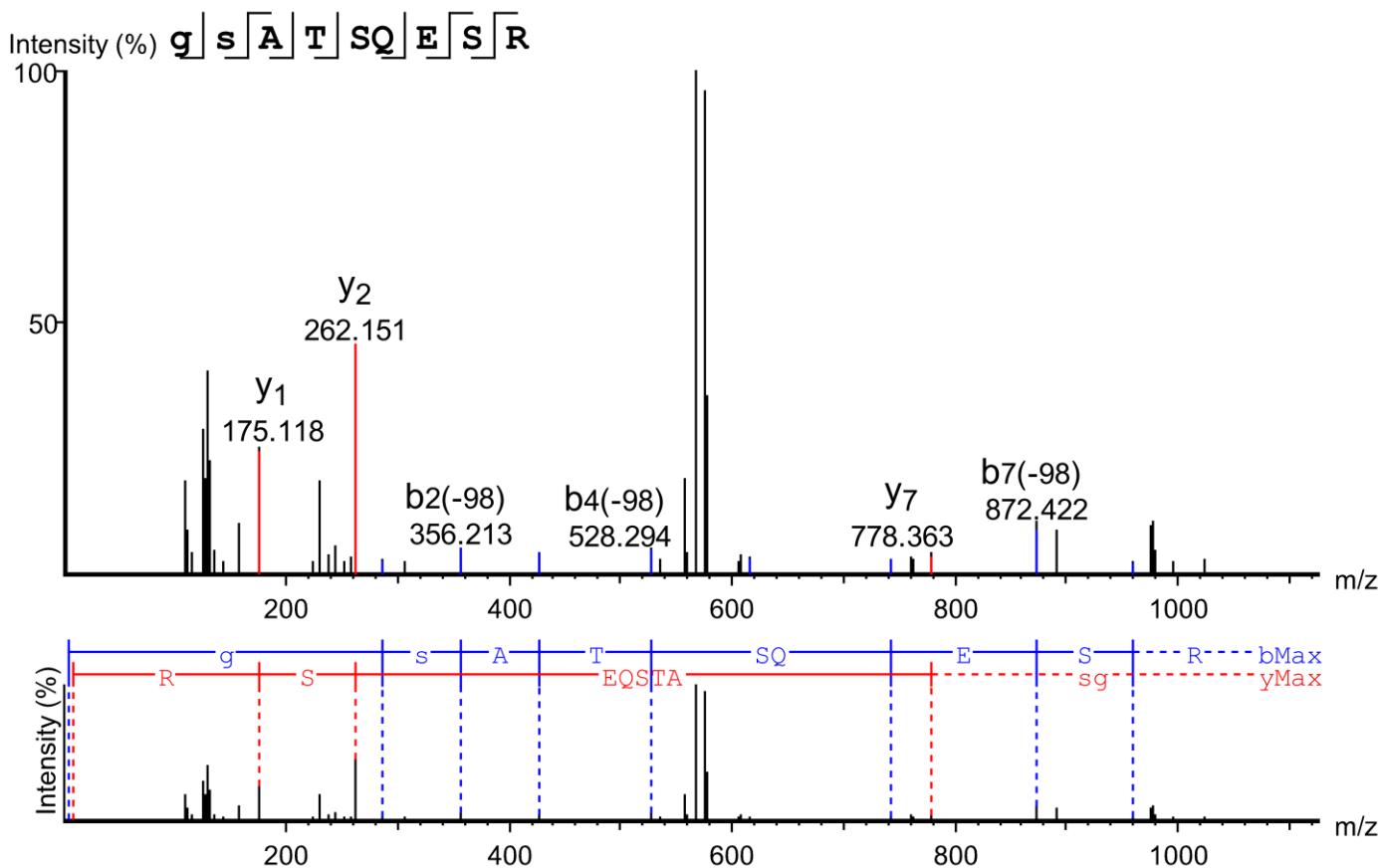


Table 2 - Figure Supplement 1.

Scan 42120, m/z=887.9468, z=4, -10lgP=73.05, ppm=0.6 (pS42)

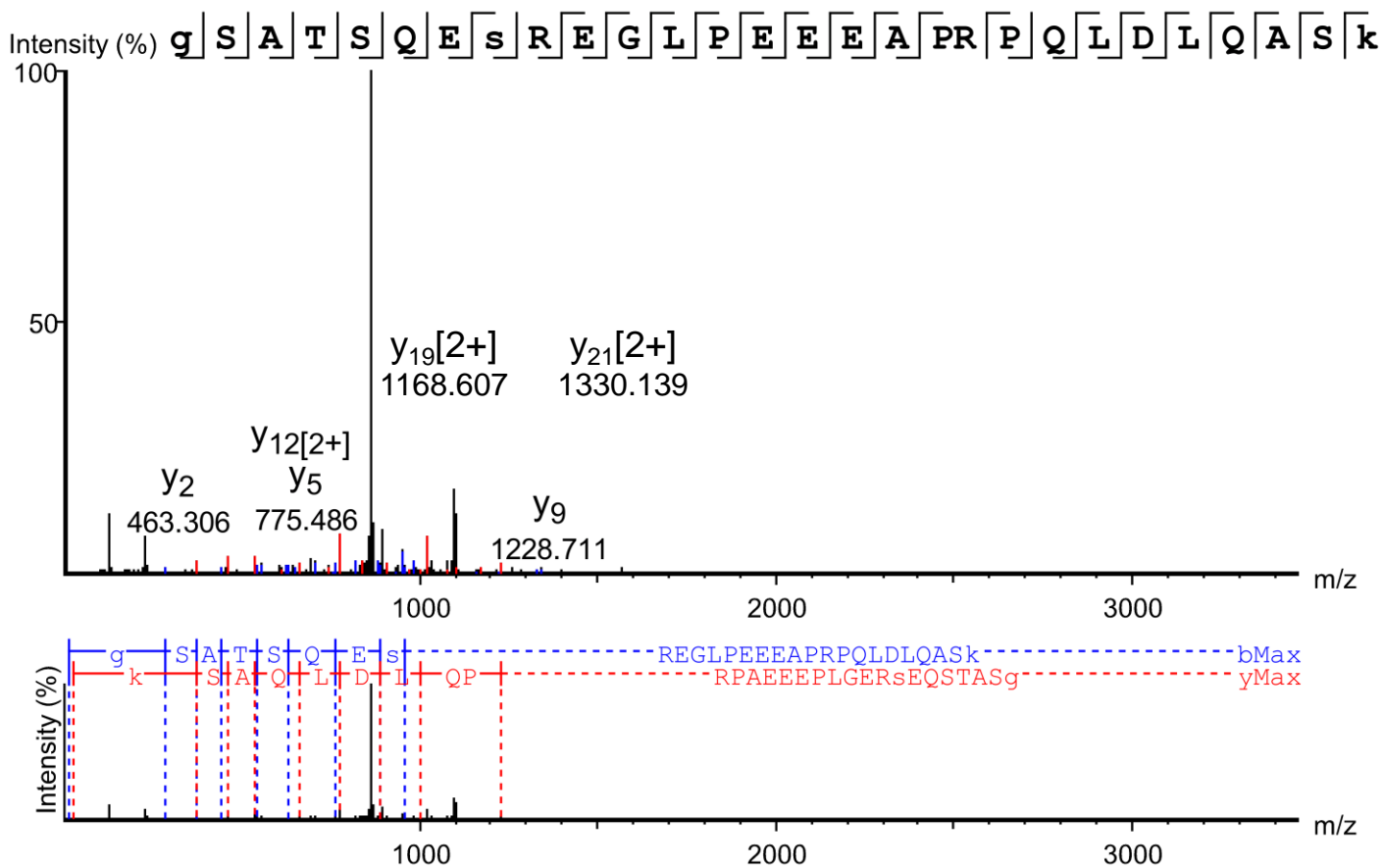


Table 2 - Figure Supplement 1.

Scan 49741, m/z=907.9366, z=4, -10lgP=68.43, ppm=-1.4 (pS39 + pS42)

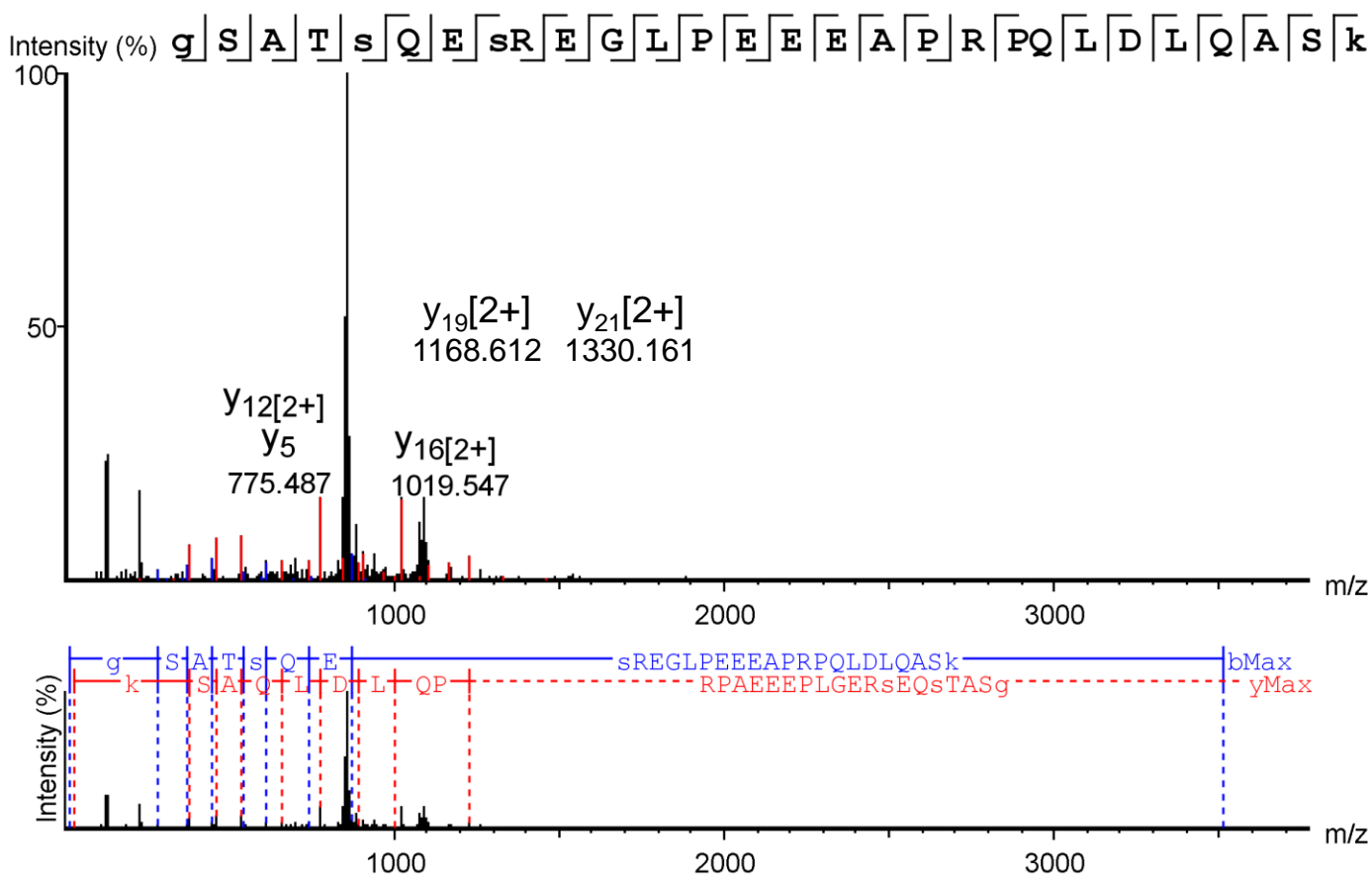


Table 2 - Figure Supplement 1.

Scan 51767, m/z=957.7820, z=3, -10lgP=77.13, ppm=0.1 - pS457 (+ pS459 or pS460)

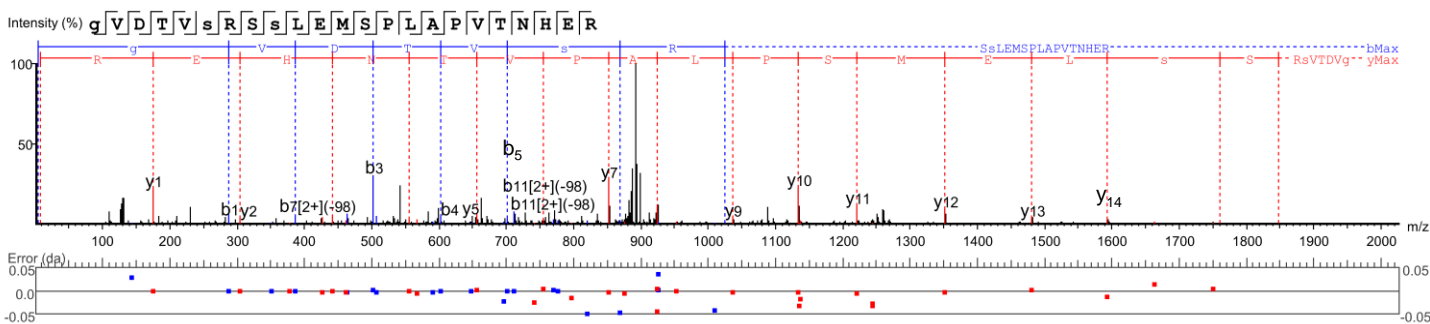


Table 2 - Figure Supplement 1.

Scan 52470, m/z=958.1167, z=3, -10lgP=41.49, ppm=7.1 (pS459 + pS460)

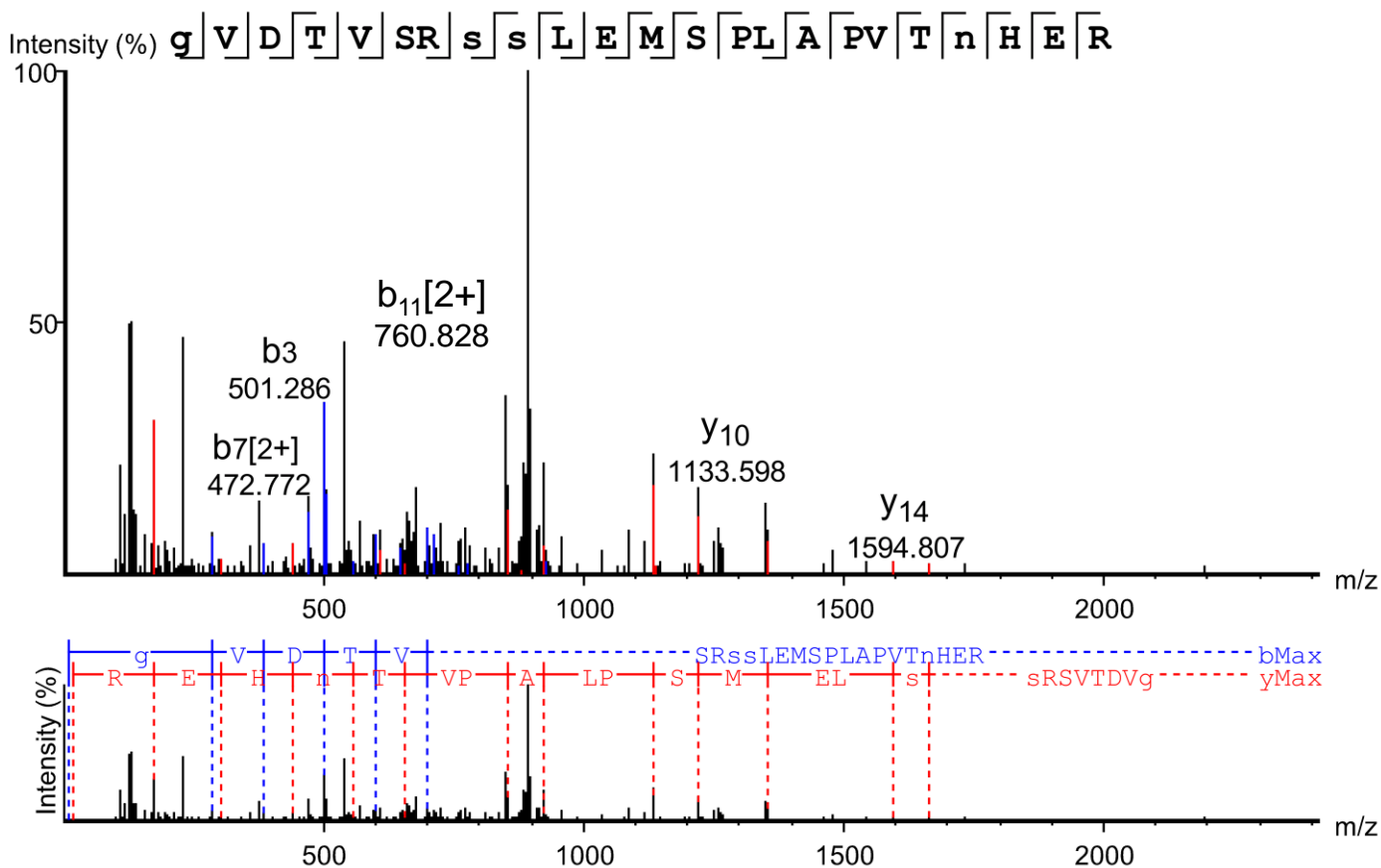


Table 2 - Figure Supplement 1.

Scan 46779, m/z=1039.0032, z=2, -10lgP=61.17, ppm=0.2 (pS460)

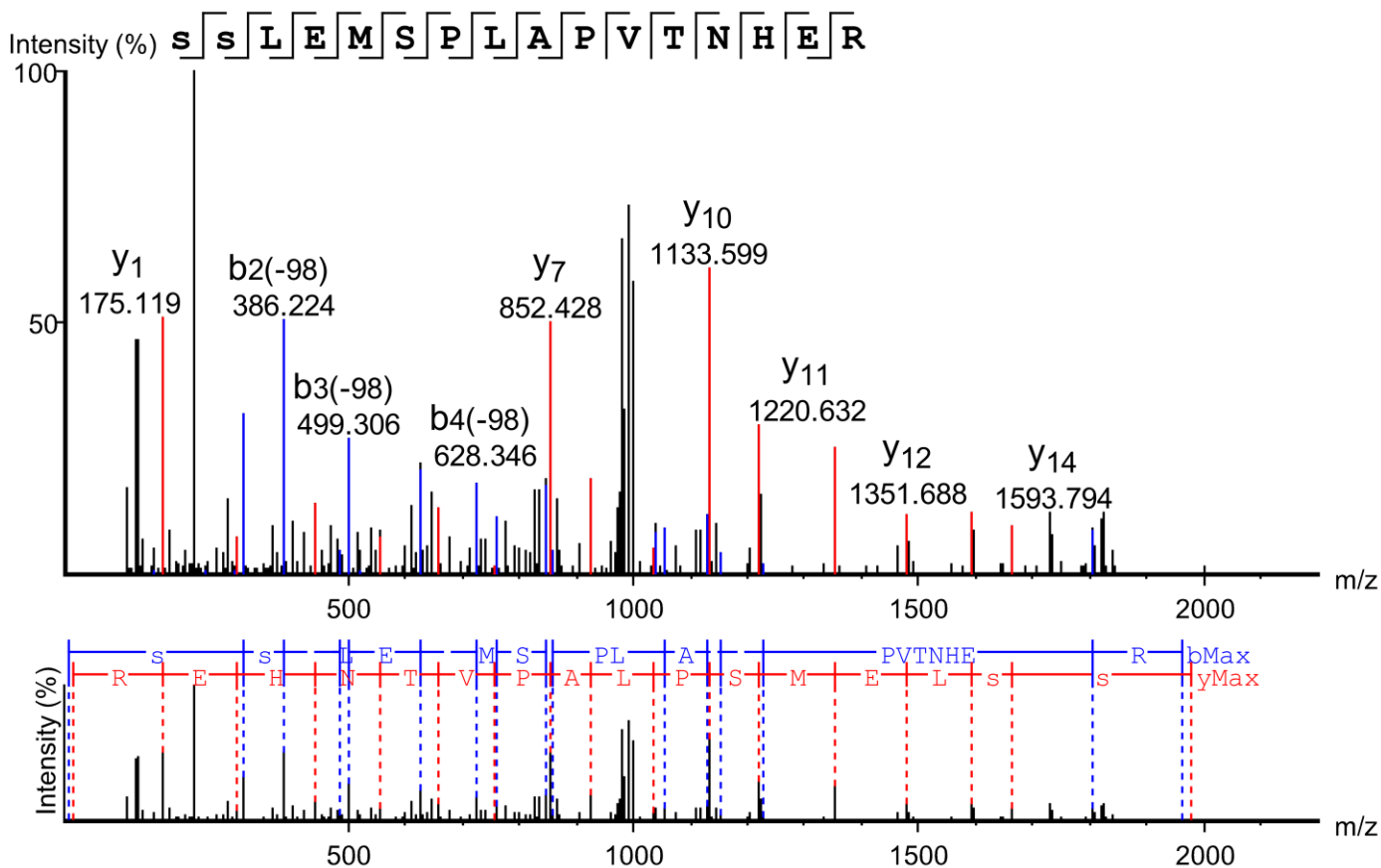


Table 2 - Figure Supplement 1.

Scan 26433, m/z=561.0378, z=4, -10lgP=52.36, ppm=0.7 (pS483)

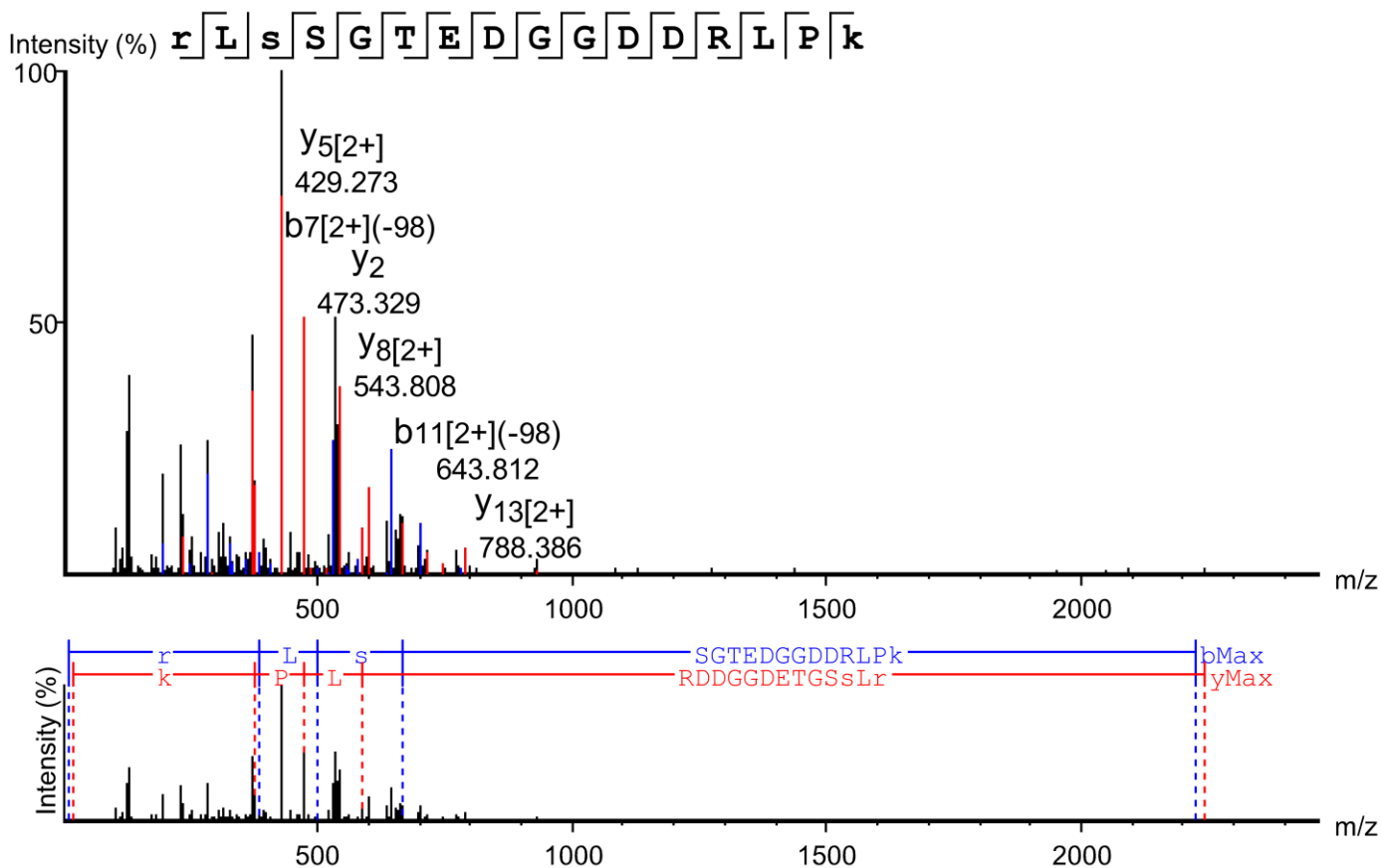


Table 2 - Figure Supplement 1.

Scan 22284, m/z=759.3195, z=2, -10lgP=45.74, ppm=0.0 (pS484)

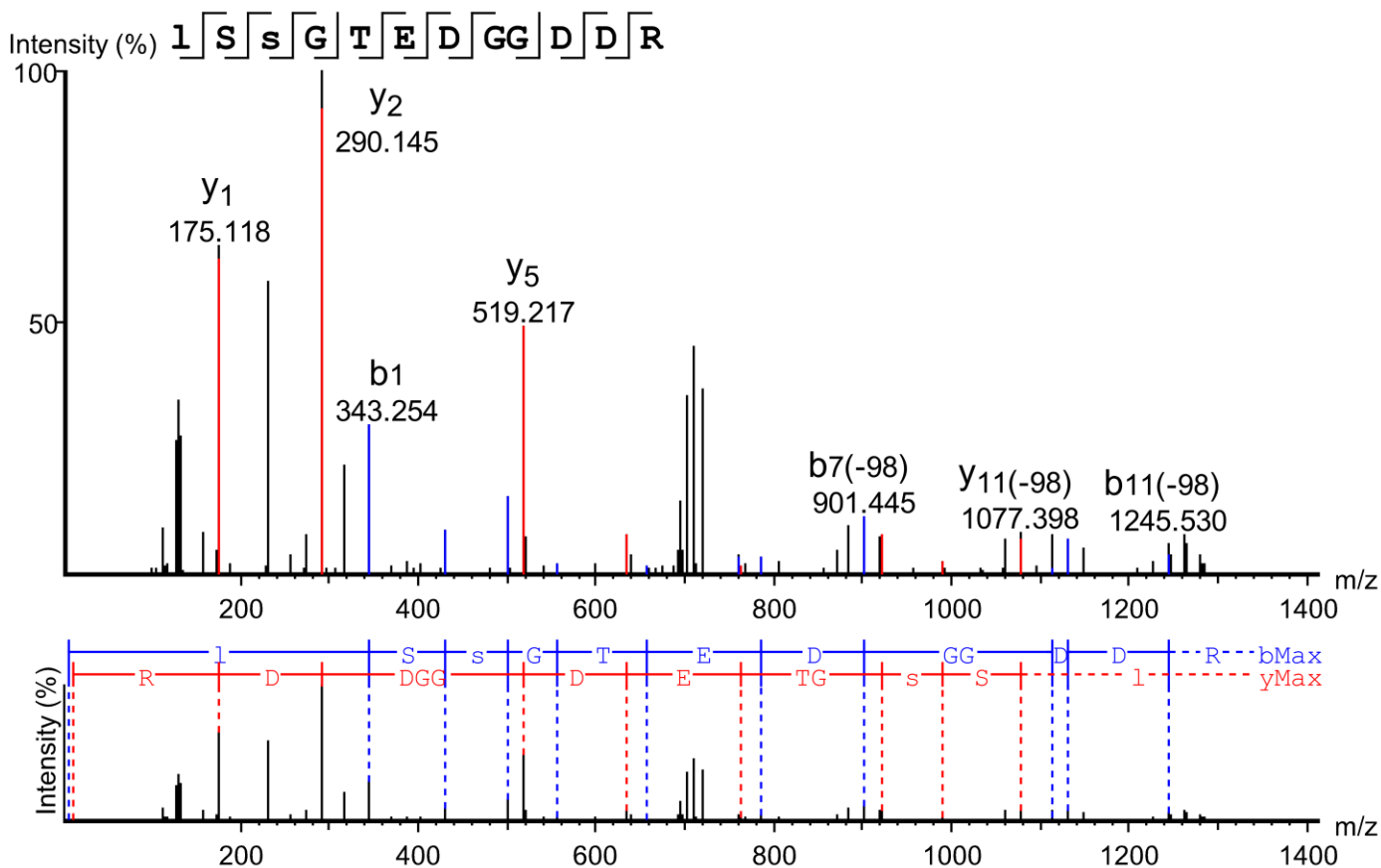


Table 2 - Figure Supplement 1.

Scan 26141, m/z=628.9735, z=3, -10lgP=21.92, ppm=-2.3 (pT486)

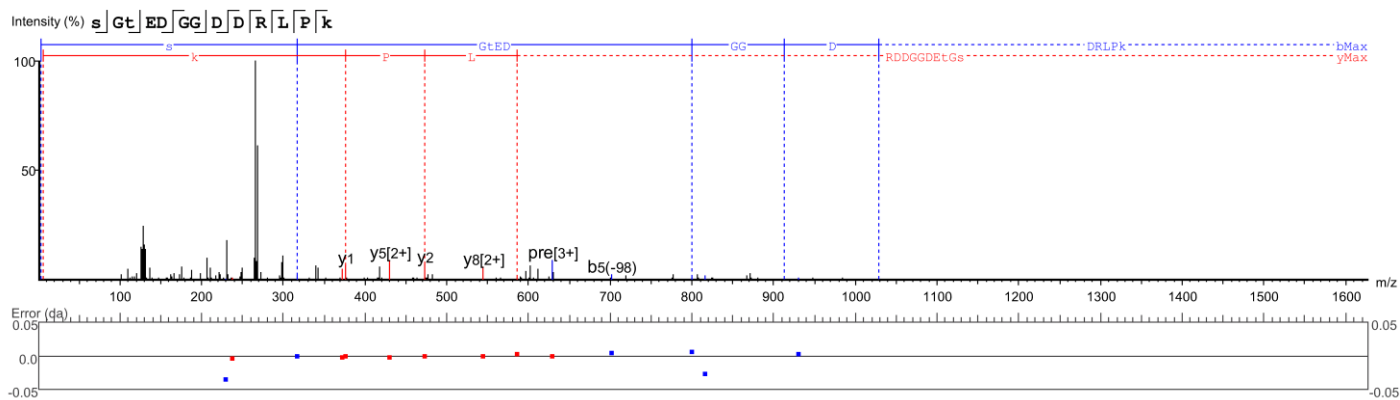


Table 2 - Figure Supplement 1.

Scan 29037, m/z=536.4764, z=5, -10lgP=62.95, ppm=0.5 (pS483 + pS484)

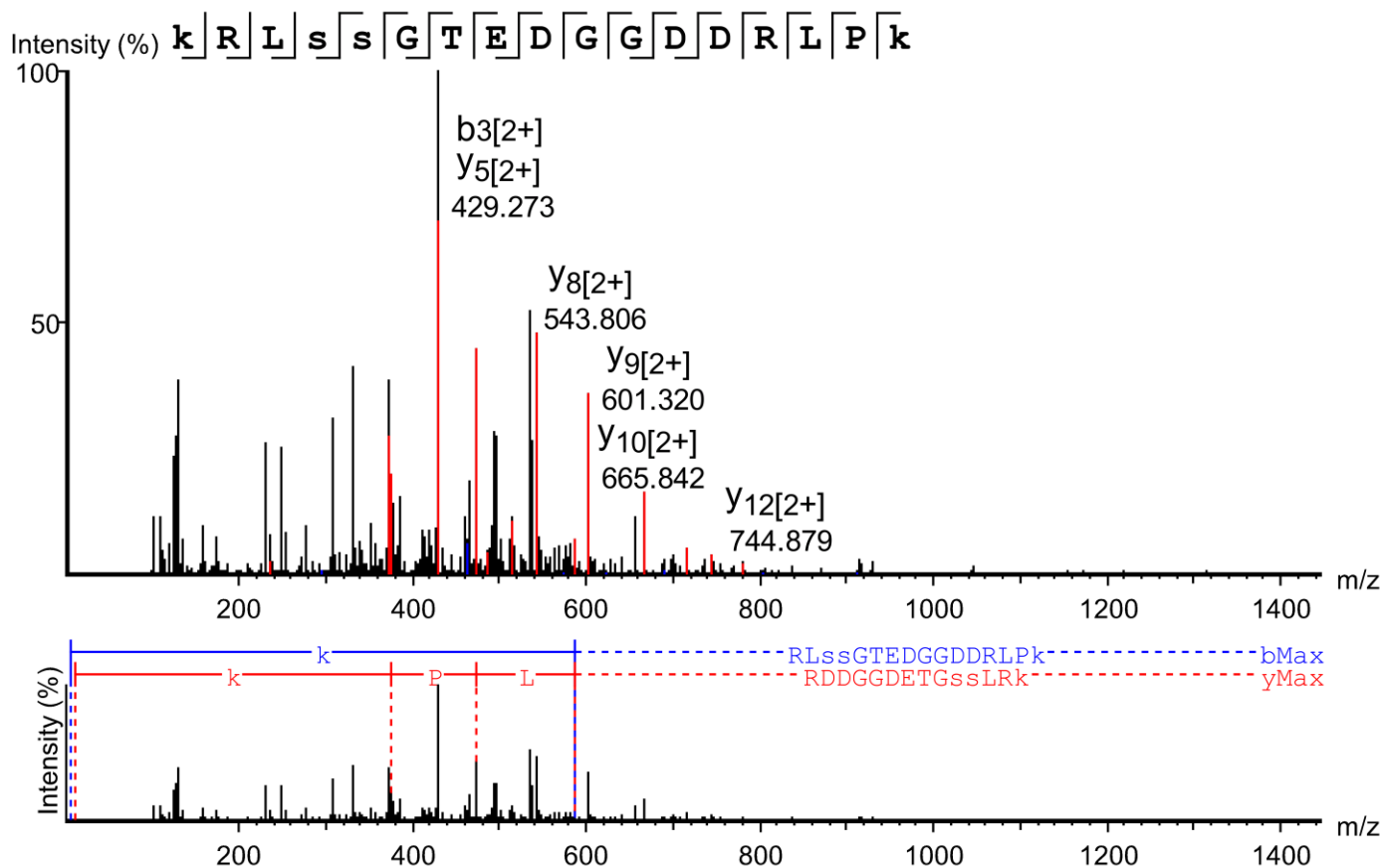


Table 2 - Figure Supplement 1.

Scan 29957, m/z=732.8451, z=4, -10lgP=60.24, ppm=-1.3 (pS497)

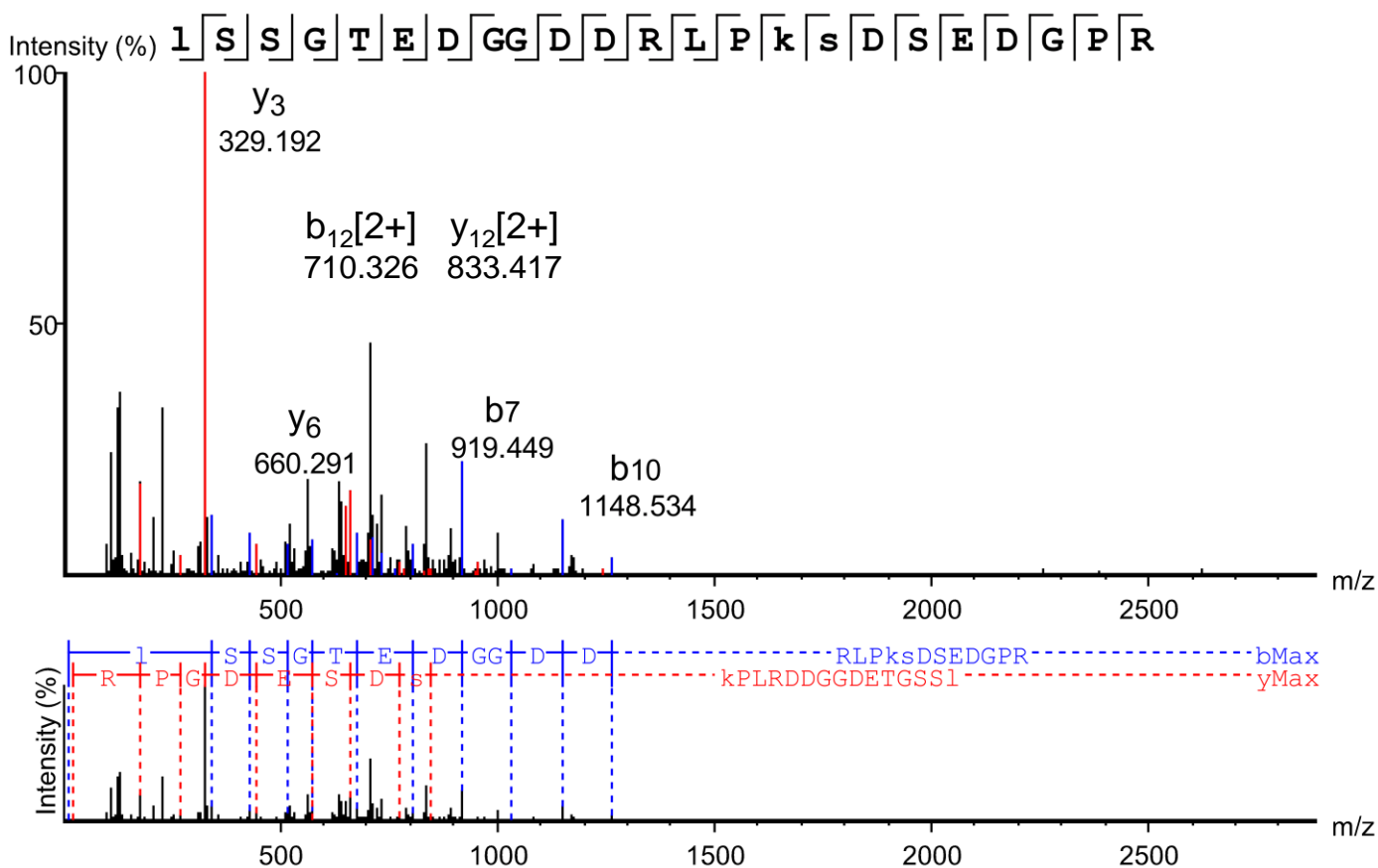


Table 2 - Figure Supplement 1.

Scan 27780, m/z=791.8616, z=4, -10lgP=40.10, ppm=-1.6 (pS483 + pS497)

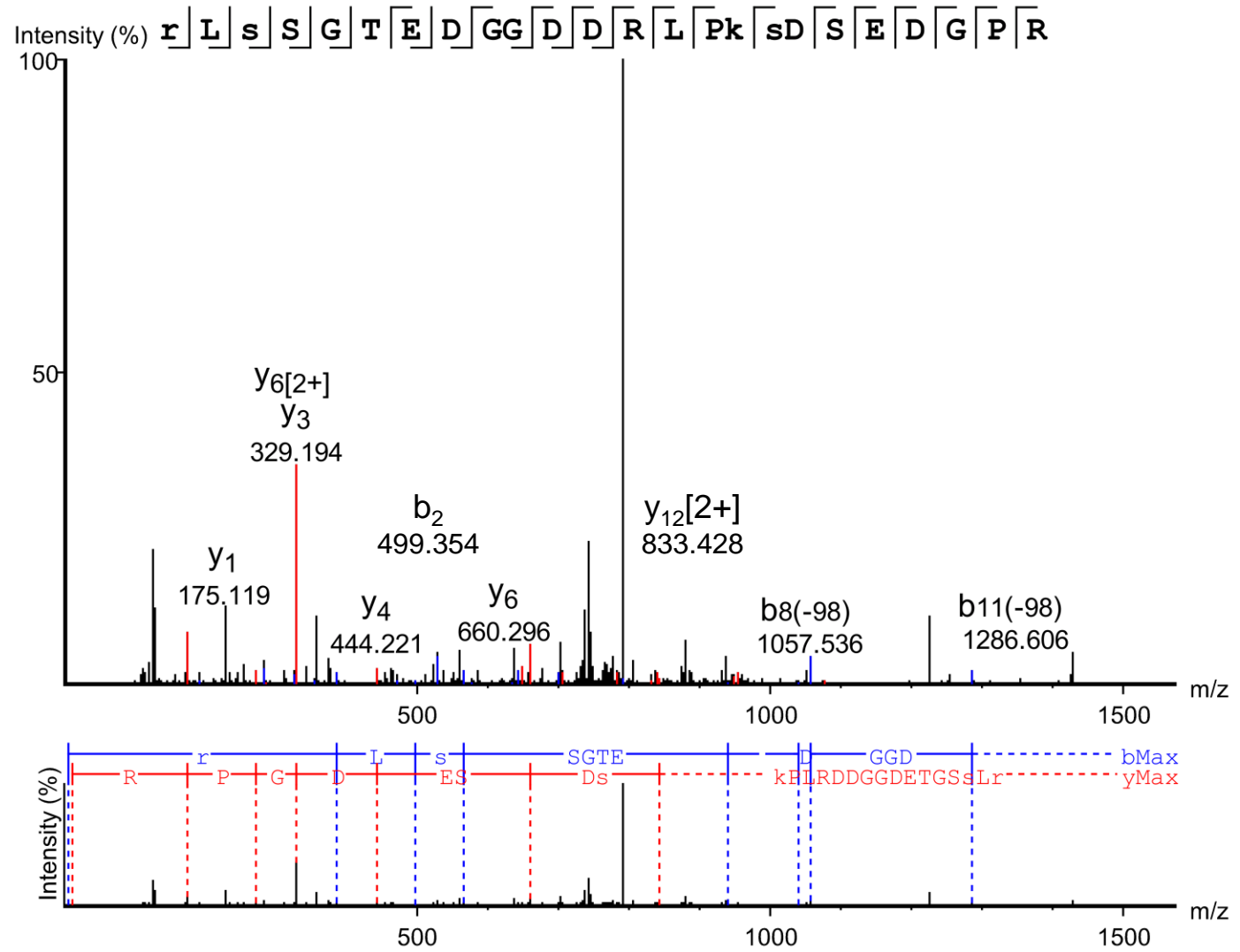


Table 2 - Figure Supplement 1.

Scan 36168, m/z=1003.4476, z=3, -10lgP=54.82, ppm=-0.1 (pS484 + pS497)

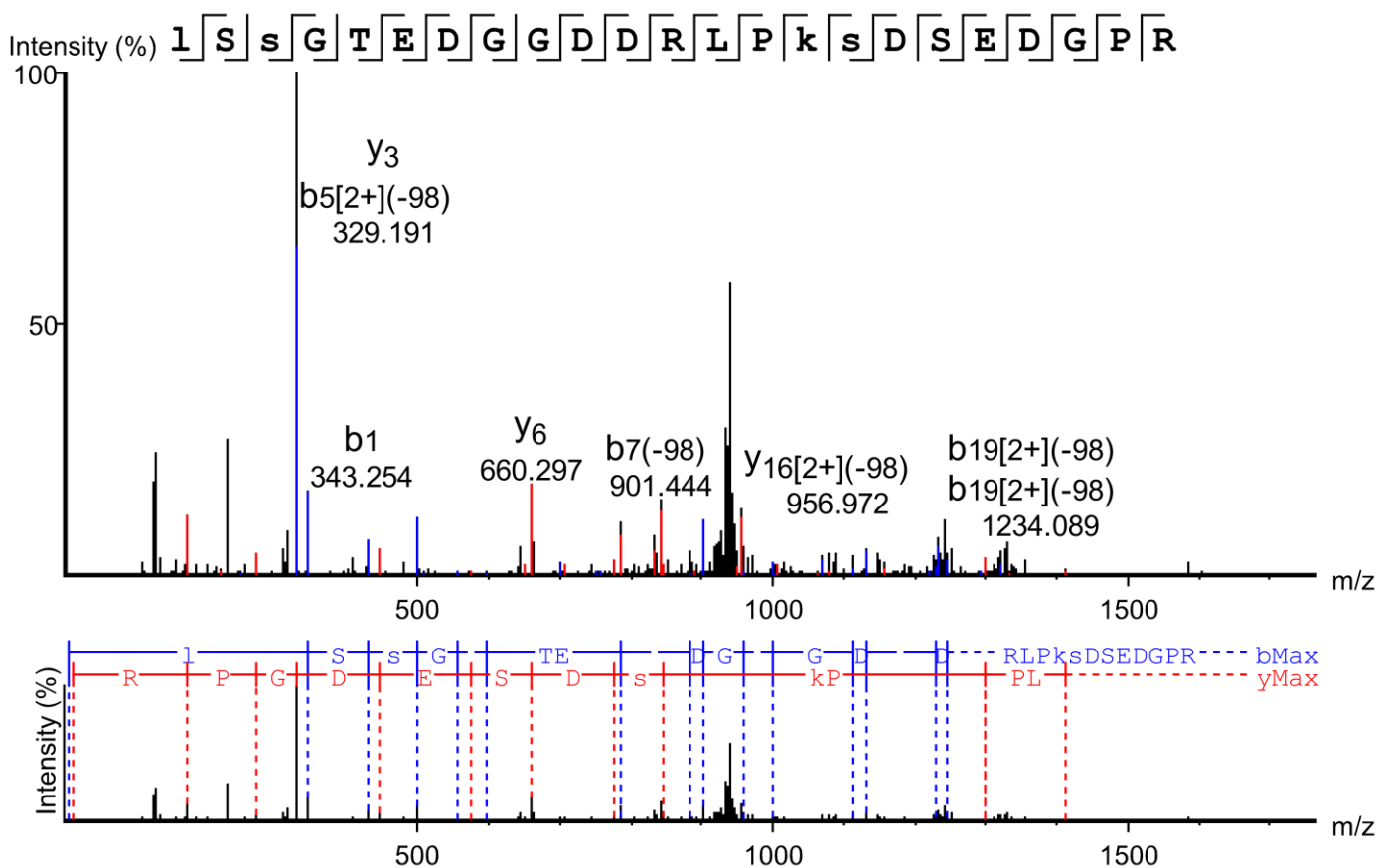


Table 2 - Figure Supplement 1.

Scan 7929, m/z=586.2448, z=2, -10lgP=41.97, ppm=-0.5 (pS499)

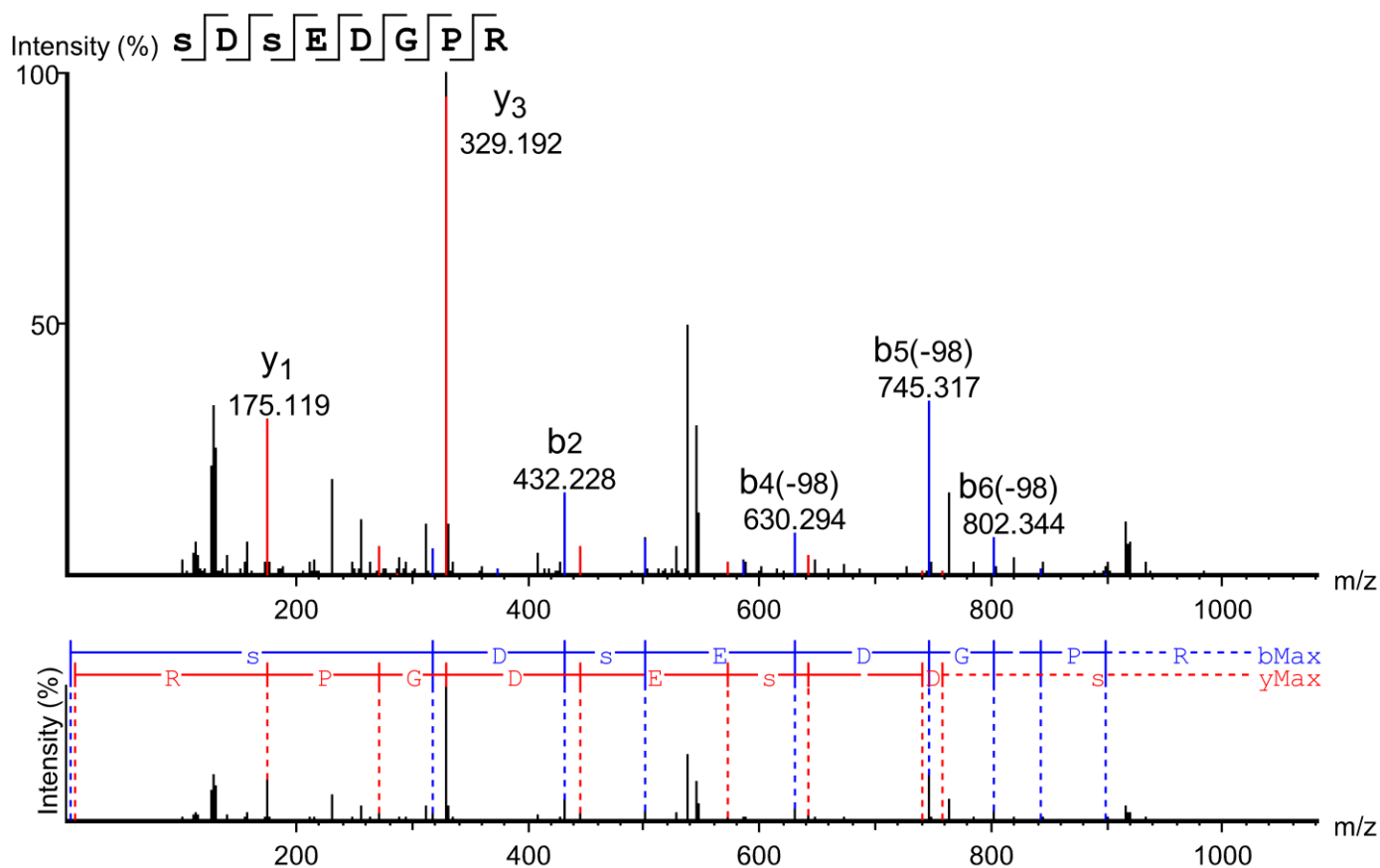


Table 2 - Figure Supplement 1.

Scan 46112, m/z=573.6431, z=3, -10lgP=51.77, ppm=-0.2 (pS510)

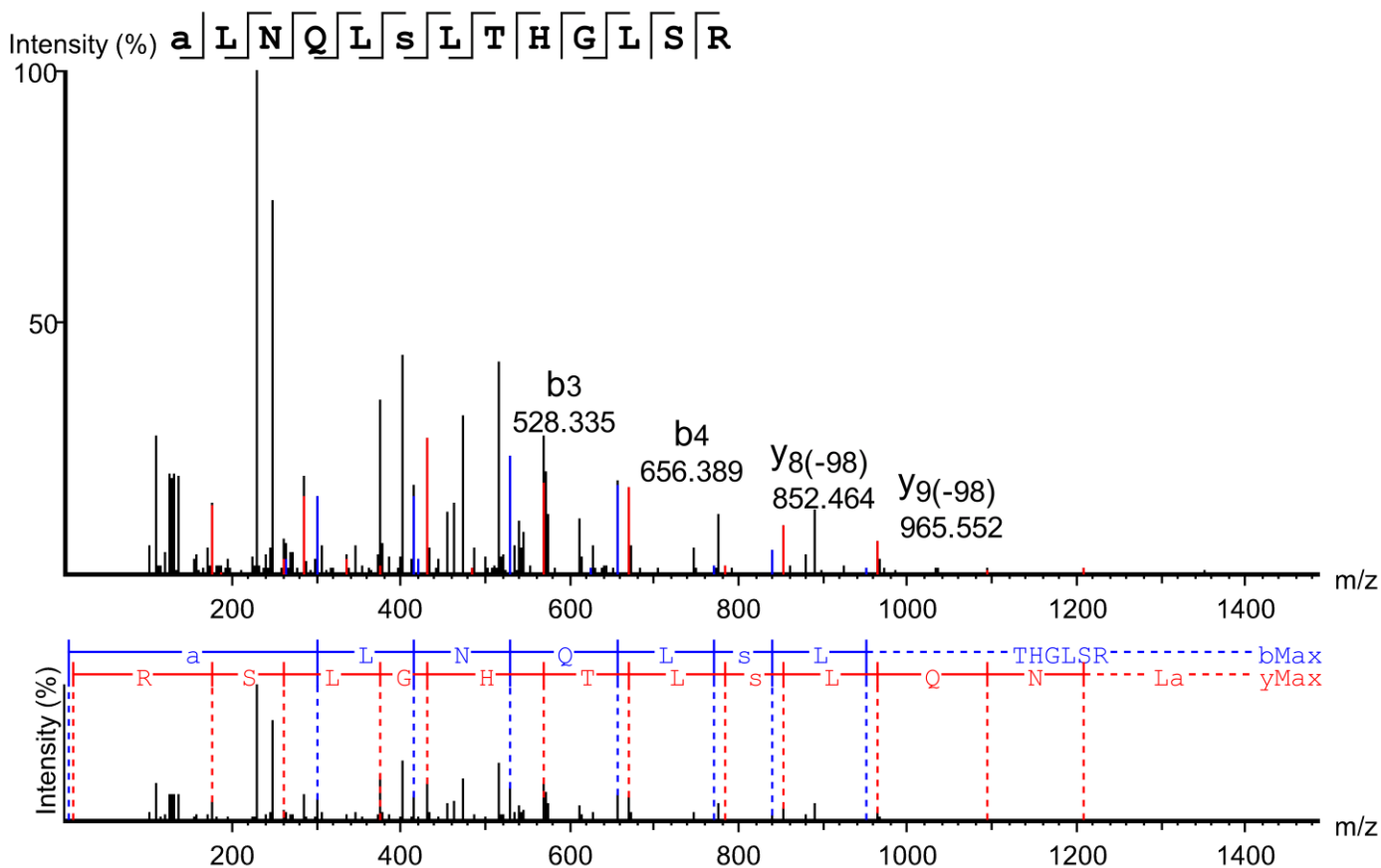


Table 2 - Figure Supplement 1.

Scan 45136, m/z=573.6437, z=3, -10lgP=46.66, ppm=0.7 (pS516)

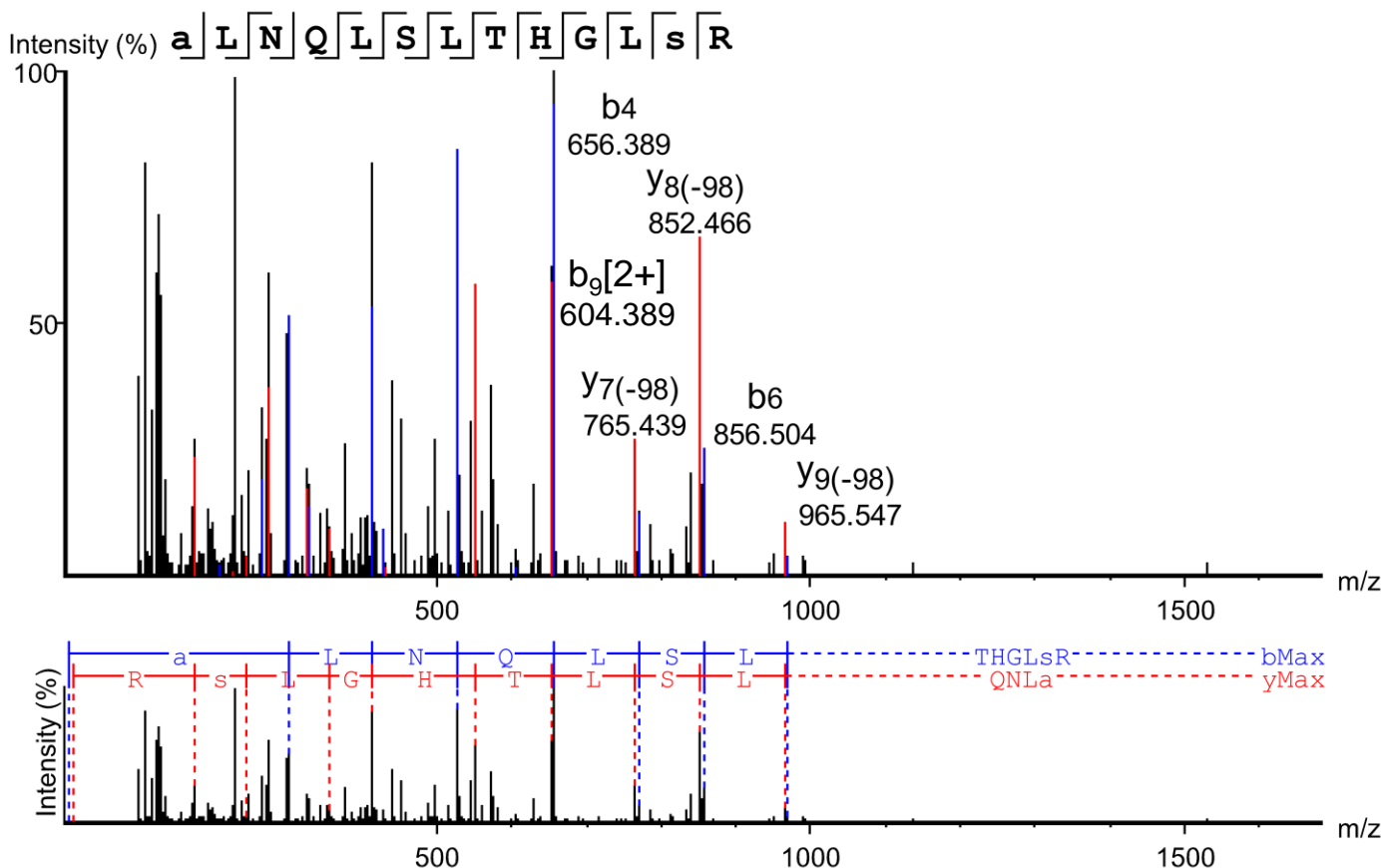


Table 2 - Figure Supplement 1.

Scan 38518, m/z=489.5841, z=3, -10lgP=40.74, ppm=1.7 (pS525)

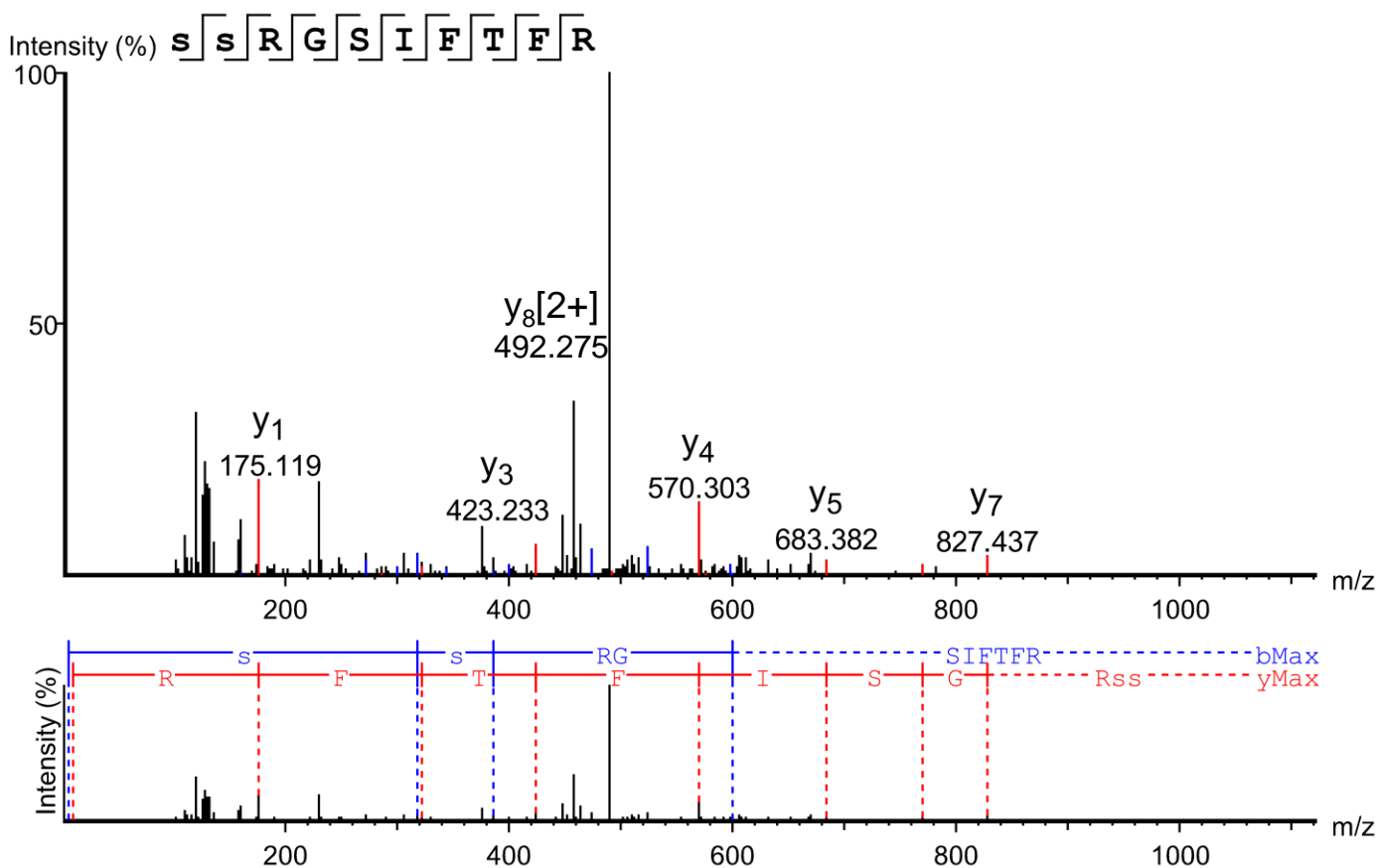


Table 2 - Figure Supplement 1.

Scan 25979, m/z=921.7010, z=3, -10lgP=70.93, ppm=1.2 (pS539)

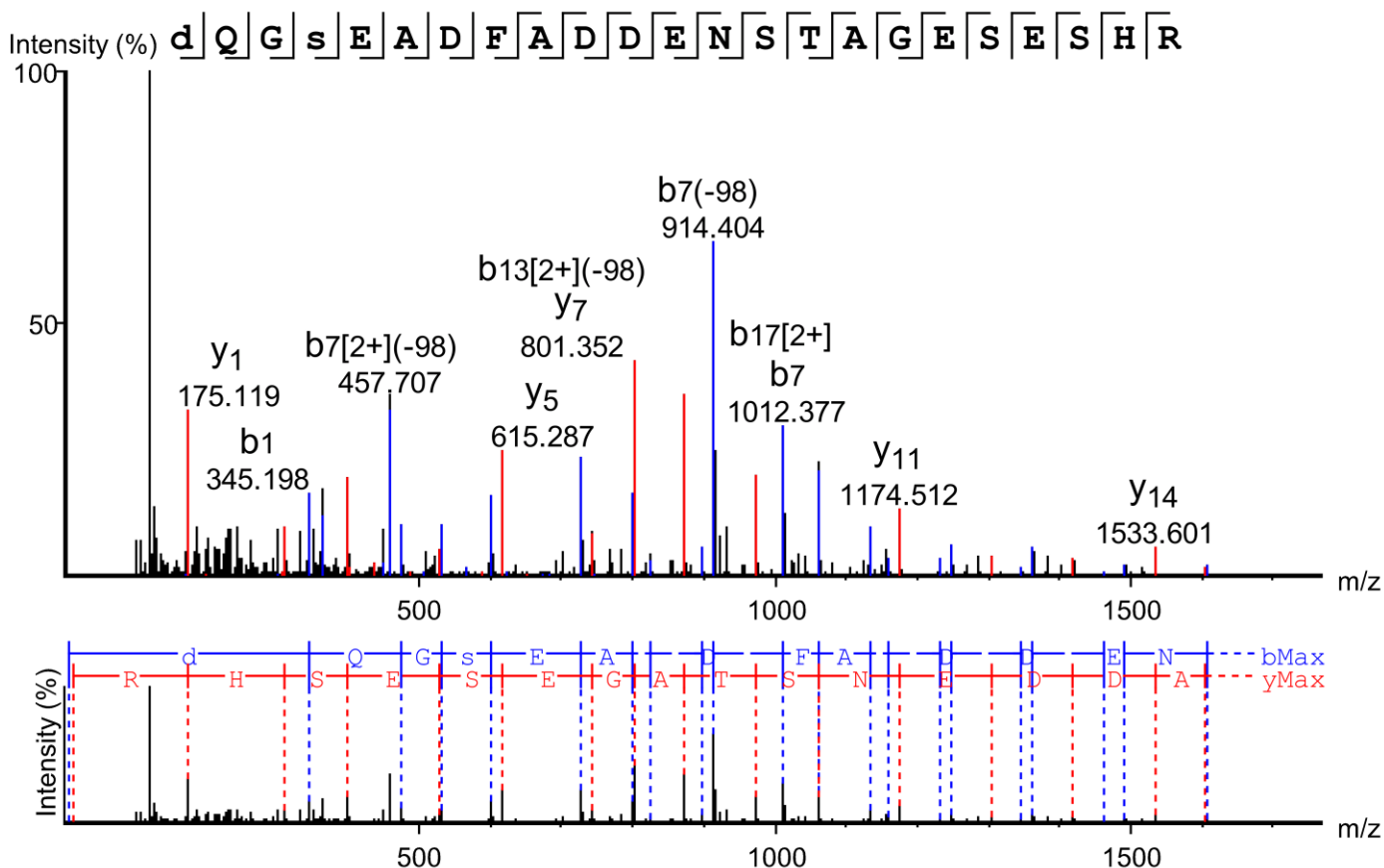


Table 2 - Figure Supplement 1.

Scan 13172, m/z=769.5792, z=4, -10lgP=55.34, ppm=2.5 (pS549)

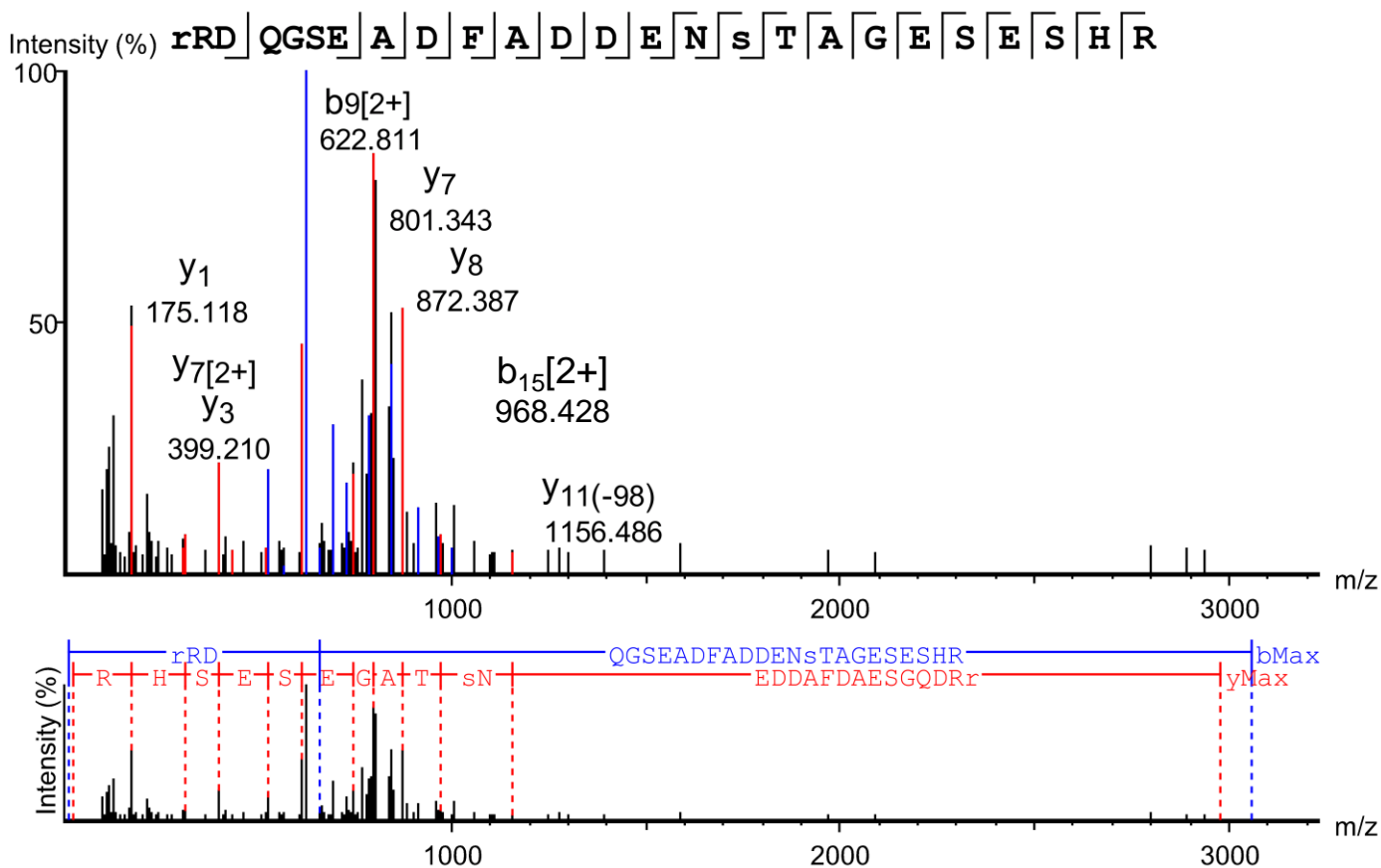


Table 2 - Figure Supplement 1.

Scan 91146, m/z=745.9208, z=2, -10lgP=30.17, ppm=0.6 (pS560)

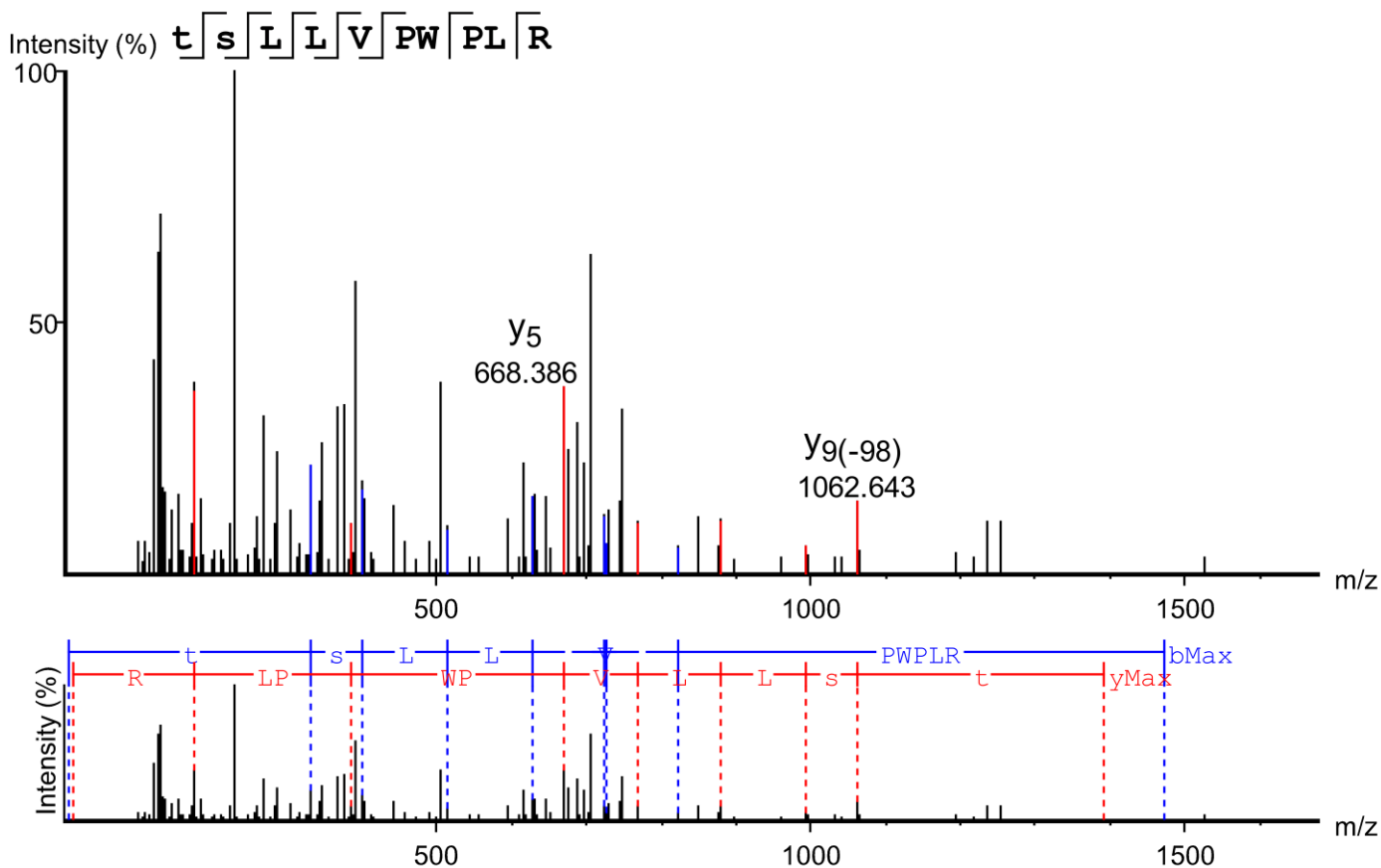


Table 2 - Figure Supplement 1.

Scan 35559, m/z=911.4655, z=3, -10lgP=55.17, ppm=-3.7 (pS571)

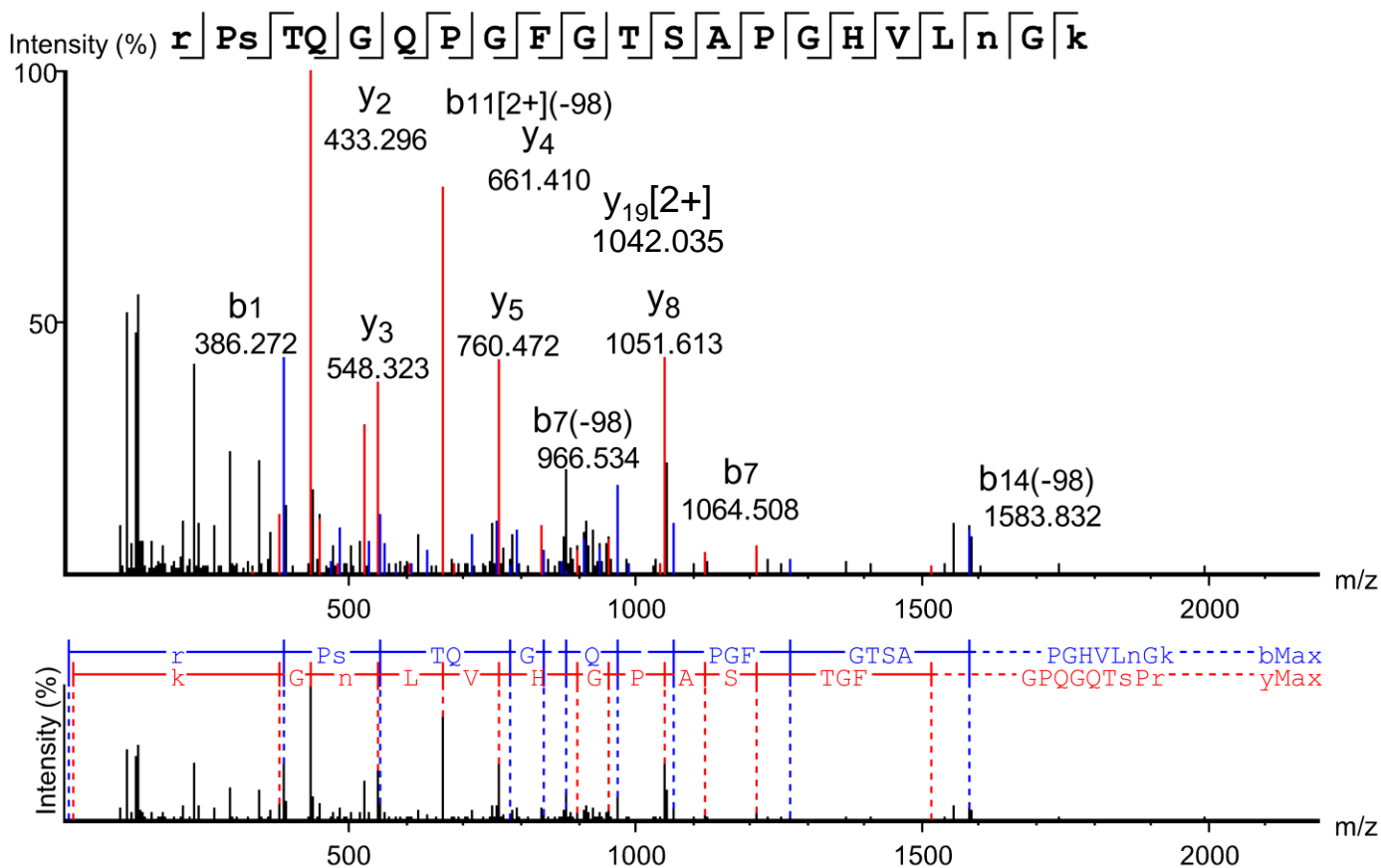


Table 2 - Figure Supplement 1.

Scan 36455, m/z=683.8556, z=4, -10lgP=48.45, ppm=3.1 (pS581)

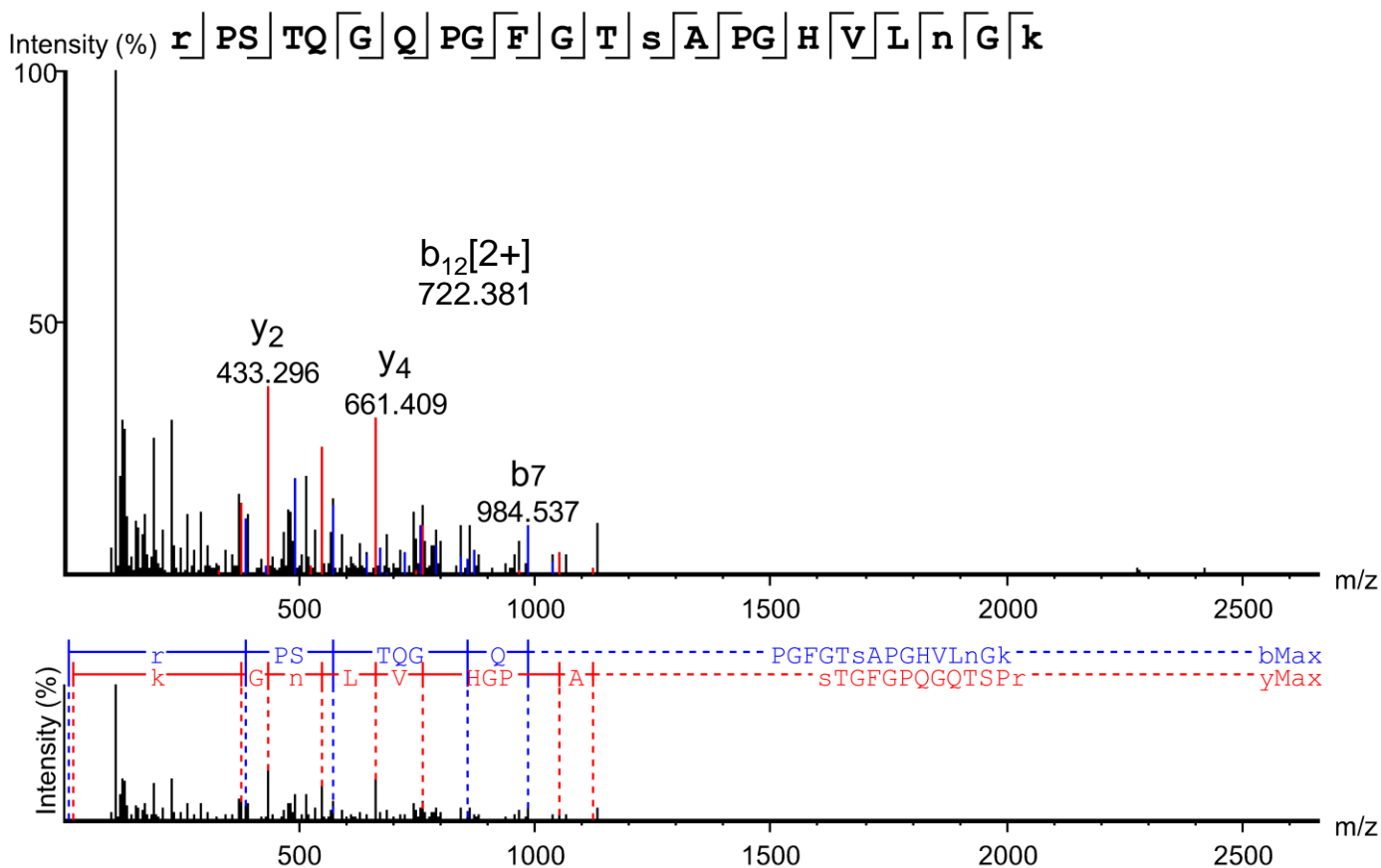


Table 2 - Figure Supplement 1.

Scan 59637, m/z=841.6600, z=4, -10lgP=71.71, ppm=-0.6 (pS593)

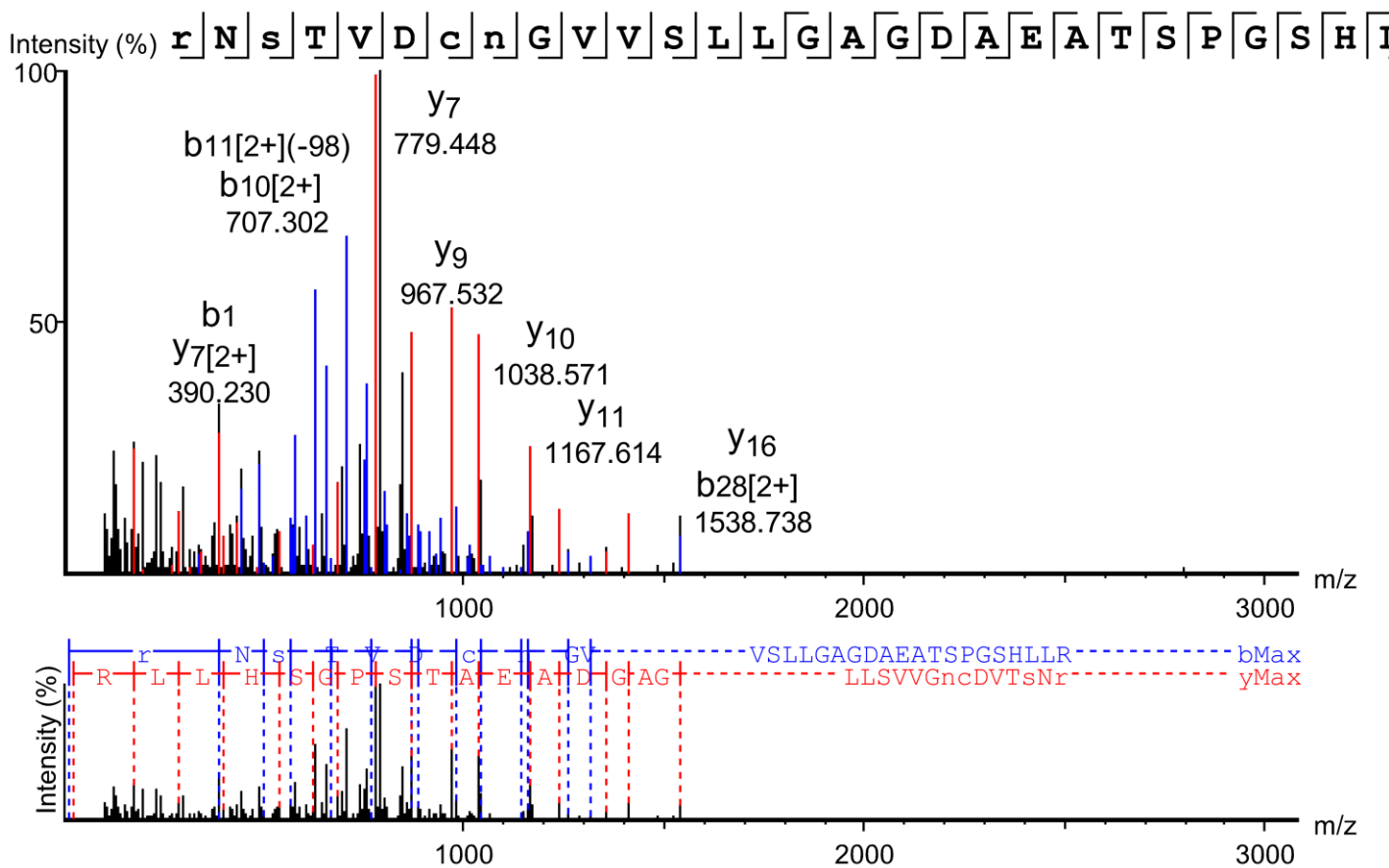


Table 2 - Figure Supplement 1.

Scan 91558, m/z=936.5065, z=3, -10lgP=60.59, ppm=3.3 (pS664)

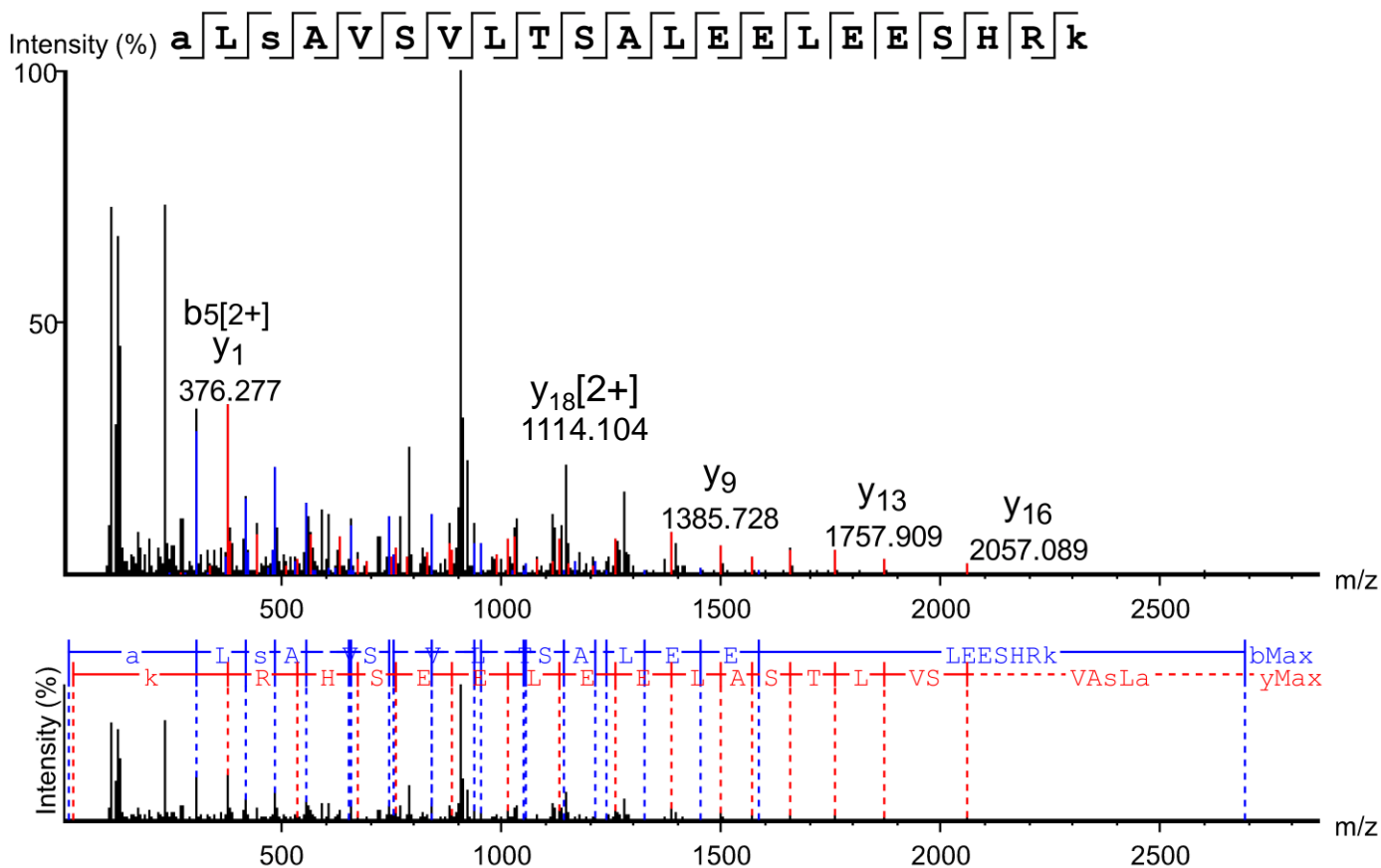


Table 2 - Figure Supplement 1.

Scan 97561, m/z=817.4163, z=3, -10lgP=64.07, ppm=-1.4 (pS667)

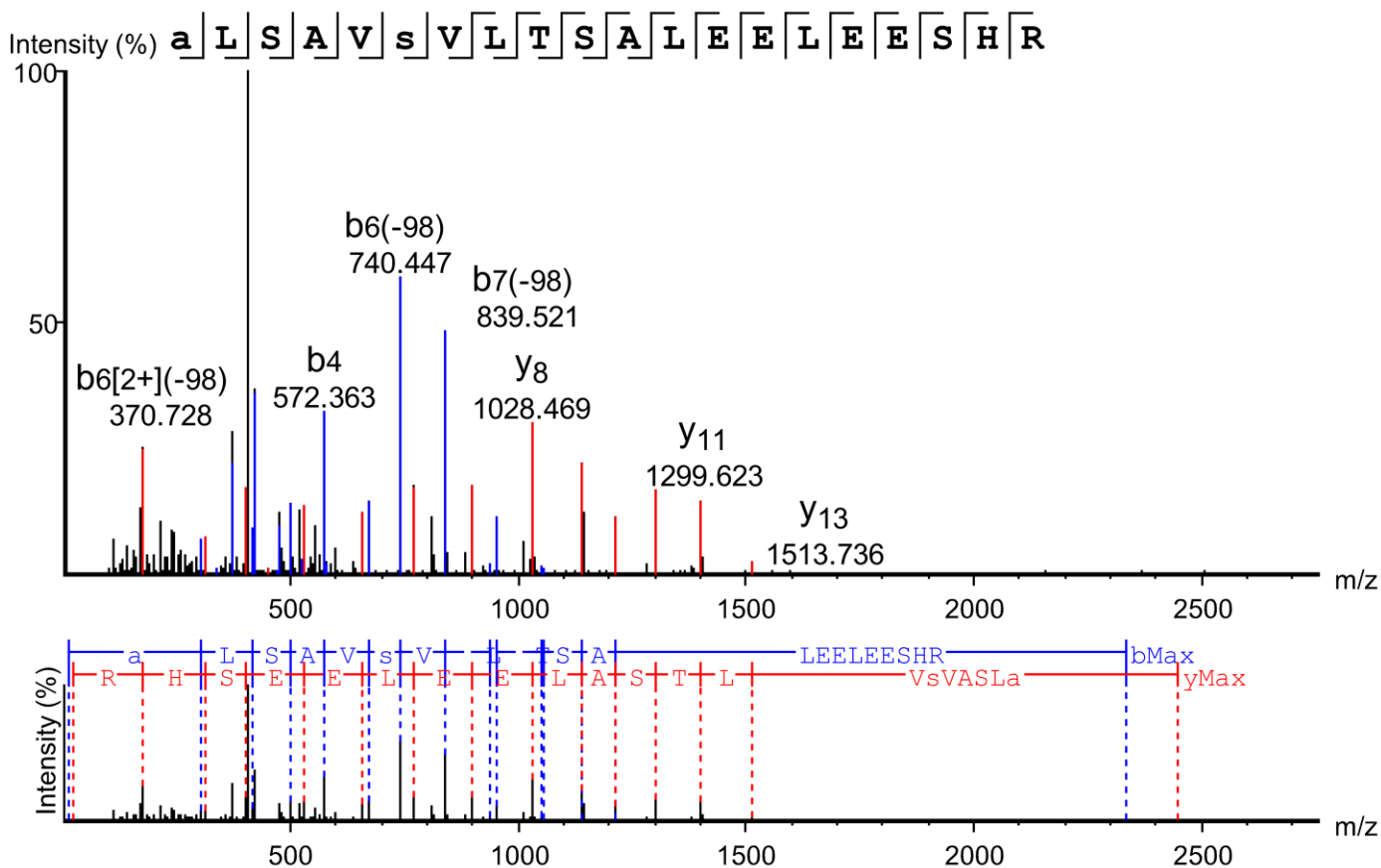


Table 2 - Figure Supplement 1.

Scan 85466, m/z=702.6287, z=4, -10lgP=54.31, ppm=-1.0 (pT670)

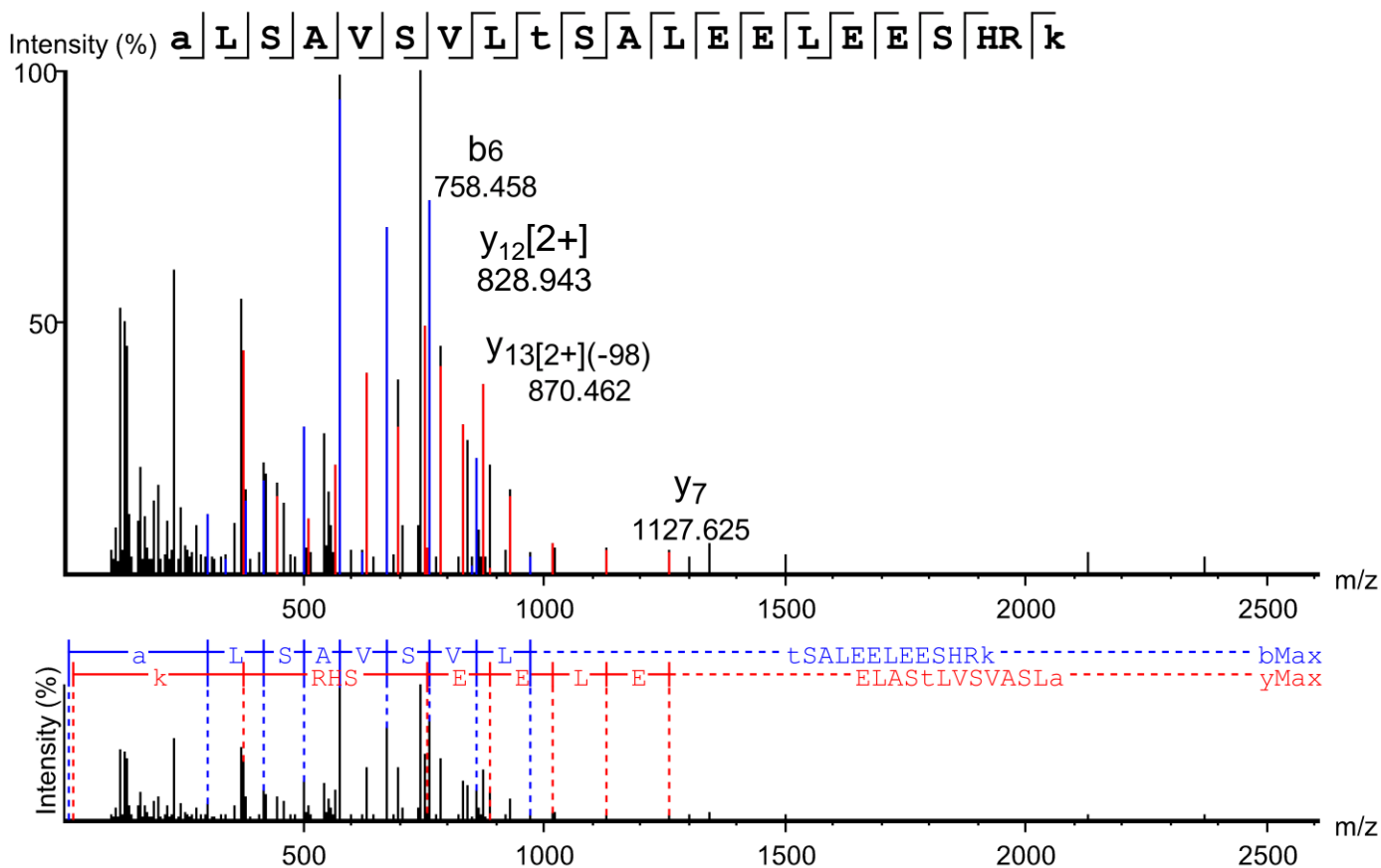


Table 2 - Figure Supplement 1.

Scan 88006, m/z=702.6296, z=4, -10lgP=63.19, ppm=0.3 (pS671)

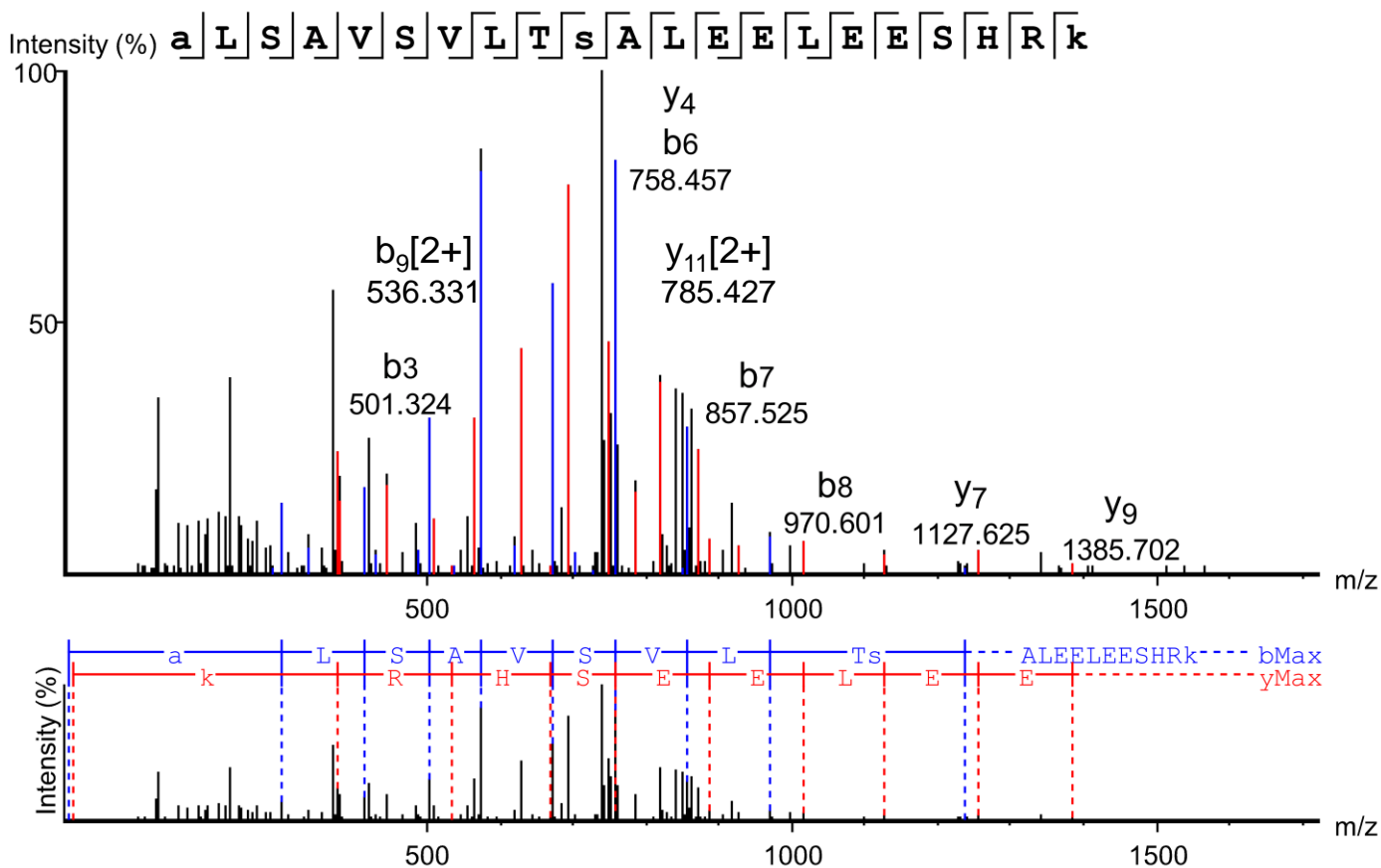


Table 2 - Figure Supplement 1.

Scan 93723, m/z=886.7712, z=3, -10lgP=58.77, ppm=0.1 (pS664 + pS667)

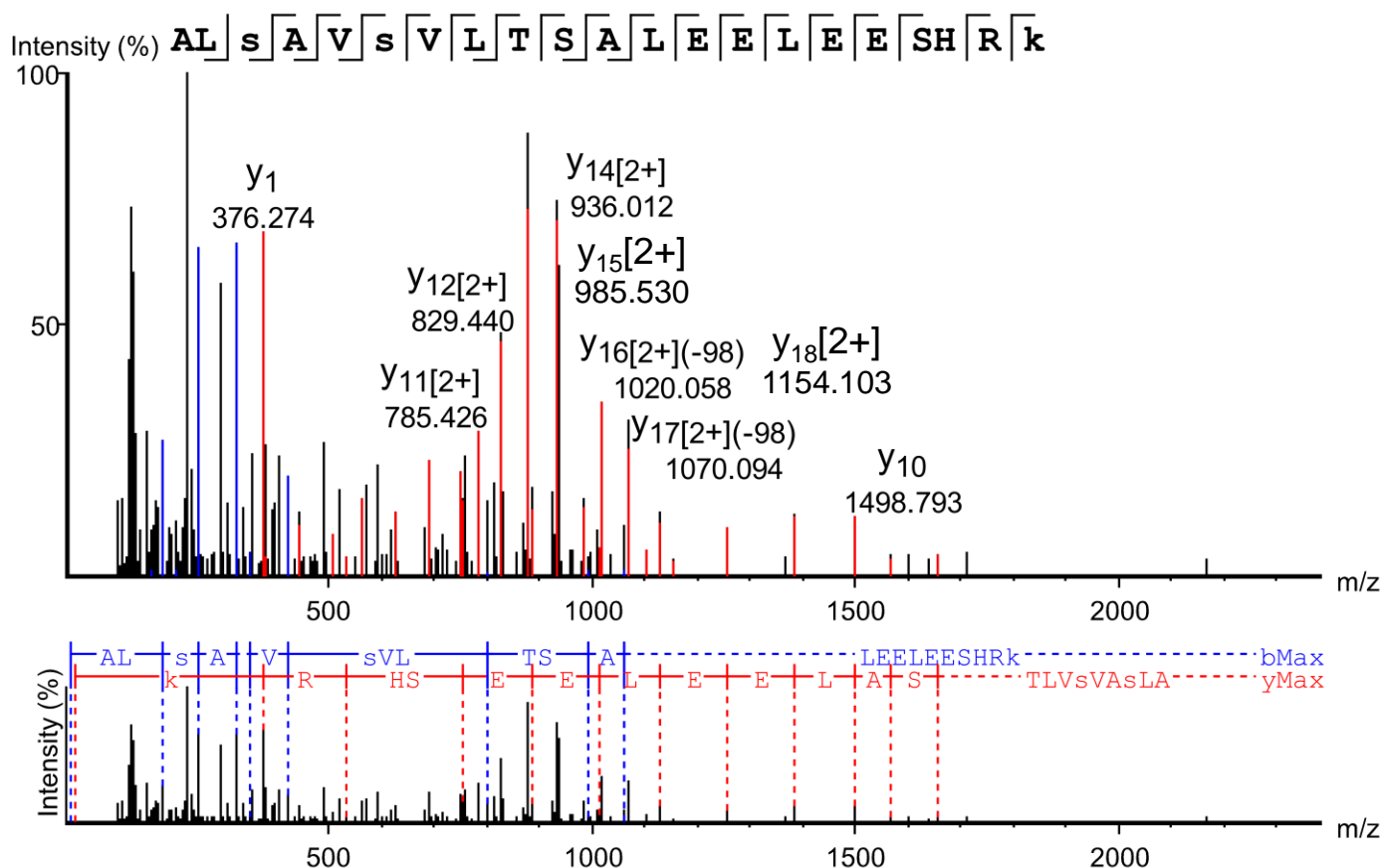


Table 2 - Figure Supplement 1.

Scan 99097, m/z=844.0719, z=3, -10lgP=59.30, ppm=-1.1 (pS664 + pT670)

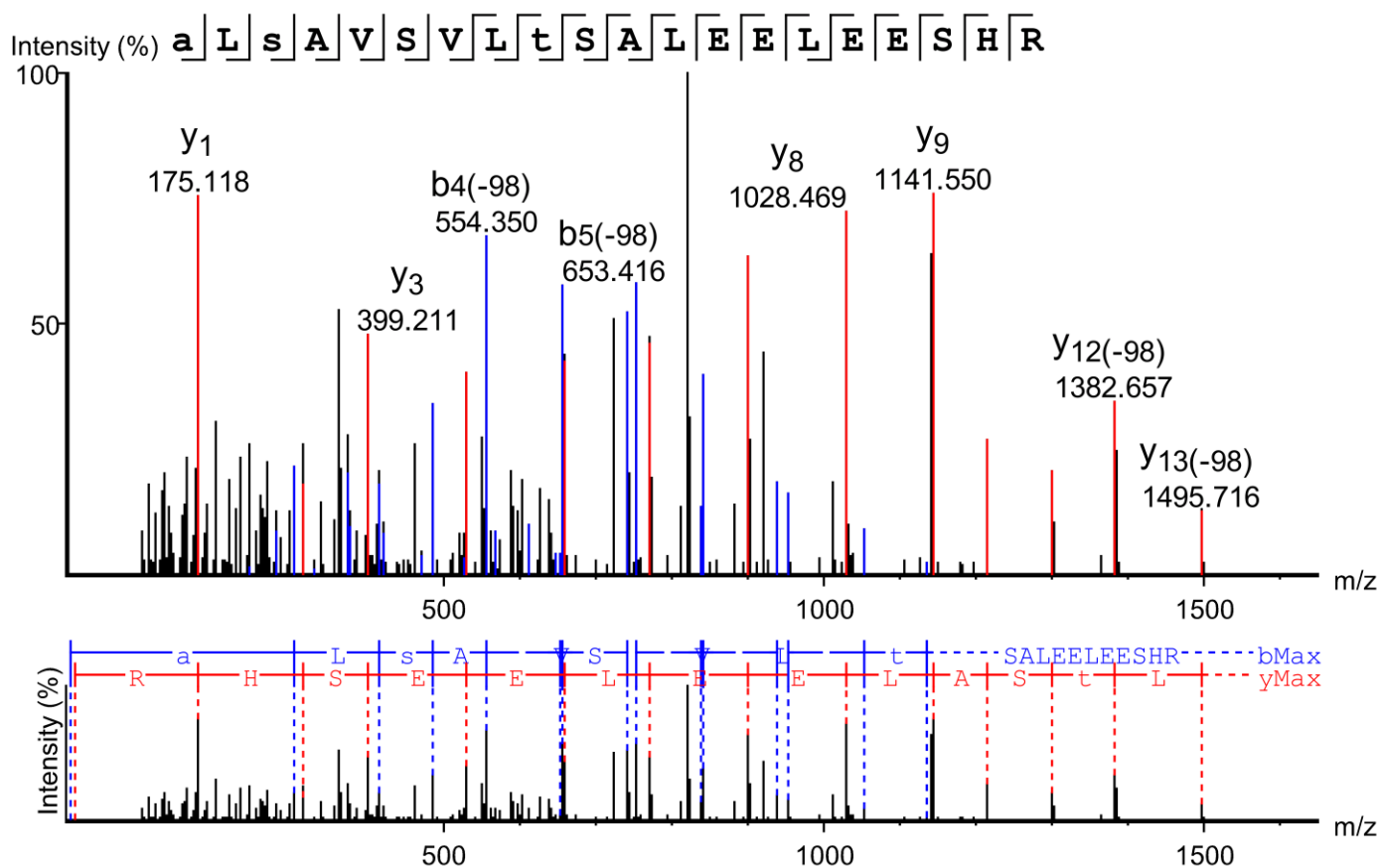


Table 2 - Figure Supplement 1.

Scan 101033, m/z=844.0723, z=3, -10lgP=58.32, ppm=-0.6 (pS664 + pS671)

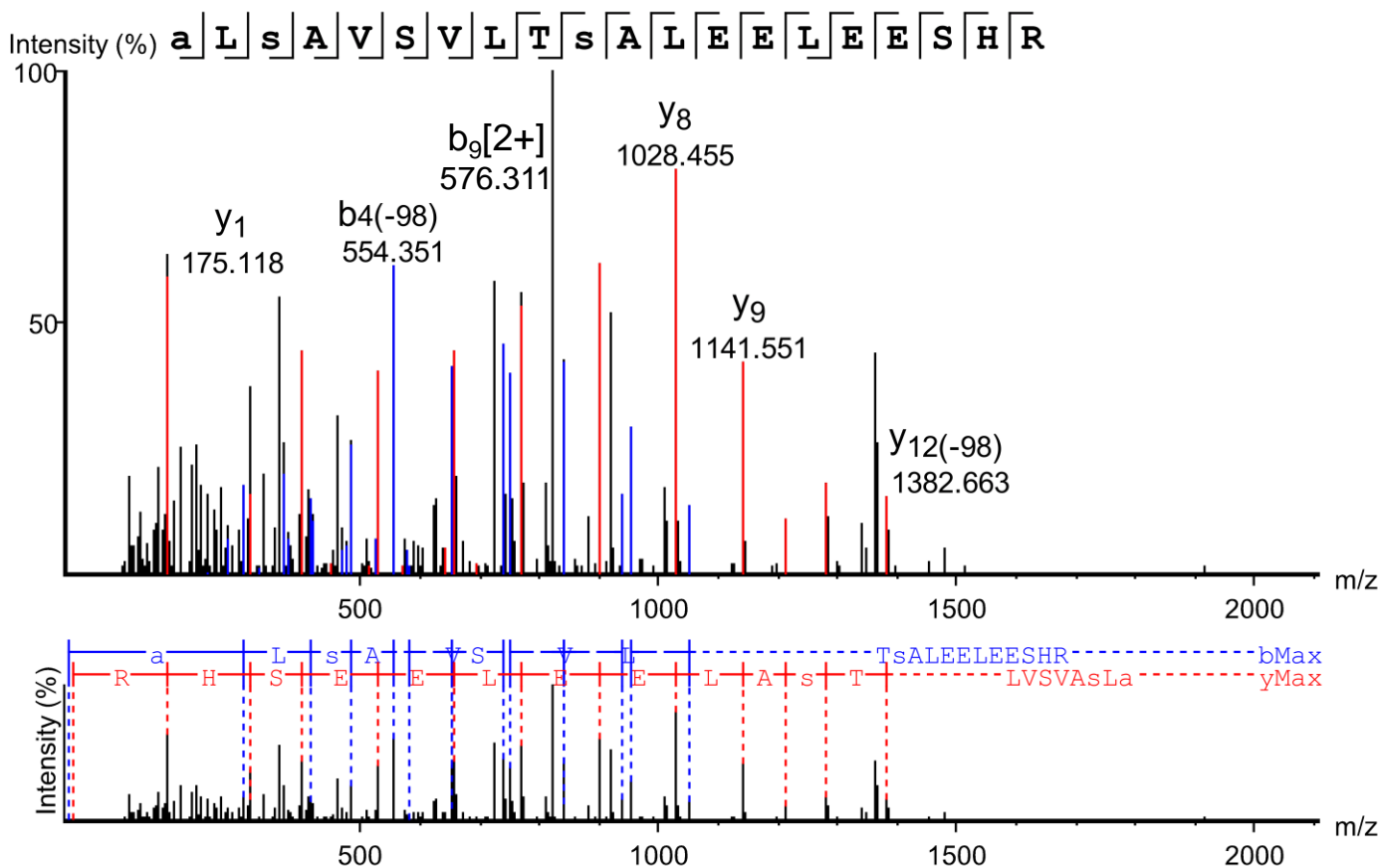


Table 2 - Figure Supplement 1.

Scan 93884, m/z=722.6213, z=4, -10lgP=54.08, ppm=0.5 (pS667 + pT670)

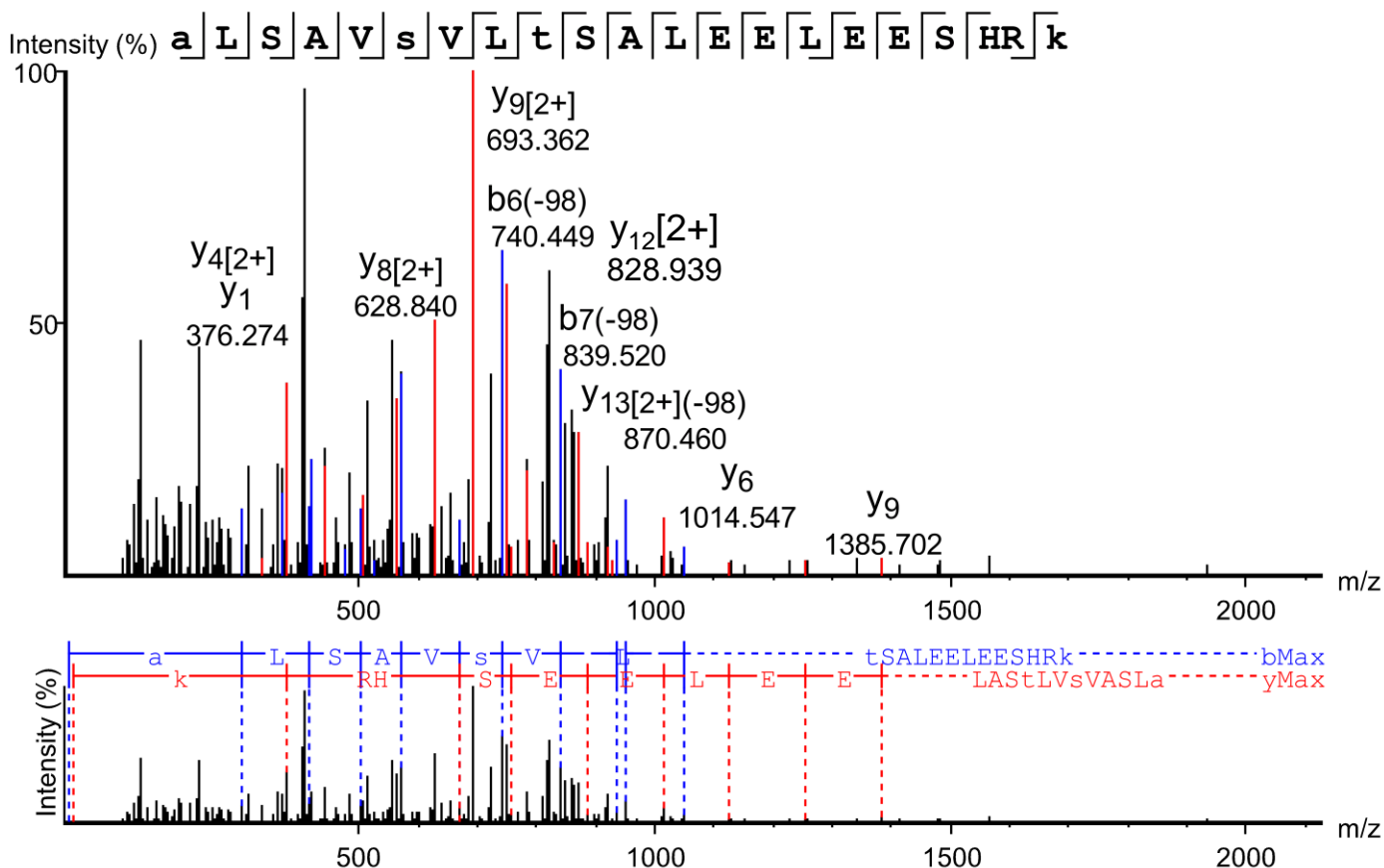


Table 2 - Figure Supplement 1.

Scan 101560, m/z=844.0726, z=3, -10lgP=60.51, ppm=-0.3 (pS667 + pS671)

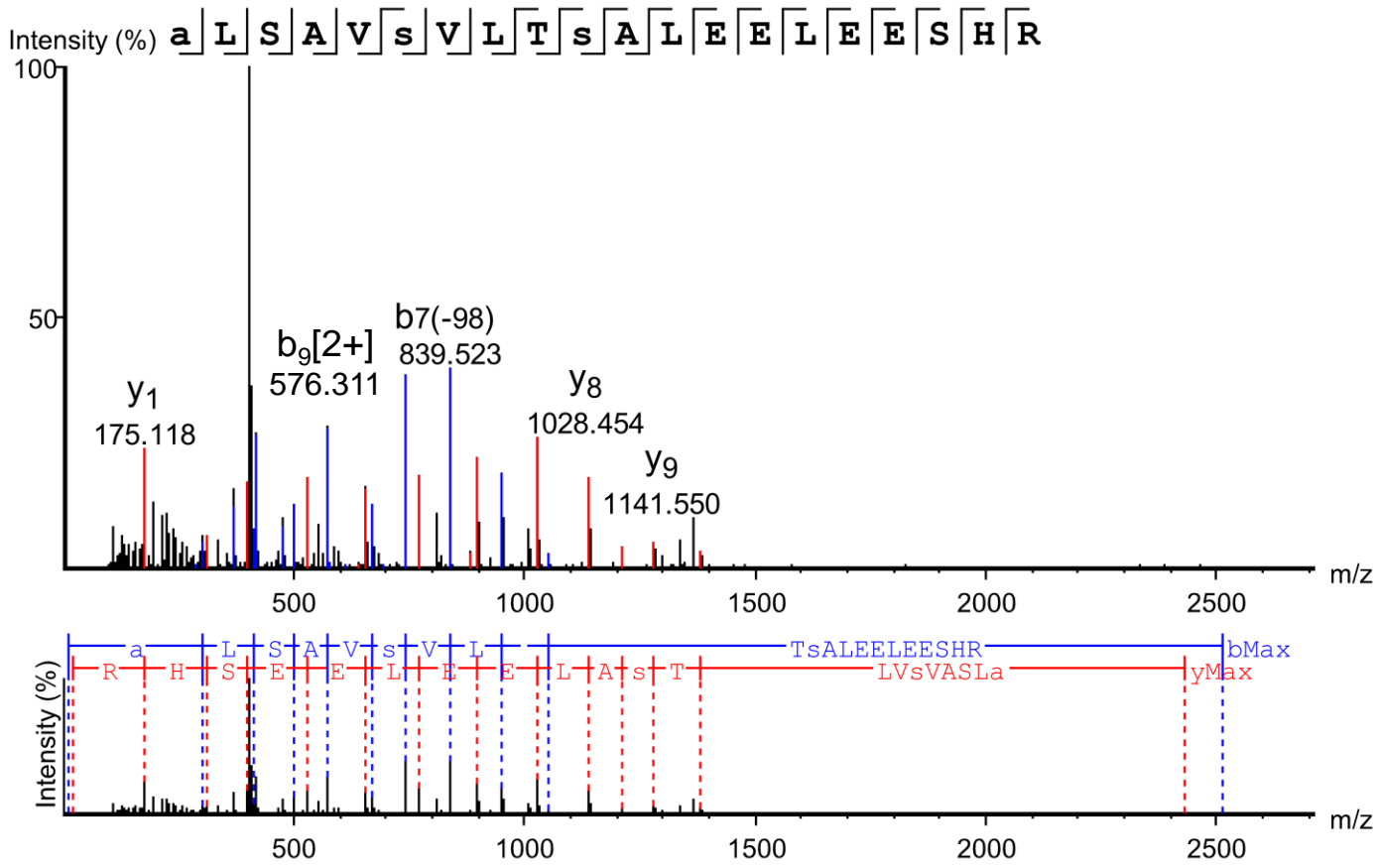


Table 2 - Figure Supplement 1.

Scan 41764, m/z=824.1139, z=3, -10lgP=48.76, ppm=-5.4 (pT999)

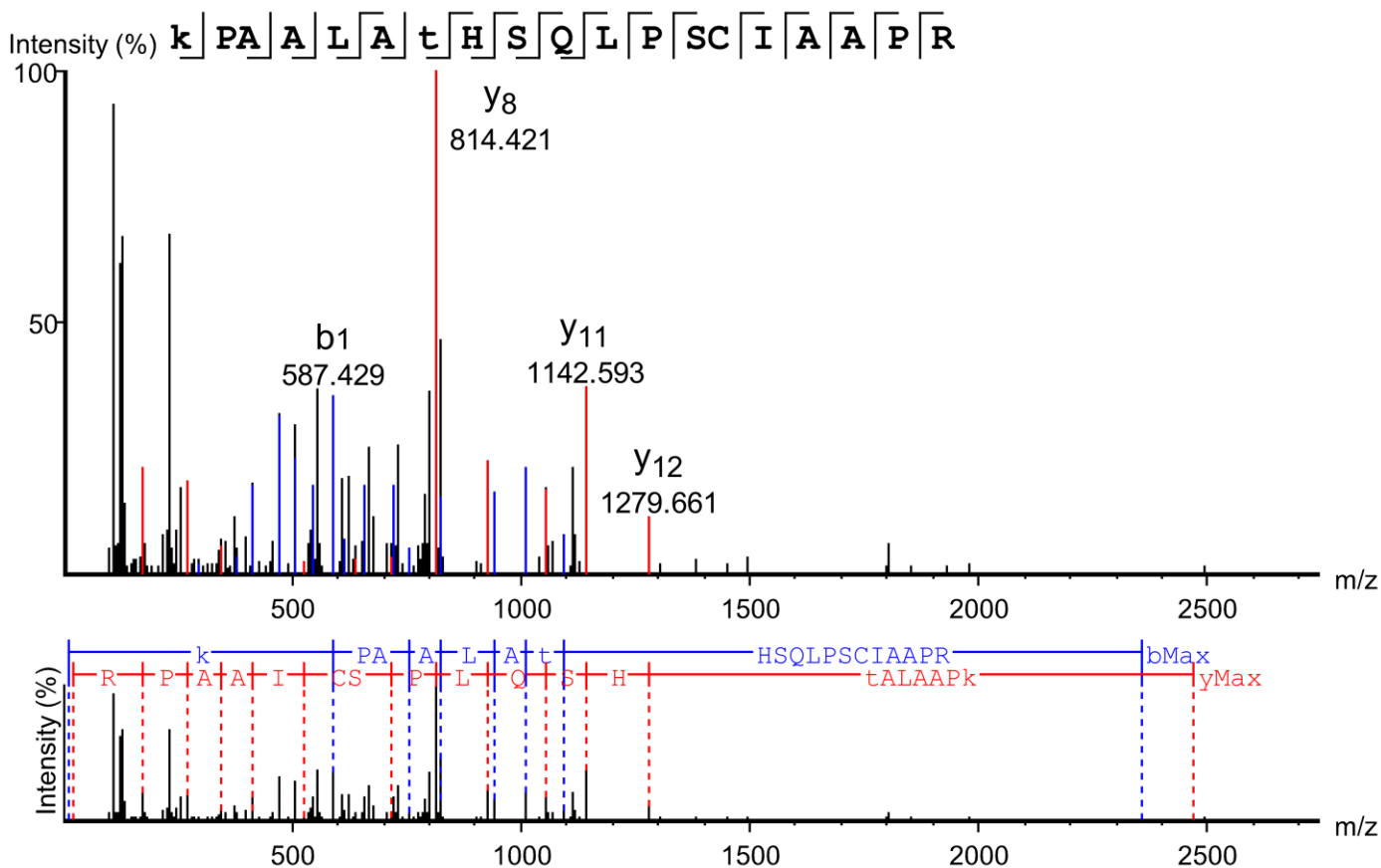


Table 2 - Figure Supplement 1.

Scan 16929, m/z=503.5912, z=3, -10lgP=32.62, ppm=6.4 (pS1001)

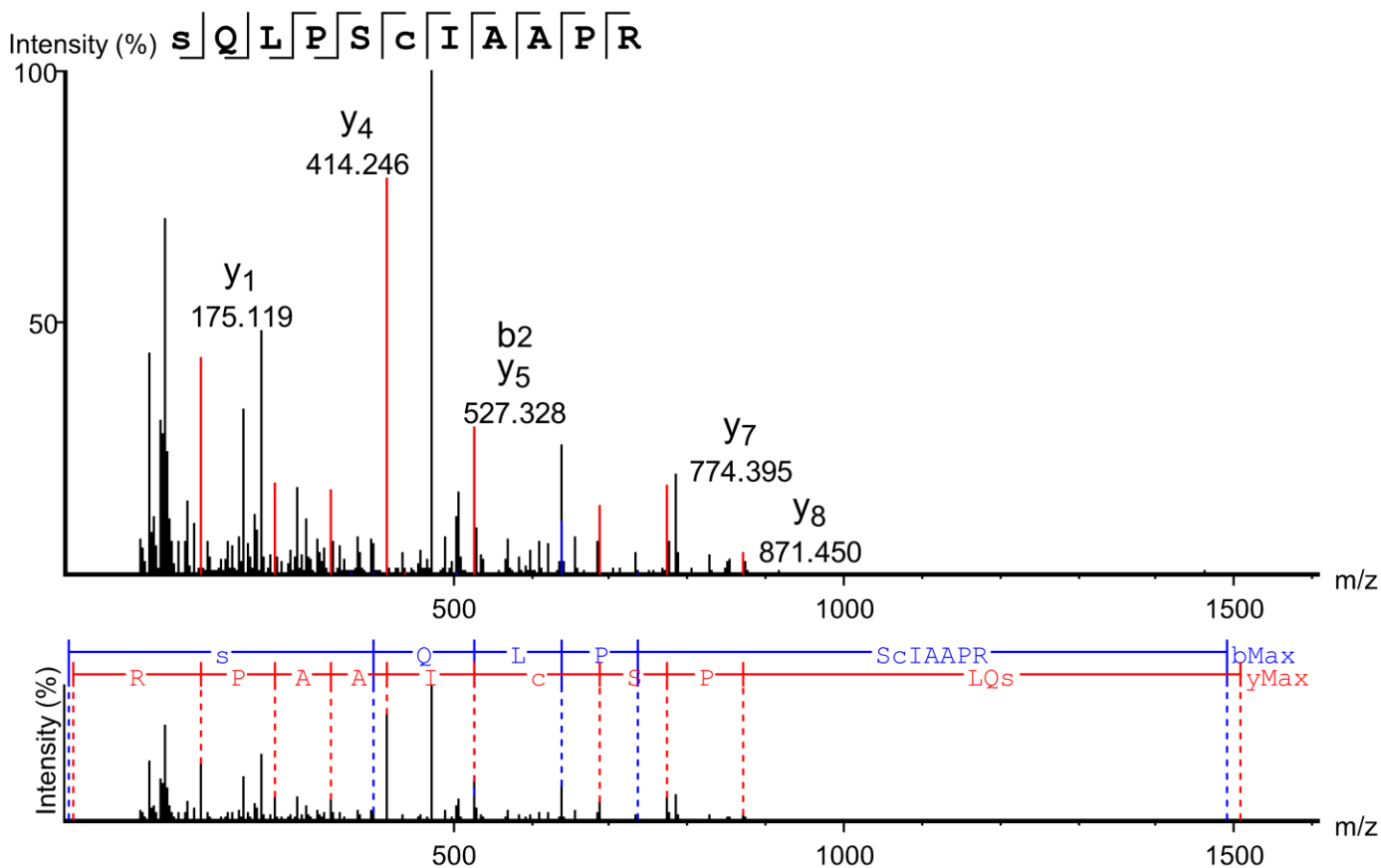


Table 2 - Figure Supplement 1.

Scan 39364, m/z=702.3888, z=6, -10lgP=71.41, ppm=-0.2 (pS1005)

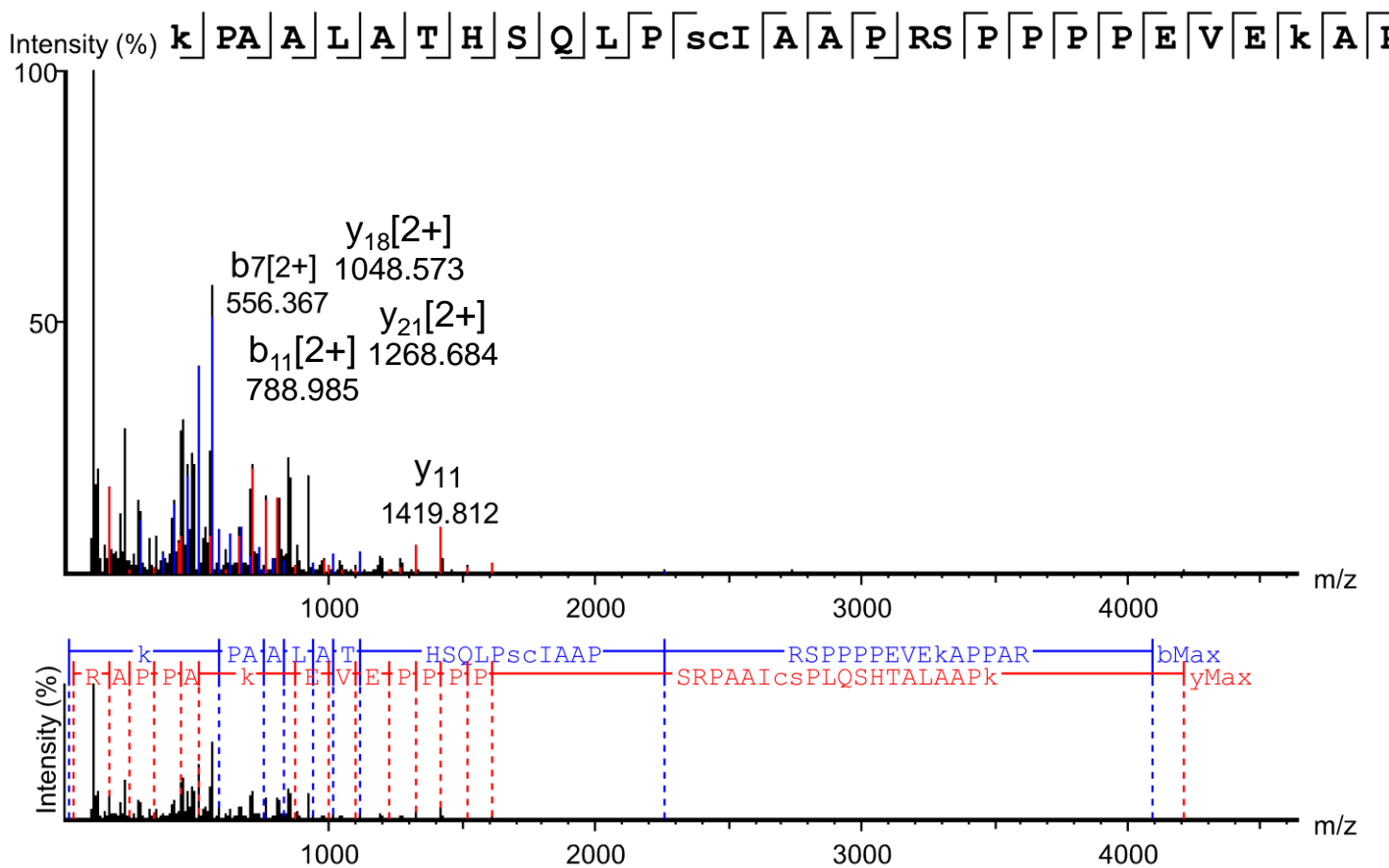


Table 2 - Figure Supplement 1.

Scan 33829, m/z=759.4054, z=2, -10lgP=42.26, ppm=1.3 (pS1012)

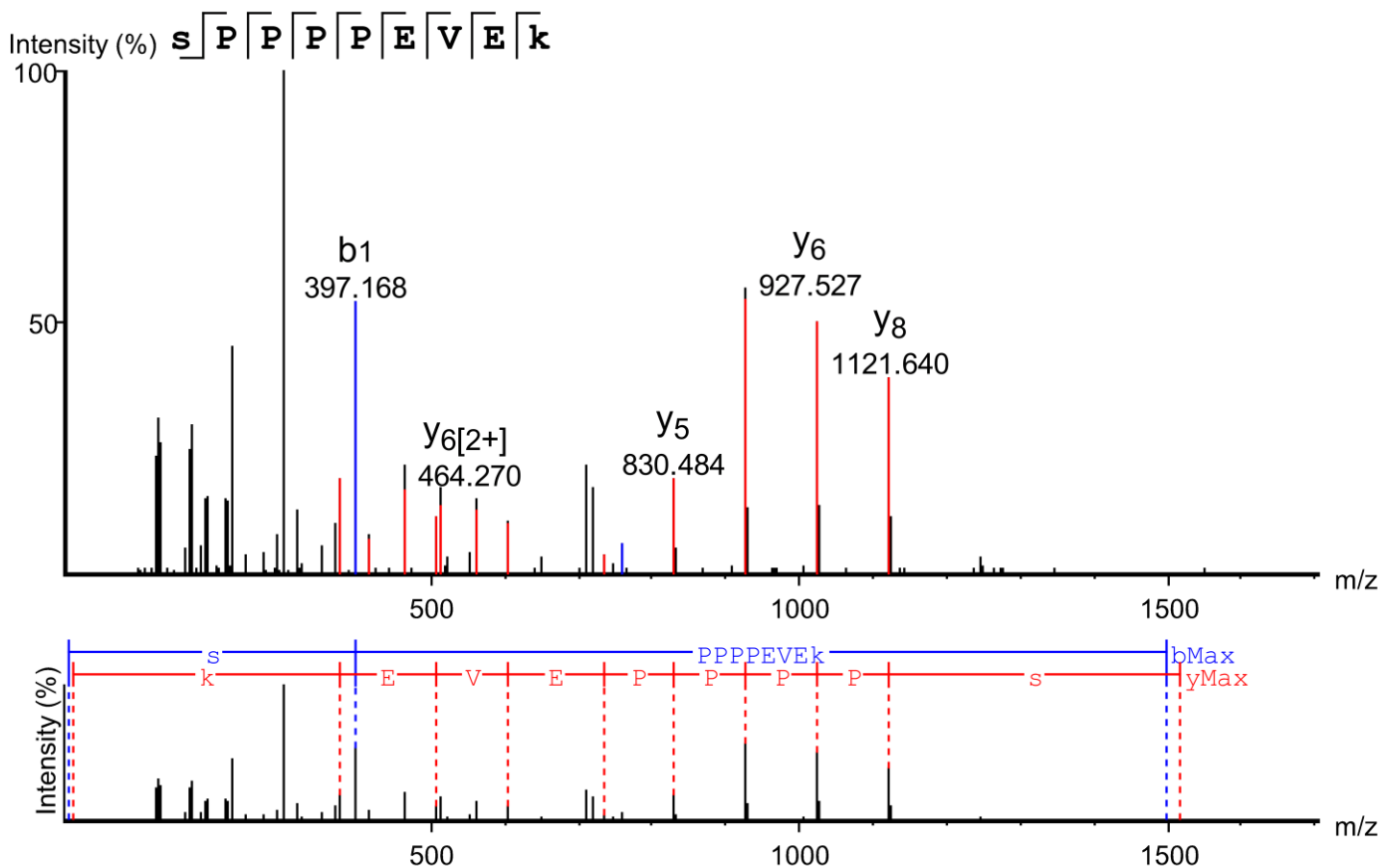


Table 2 - Figure Supplement 1.

Scan 64017, m/z=1230.5586, z=5, -10lgP=57.25, ppm=0.8 (pS1056 and/or T1058)

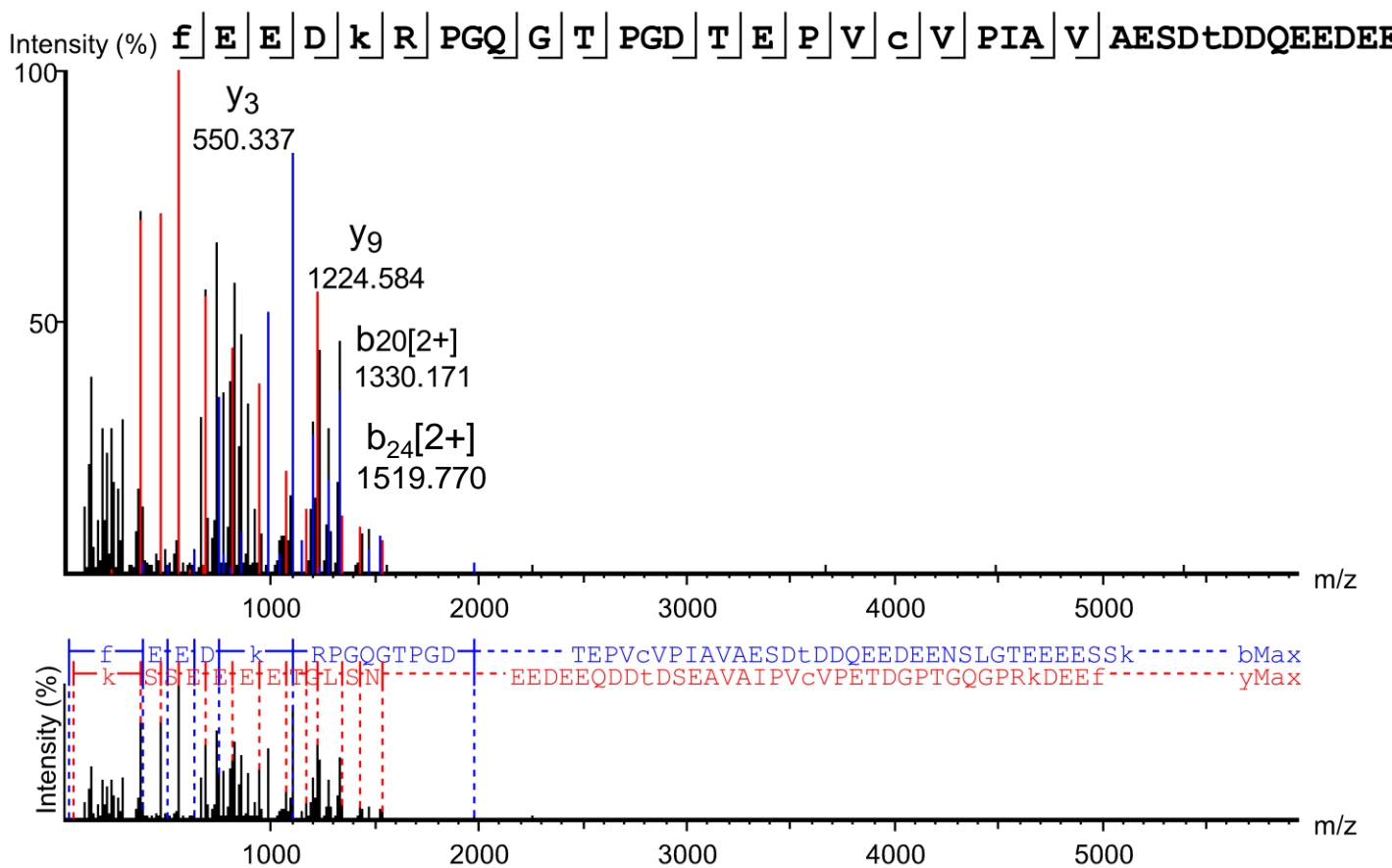


Table 2 - Figure Supplement 1.

Scan 53783, m/z=1070.1316, z=3, -10lgP=64.34, ppm=-3.2 (pT1105)

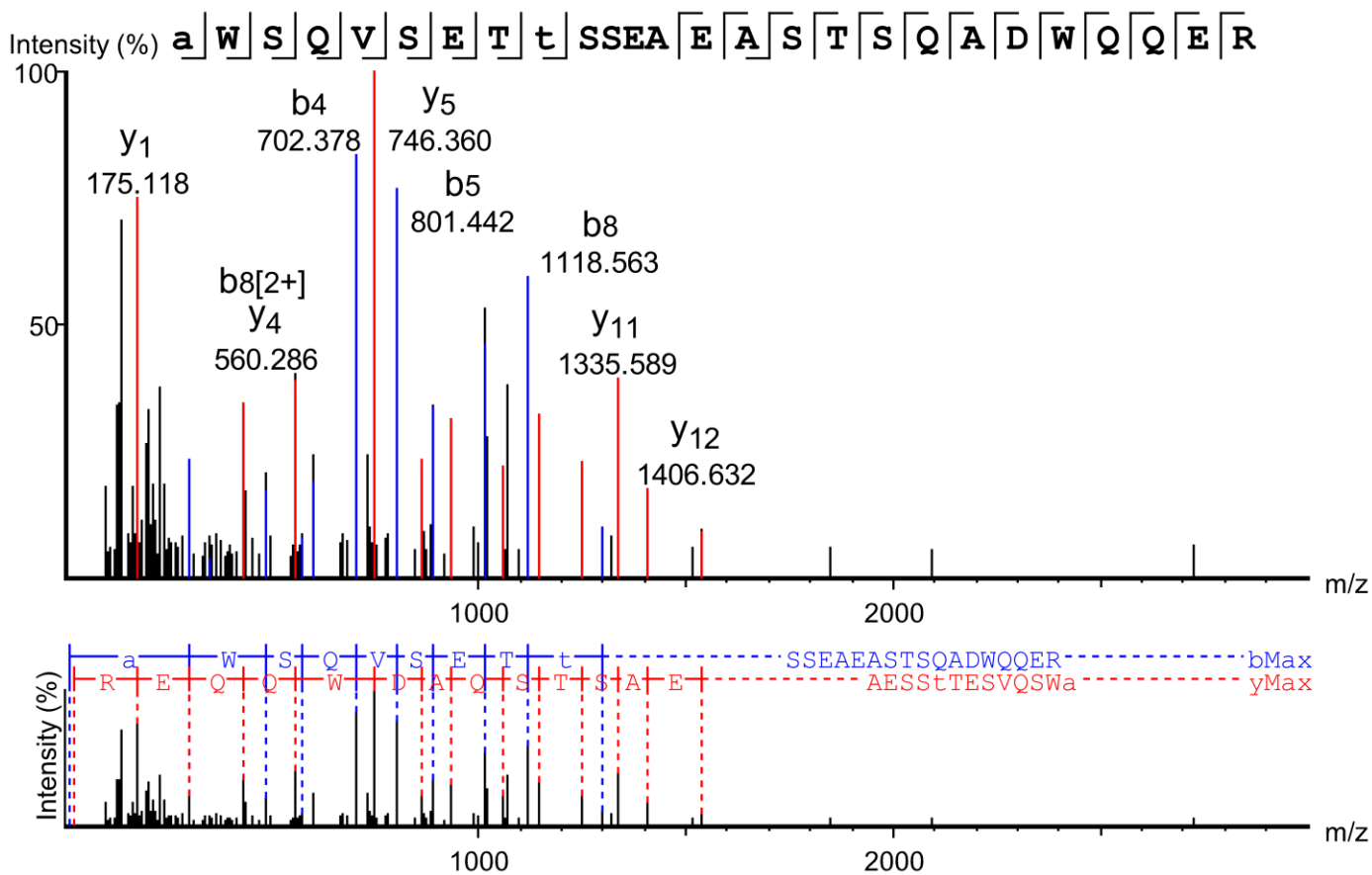


Table 2 - Figure Supplement 1.

Scan 54409, m/z=1070.1345, z=3, -10lgP=69.89, ppm=-0.5 (pS1107)

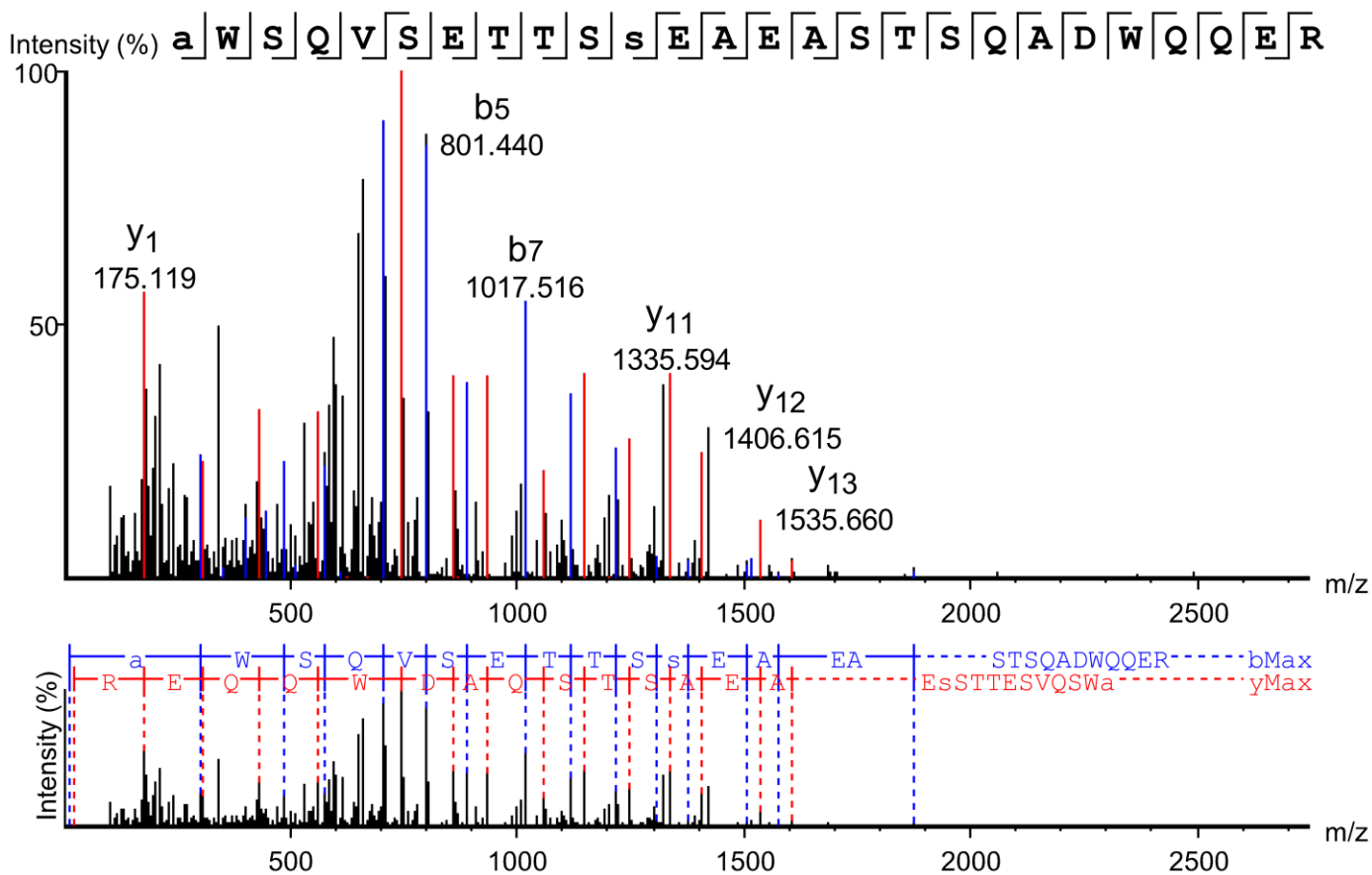


Table 2 - Figure Supplement 1.

Scan 92771, m/z=1312.5819, z=4, -10lgP=44.70, ppm=3.2 (pS1138)

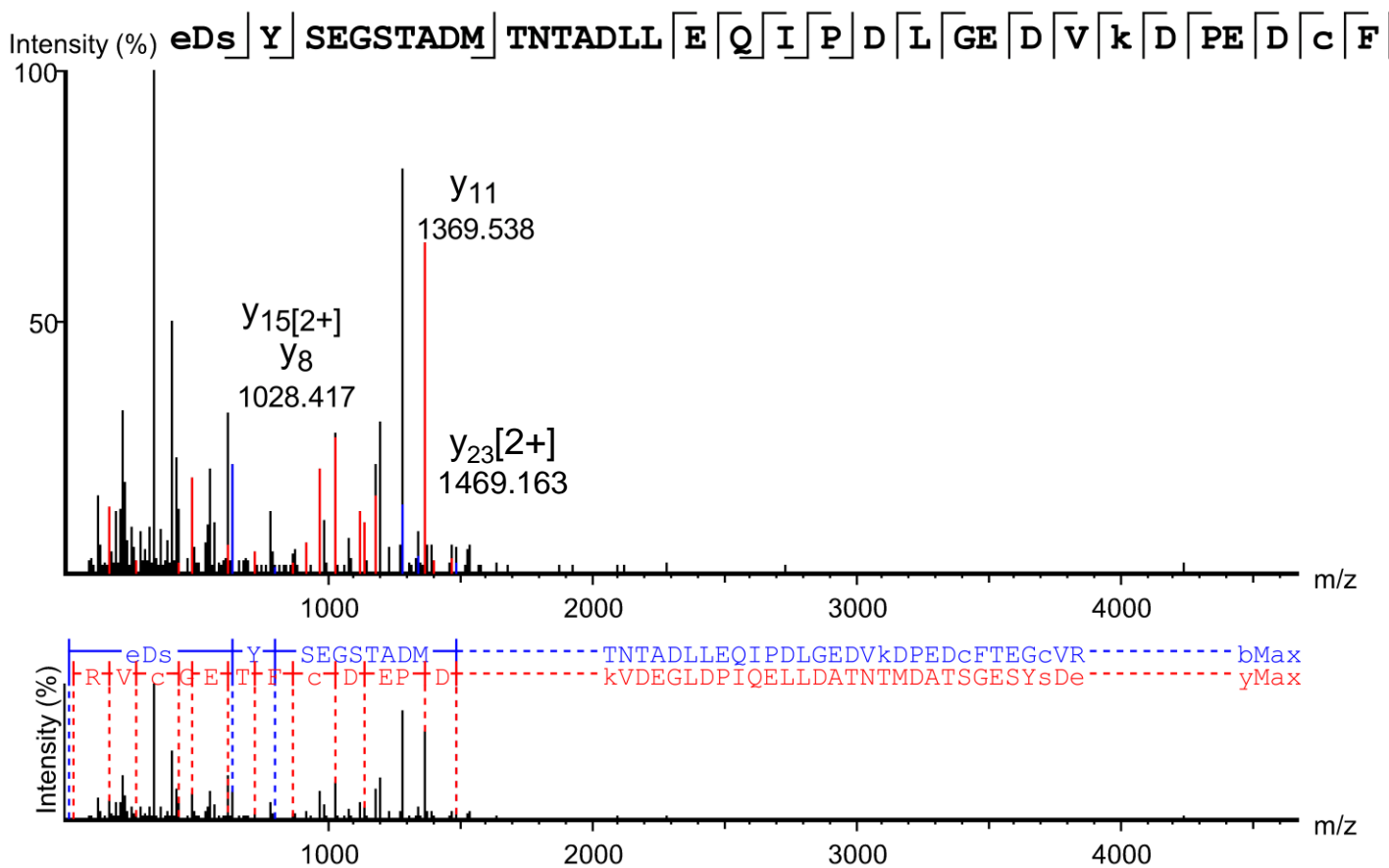


Table 2 - Figure Supplement 1.

Scan 101916, m/z=903.4511, z=3, -10lgP=54.76, ppm=-1.2 (pT1809)

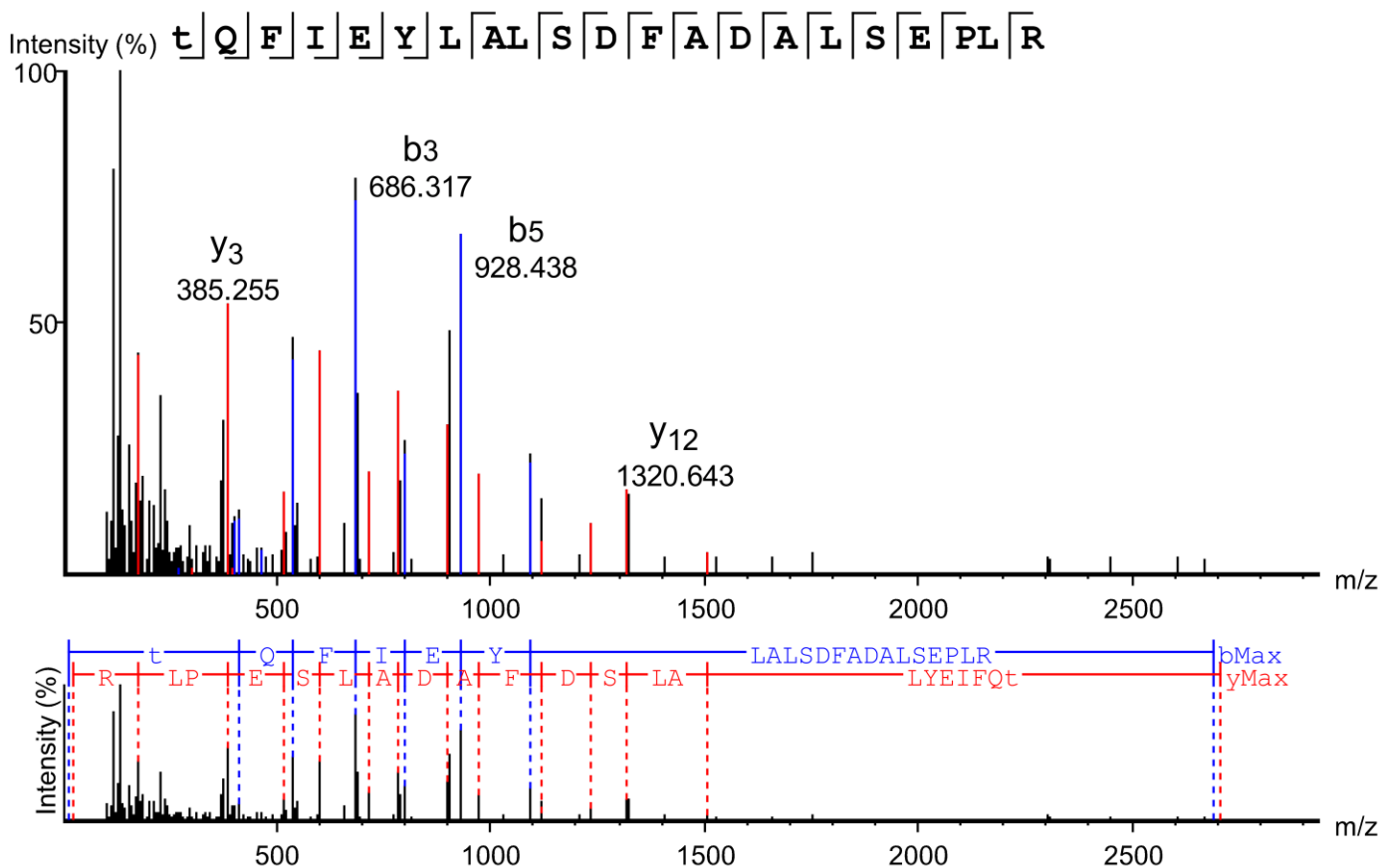


Table 2 - Figure Supplement 1.

Scan 24603, m/z=978.4300, z=2, -10lgP=60.07, ppm=-0.9 (pS1937)

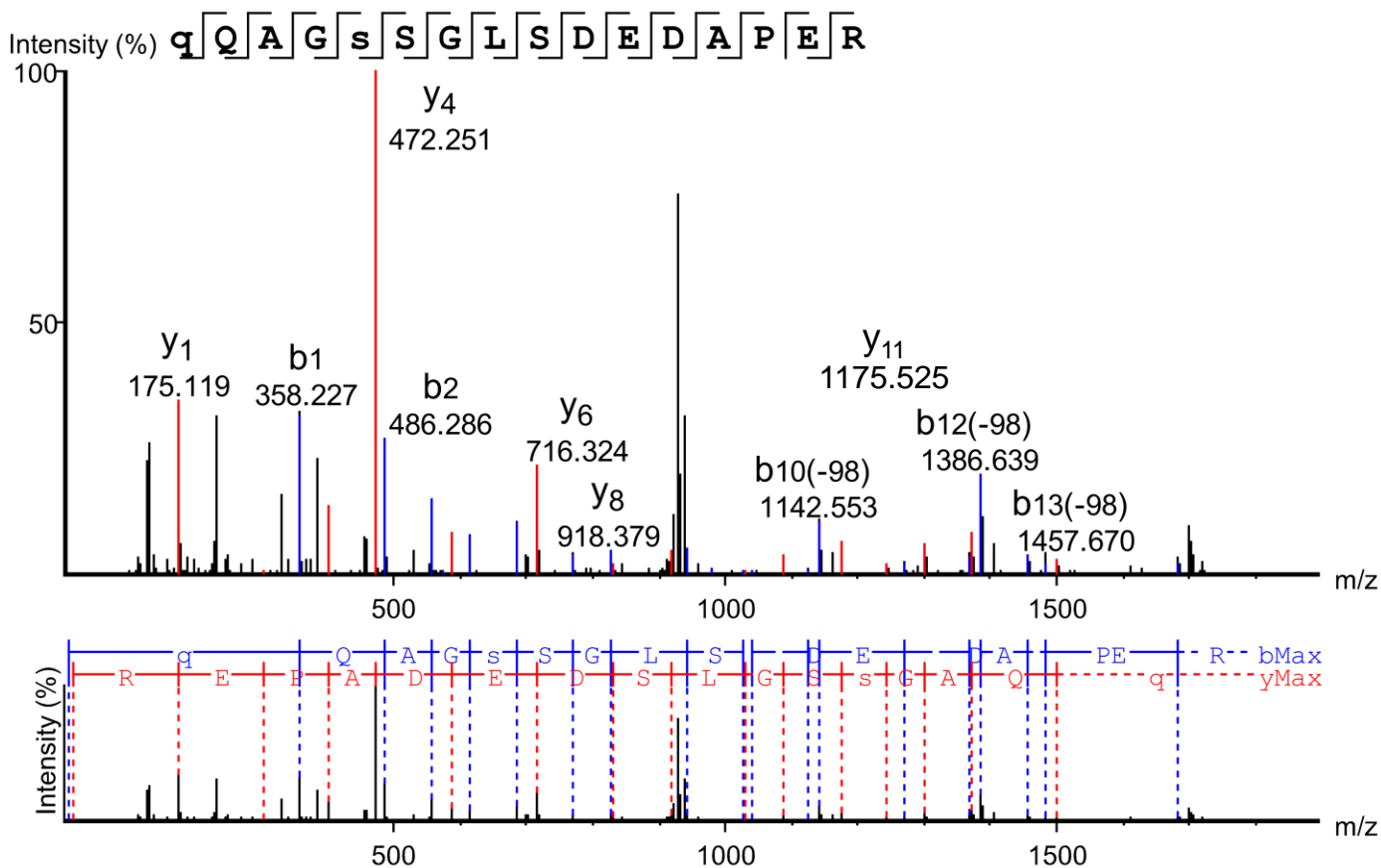


Table 2 - Figure Supplement 1.

Scan 67128, m/z=885.7517, z=3, -10lgP=50.34, ppm=0.7 (pS1964)

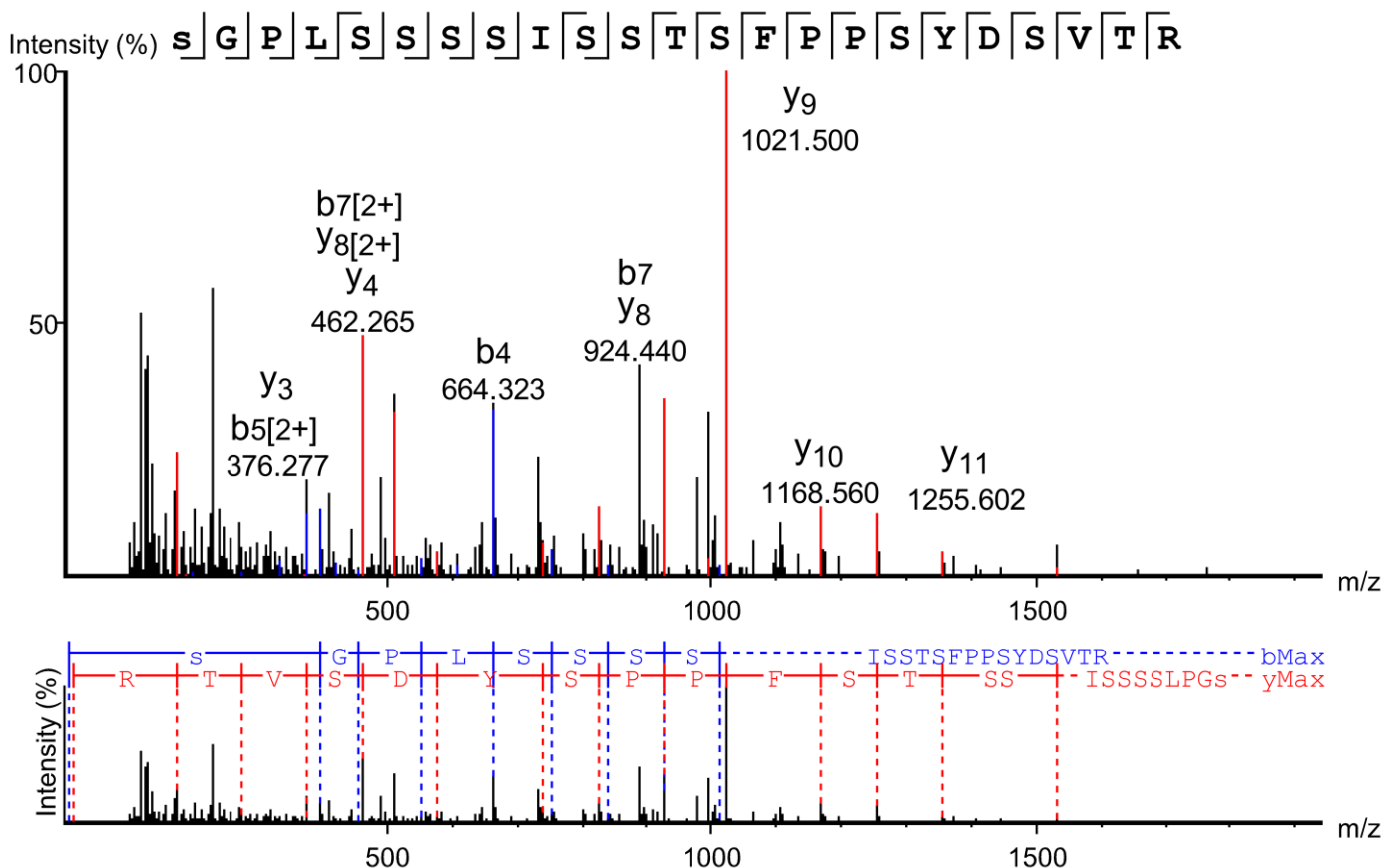


Table 2 - Figure Supplement 1.

Scan 67492, m/z=885.7529, z=3, -10lgP=56.87, ppm=2.1 (pS1969)

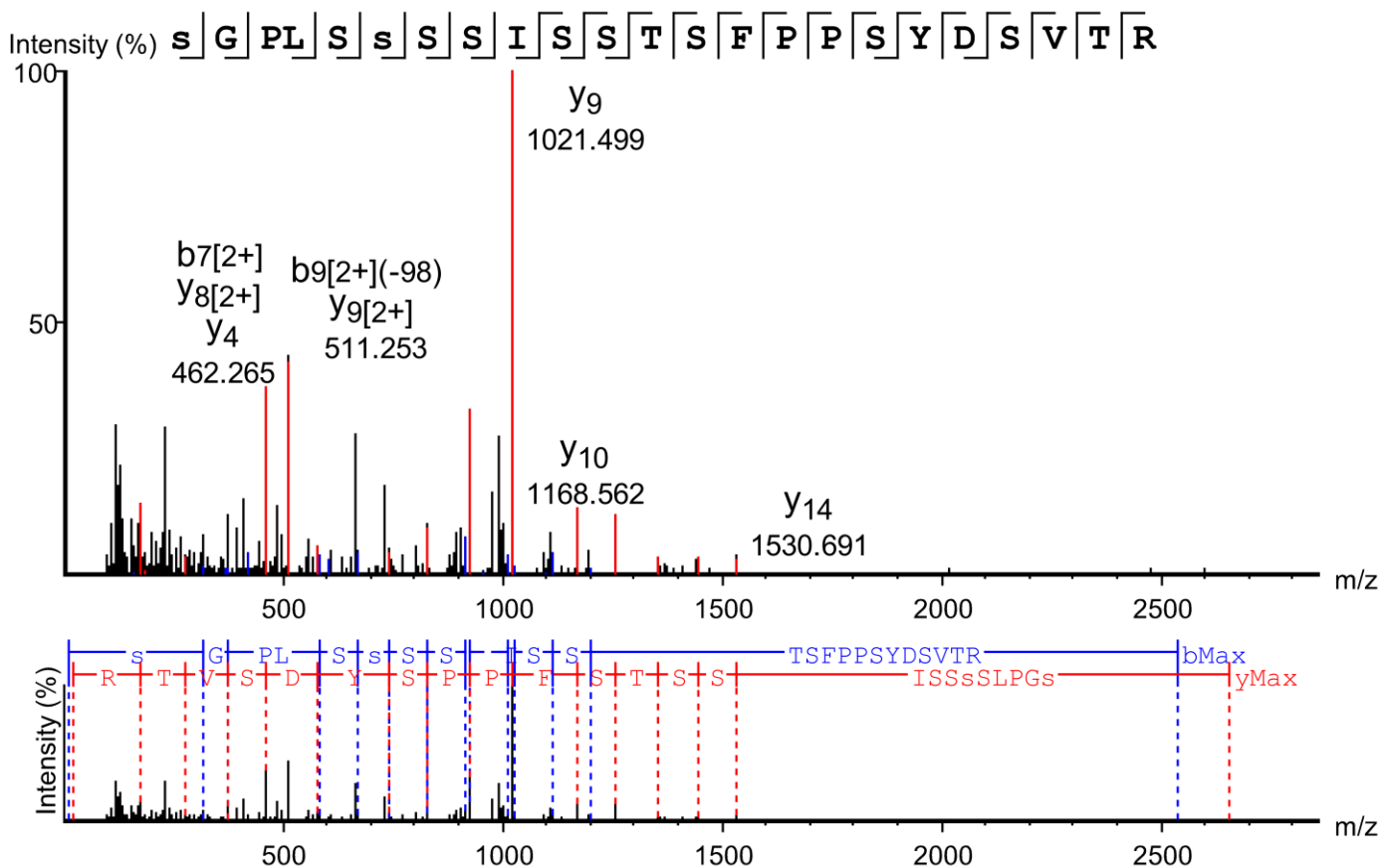


Table 2 - Figure Supplement 1.

Scan 49853, m/z=937.7873, z=3, -10lgP=48.49, ppm=2.7 (pS1971)

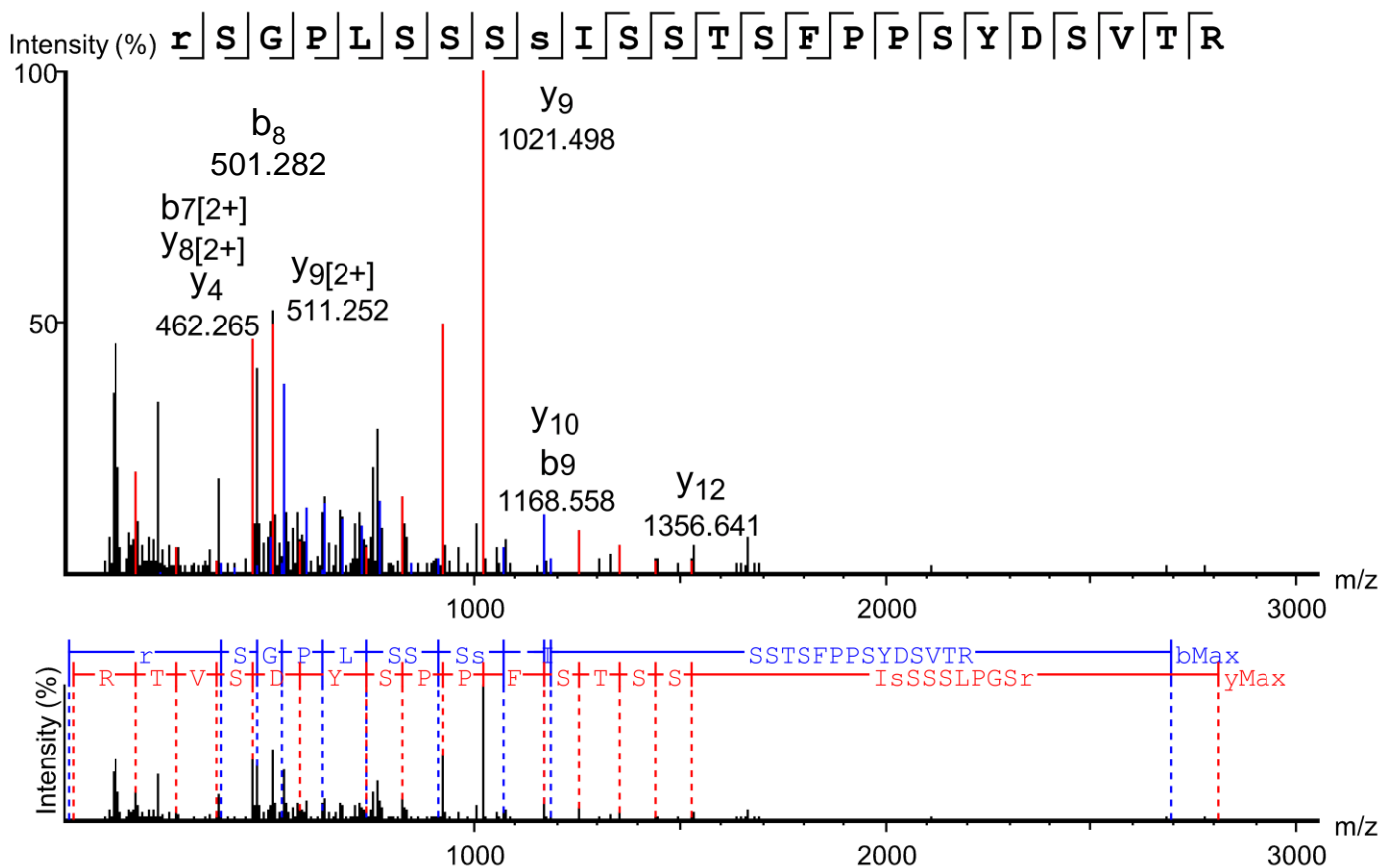


Table 2 - Figure Supplement 1.

Scan 64573, m/z=885.7498, z=3, -10lgP=61.75, ppm=-1.4 (pS1973)

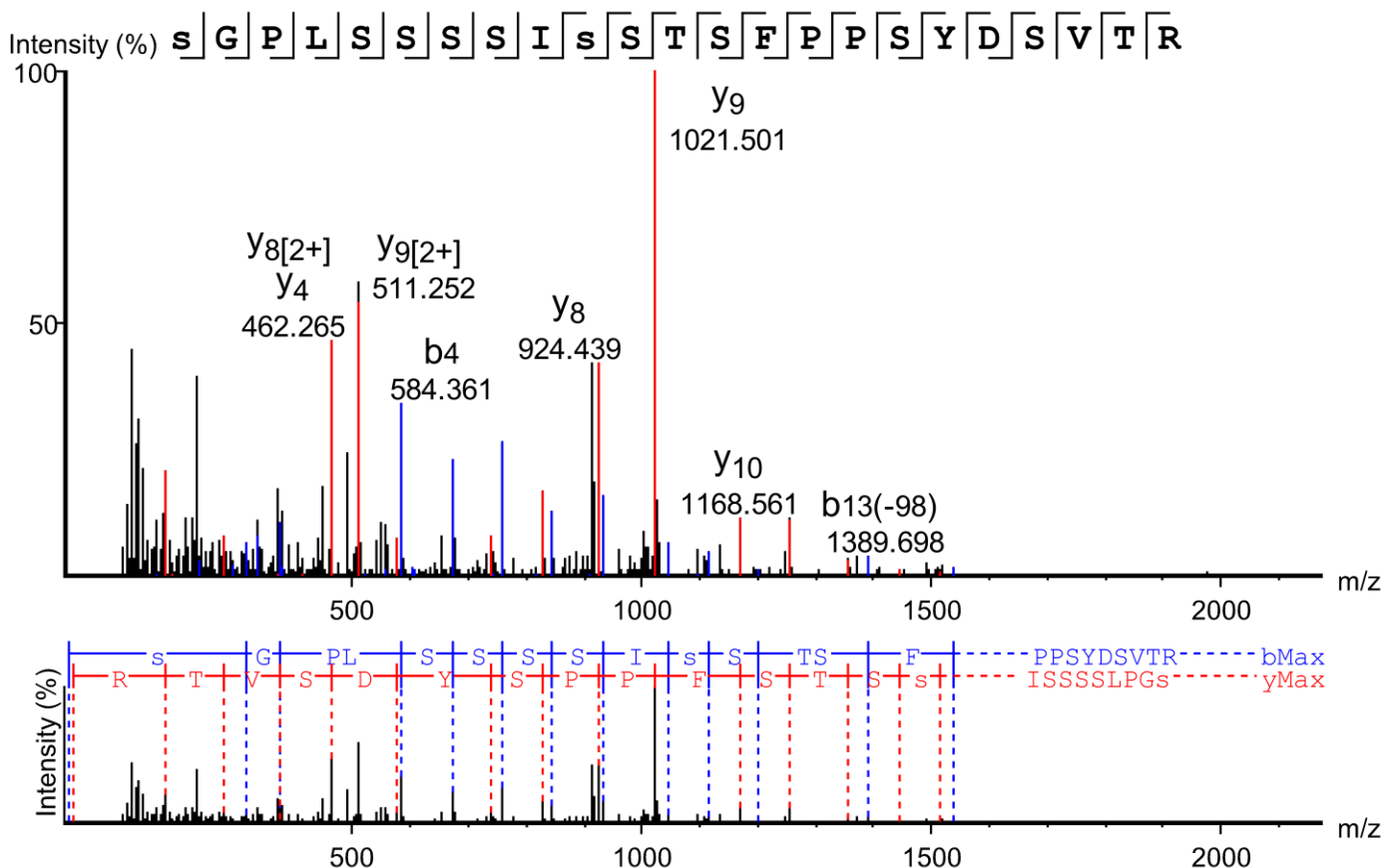


Table 2 - Figure Supplement 1.

Scan 64993, m/z=885.7498, z=3, -10lgP=61.81, ppm=-1.5 (pS1974)

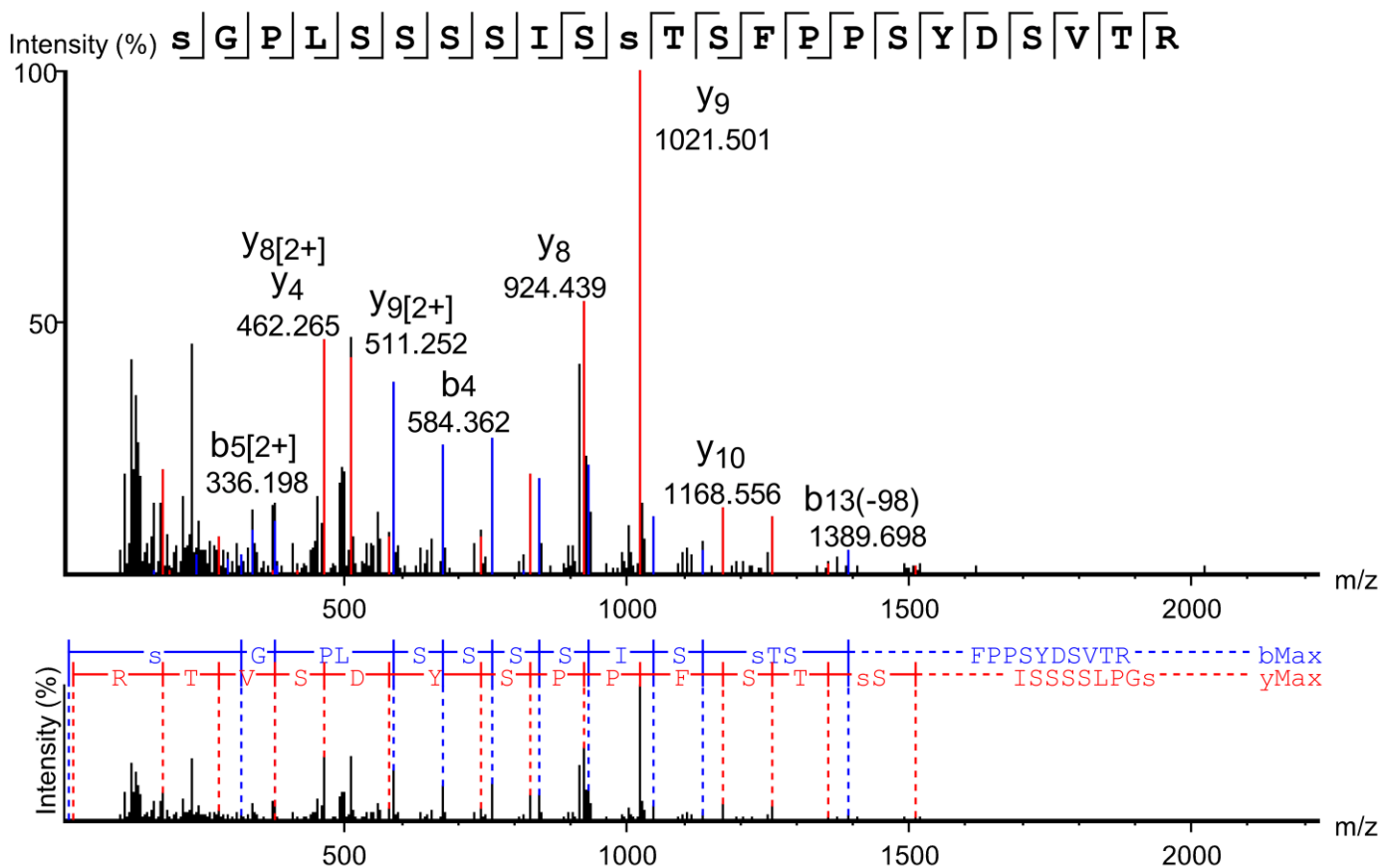


Table 2 - Figure Supplement 1.

Scan 31030, m/z=641.3244, z=2, -10lgP=37.66, ppm=1.1 (pS1989)

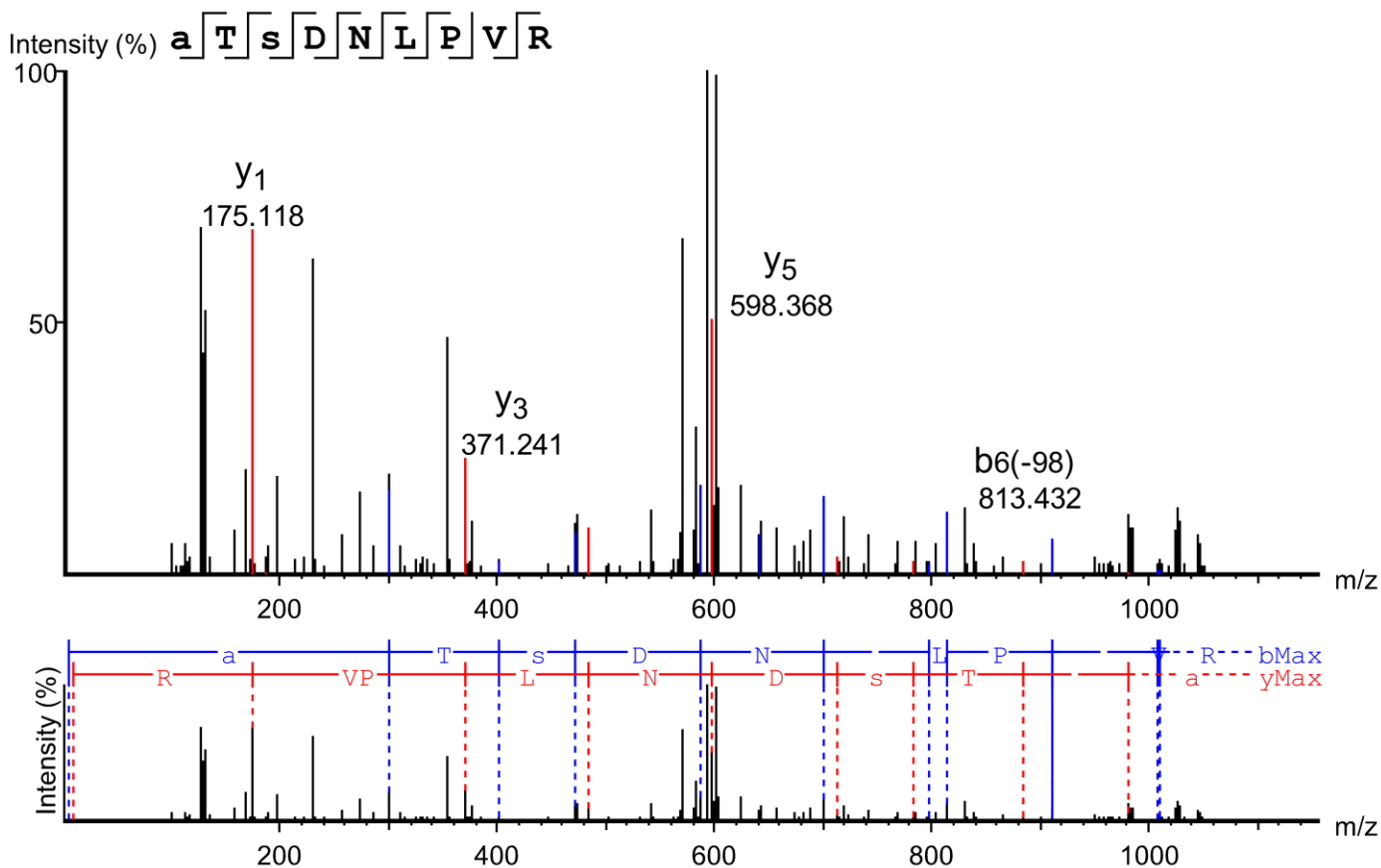


Table 2 - Figure Supplement 1.

Scan 41663, m/z=675.9753, z=3, -10lgP=38.78, ppm=-0.1 (pS2011)

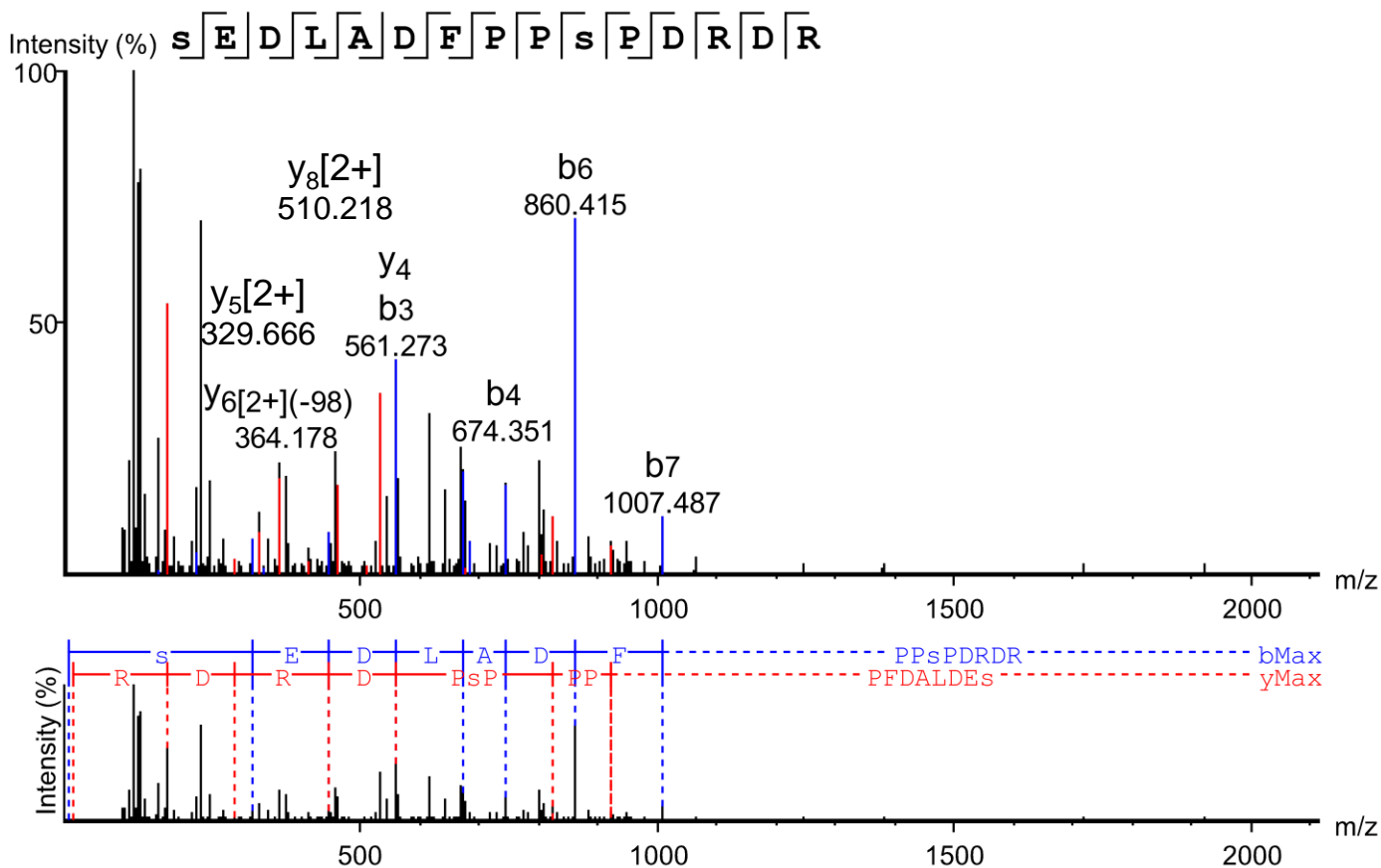


Table 2 - Figure Supplement 1.

Scan 75683, m/z=861.8894, z=4, -10lgP=48.05, ppm=3.0 (Na_v1.4; pS522 + pS525)

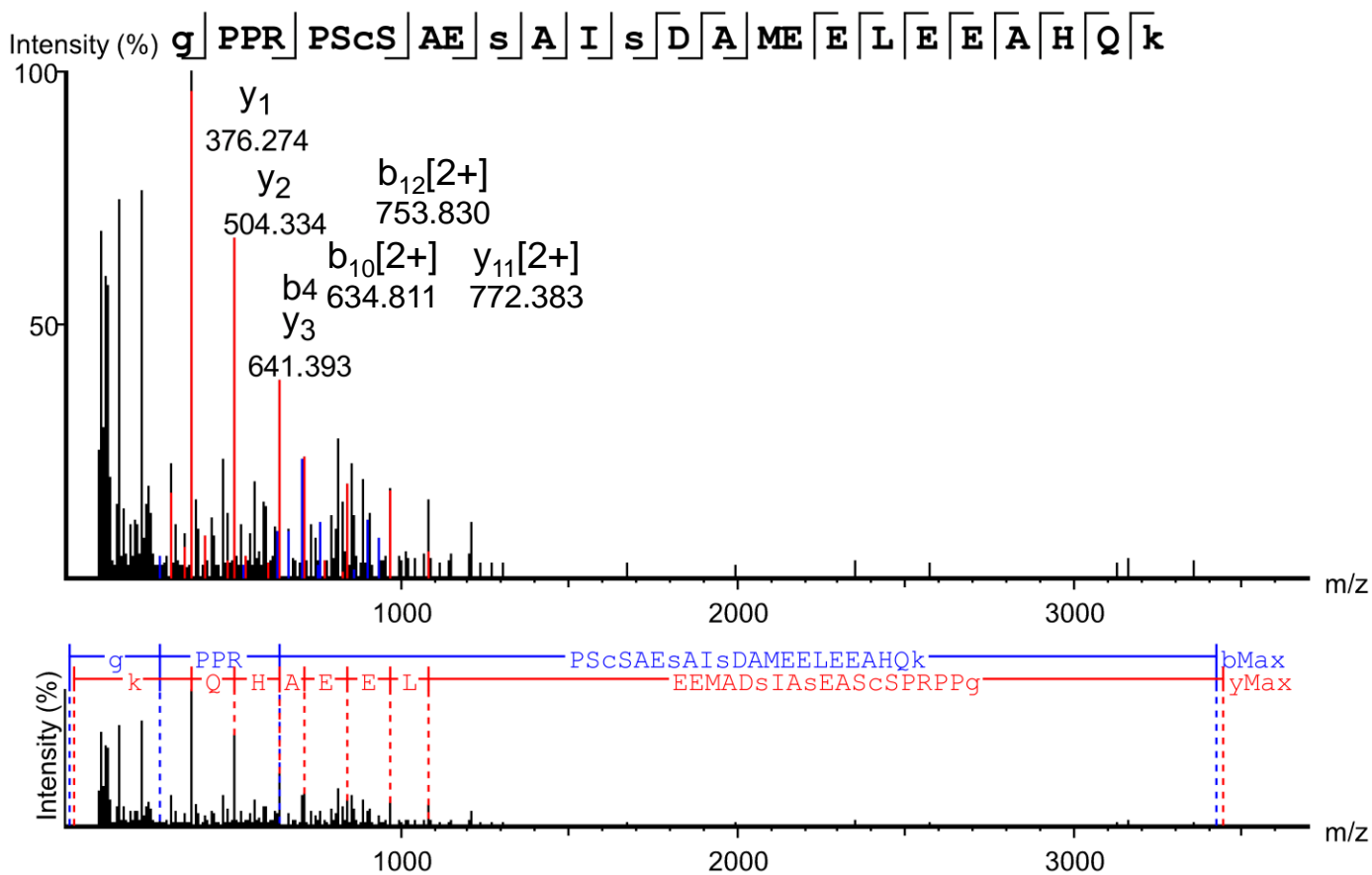


Table 2 - Figure Supplement 1.

Scan 64345, m/z=841.8929, z=4, -10lgP=60.31, ppm=-2.8 (Na_v1.4; pS525)

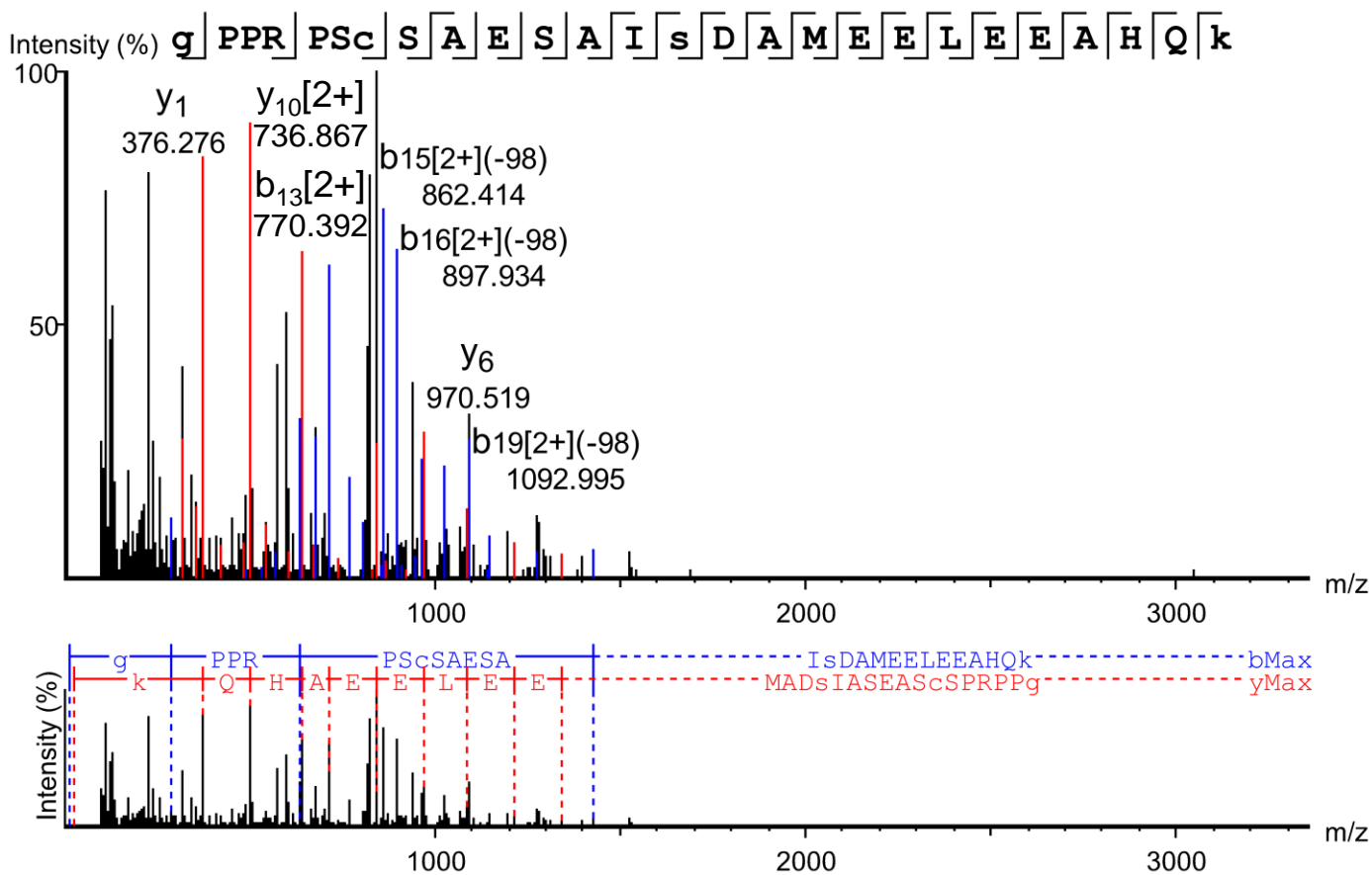


Table 2 - Figure Supplement 1.

Scan 91385, m/z=1486.9480, z=4, -10lgP=54.20, ppm=1.1 (Na_v1.4; pS900)

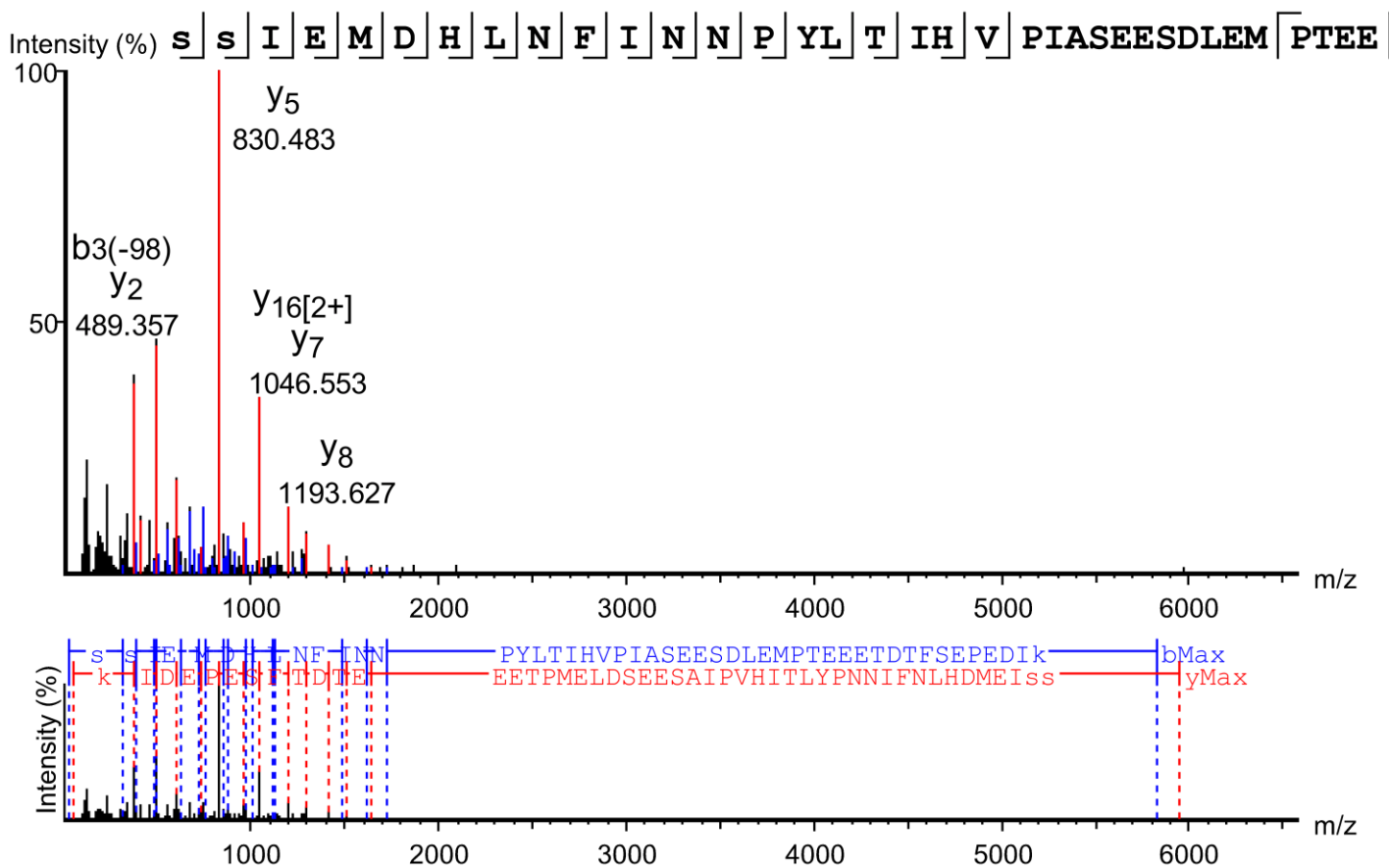


Table 2 - Figure Supplement 1.

Scan 49121, m/z=927.4735, z=6, -10lgP=52.01, ppm=1.1 (Na_v1.4; pS1819)

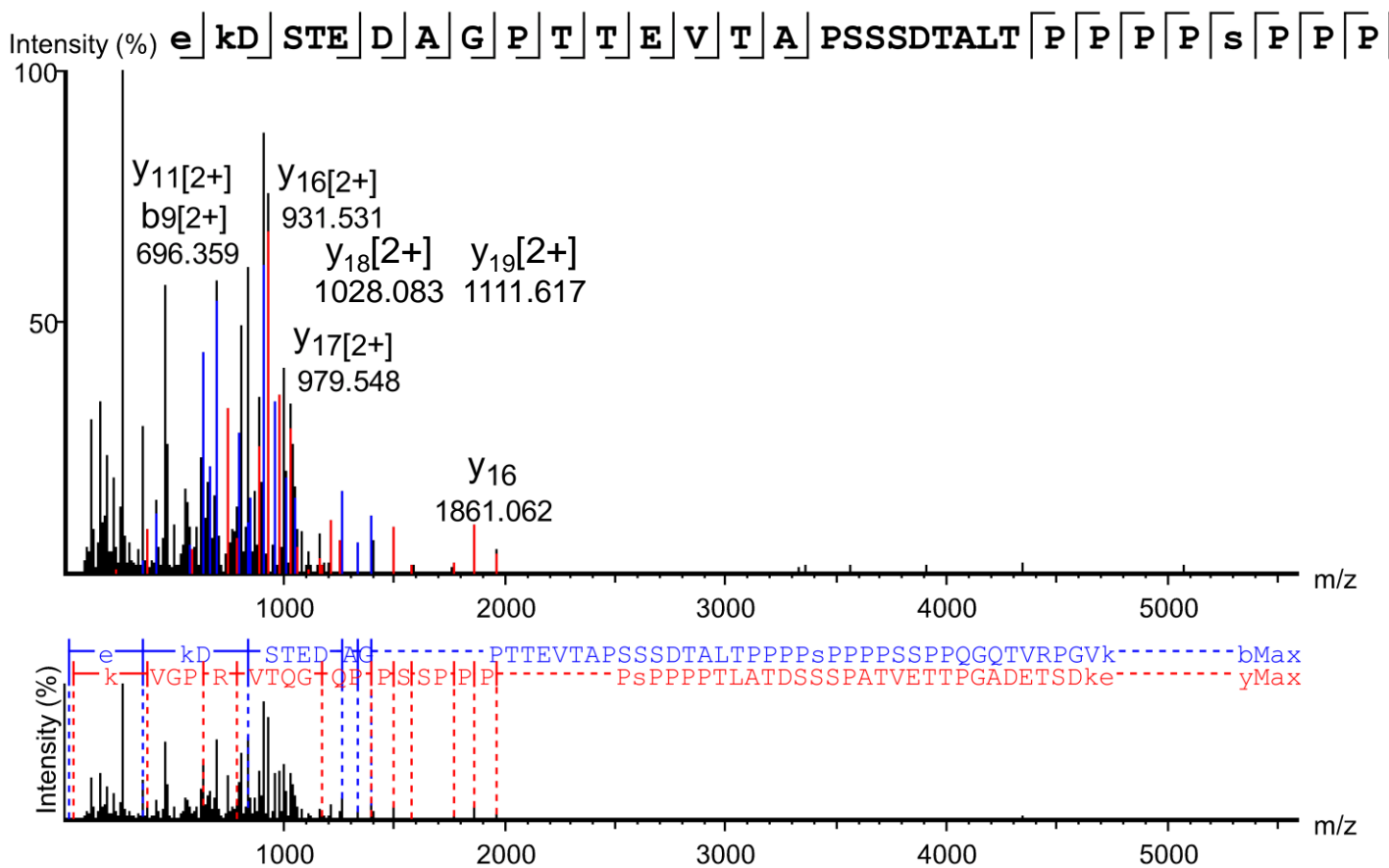


Table 2 - Figure Supplement 1.

Scan 99924, m/z=817.3834, z=3, -10lgP=63.96, ppm=-1.6 (Na_v1.3; pS658)

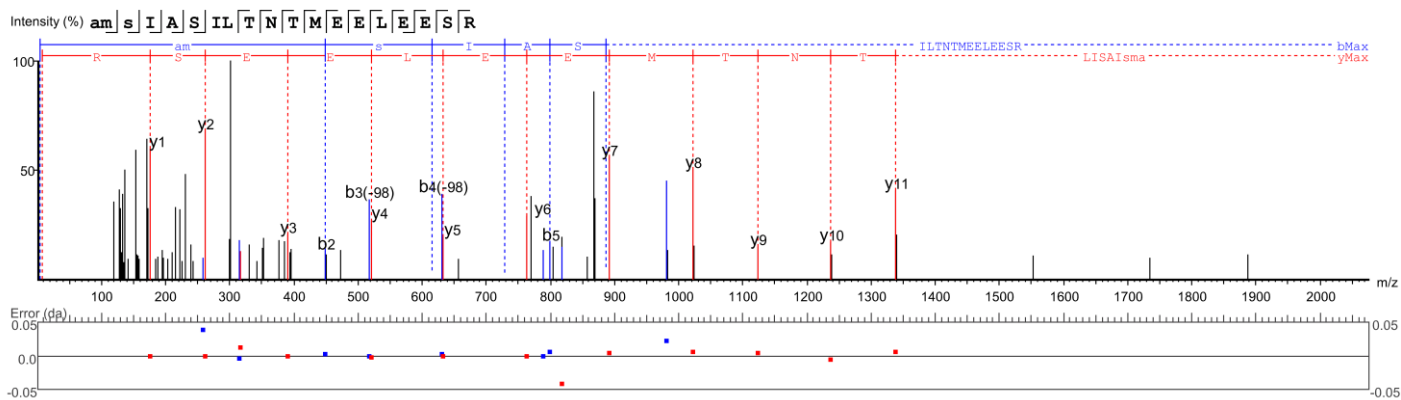


Table 2 - Figure Supplement 1.